Quantum Electrodynamics in Strong-Field Interactions: Simulation Tools towards Future Experiments

Inaugural-Dissertation

zur Erlangung des Doktorgrades
der Mathematisch-Naturwissenschaftlichen Fakultät
der Heinrich-Heine-Universität Düsseldorf

vorgelegt von

Marko Filipović
aus Düsseldorf

Düsseldorf, Dezember 2023

aus dem Institut für Theoretische Physik I
der Heinrich-Heine-Universität Düsseldorf

Gedruckt mit der Genehmigung der
Mathematisch-Naturwissenschaftlichen Fakultät der
Heinrich-Heine-Universität Düsseldorf

Berichterstatter:

1. Prof. Dr. Alexander Pukhov
2. Prof. Dr. Dr. Carsten Müller

Tag der mündlichen Prüfung: 23.04.2024

Abstract

The swift progress of high-intensity lasers has opened new avenues for exploring light-matter interactions, particularly in the field of quantum electrodynamics (QED). High-intensity laser-plasma interactions provide an ideal platform for probing QED processes as they generate strong electromagnetic fields and facilitate ultra-relativistic particle acceleration. This research utilises particle-in-cell (PIC) code simulations to investigate QED phenomena under such conditions, focusing on three distinct studies involving intense fields to prepare future experiments.

The first part of the research presents a Maxwell solver improving one-dimensional field propagation simulations. It is demonstrated that the solver effectively suppresses the numerical Cherenkov instability while minimizing energy losses and self-interactions in the propagation of an ultra-relativistic electron bunch. In a next step, the radiation reaction force, typically encountered in strong fields, is introduced. The influence of the force will be discussed in regards of energy losses and beam dynamics. The second part examines QED effects in the collision of electron bunches with laterally shifted propagation axes. Due to the shift a higher number of electrons experience the strong field of the counter-propagating beam. The configuration yields higher γ-photon emission and a subsequent higher number of decays into electron-positron pairs. However, fewer particles reach the conjectured nonperturbative QED regime, which is currently not experimentally feasible. The third part proposes an experimental setup for future QED investigations. This design incorporates two linearly polarized lasers, which approach a solid-state target under a small angle. Due to the small angle electrons are extracted and accelerated from the surface. As electrons reach the intersection of the laser propagation axes, they engage with counter-propagating beams, potentially leading to a QED cascade under strong field conditions. Subsequently, the study investigates the influence of various parameters on particle spectra and yields, focusing on the intensity of the lasers and the angle between the target and the laser.

Zusammenfassung

Der rasche Fortschritt in der Entwicklung von Hochintensitätslasern hat neue Wege zur Erforschung der Licht-Materie-Wechselwirkung erschlossen, insbesondere im Bereich der Quantenelektrodynamik (QED). Hochintensive Laser-Plasma-Interaktionen bieten eine ideale Plattform für die Untersuchung von QED Prozessen, da sie starke elektromagnetische Felder generieren und die ultra-relativistische Beschleunigung von Teilchen ermöglichen. Diese Forschungsarbeit nutzt Simulationen mit Hilfe eines Particle-in-Cell (PIC)-Code, um QED Phänomene unter solchen Bedingungen zu untersuchen, wobei der Schwerpunkt auf drei verschiedenen Studien liegt, die intensive Felder nutzen, um zukünftige Experimente vorzubereiten.

Der erste Teil der Forschung stellt einen verbesserten Maxwell-Solver für Simulationen mit eindimensionaler Feldausbreitung vor. Es wird demonstriert, dass der Solver die numerische Tscherenkow-Instabilität effektiv unterdrückt, während er gleichzeitig Energieverluste und Selbstinteraktionen bei der Ausbreitung eines ultra-relativistischen Elektronenbündels minimiert. In einem nächsten Schritt wird die Strahlungsrückwirkungskraft hinzugefügt, die typischerweise in starken Feldern auftritt. Der Einfluss der Kraft wird hinsichtlich Energieverlusten und Teilchen-Dynamiken diskutiert. Der zweite Teil befasst sich mit der Untersuchung von QED Effekten beim Zusammenstoß von Elektronenbündel, deren Ausbreitungsachsen zueinander transversal verschoben sind. Aufgrund der transversalen Verschiebung sind mehr Elektronen dem starken Feld des entgegenlaufenden Strahls ausgesetzt. Diese Konfiguration resultiert in einer erhöhten γ-Photonenemission und in der Folge in einer angestiegene Anzahl an Zerfällen in Elektron-Positron-Paare. Allerdings erreichen weniger Teilchen das postulierte nichtperturbative QED-Regime, welches derzeit experimentell nicht realisierbar ist. Der dritte Teil schlägt eine experimentelle Anordnung für zukünftige QED Untersuchungen vor. Dieses Design beinhaltet zwei linear polarisierte Laser, die einem Festkörper unter einem kleinen Winkel nähern und Elektronen aus dem Körper extrahieren und beschleunigen. Wenn die Elektronen den Schnittpunkt der Ausbreitungsachsen der Laser erreichen, interagieren sie mit den entgegenlaufenden Feldern, was potenziell zu einer QED Kaskade unter starken Feldbedingungen führen kann. Nachfolgend untersucht die Studie den Einfluss verschiedener Parameter auf die Partikelspektren und -ausbeuten, wobei der Schwerpunkt auf dem Winkel zwischen dem Festkörper und dem Laser sowie der Intensität der Laser liegt.

Contents

1 Introduction

In modern physics, the exploration of quantum electrodynamics (QED) is an experimentally challenging frontier, presenting physicists with great obstacles. They rely on developing new tools and theories to overcome these. With the advent of high-energy particle beams, high-intensity laser systems, and numerical simulation tools, new avenues for probing the complex theory of QED processes in regimes previously experimentally inaccessible have opened.

The development of lasers began with theoretical groundwork done by Albert Einstein, who proposed the process of stimulated emission [1]. This concept was brought to fruition with the creation of the first working laser by Theodore H. Maiman [2]. Since then, lasers have been deployed in nearly every aspect of life. Lasers provide coherence and monochromaticity, which are especially useful in scientific experiments such as trapping [3] and laser interferometry [4].
One significant breakthrough that has revolutionized the field is Chirped Pulse Amplification (CPA) [5], which has lead to continuous increase in peak intensities from $\sim 10^{15}$W cm^{-2} upward. This technique has been crucial in enabling interactions with matter and unlocking a new domain of high-intensity physics.
Leading the frontier are major laser facilities such as ELI [6], SULF [7] and many more [8–12], where CoReLS is the leading facility with a current peak intensity of $\sim 10^{23}$W cm^{-2} [13]. These facilities are not only impressive in their engineering but also serve as tools for physicists, offering a wide array of experimental setups that can be used to explore diverse physics[14].
High-intensity lasers have been instrumental in exploring plasmas, leading to groundbreaking discoveries in high-energy density physics [15–17], especially laser-driven fusion [18, 19] and particle acceleration [20–22]. Laser-plasma interaction has not only deepened the understanding of fundamental processes but also spurred numerous practical applications, ranging from materials processing [23, 24] to medical technologies [25, 26].

While laser technologies have been developing, parallel advancements have been made in the area of particle accelerators. These machines accelerate particles to nearly the

speed of light, creating high-energy conditions needed for advanced studies. The types of particle accelerators vary widely, including linear accelerators like SLAC [27, 28], synchrotrons like the Large Hadron Collider (LHC) [29], and cyclotrons like FRIB [30]. High-energy charged particle beams serve as essential instruments for probing the fundamental tenets of physics. These beams are employed in experimental settings to investigate the Standard Model [31], explore the architecture of matter [32], and produce rare atomic nuclei[33].

By combining both high-intensity lasers and high-energy electrons, researchers are poised to explore uncharted territories in light-matter interactions. A more comprehensive understanding of radiation reaction [34, 35], an aspect of electrodynamics that remains incompletely understood [36], can be researched with these lasers and electrons. Radiation reaction is the force a charged particle experiences as a consequence of radiation losses due to its acceleration in an intense field. Shifting finally to QED theory, the radiation reaction becomes less important with stronger fields. In the description of QED theory the radiation losses can be explained by the emission of high-energy photons by charged particles. Theses photons can then decay to an electron-positron pair, which influence plasma dynamics and is of a great interest for further study. As research has been conducted in this field it is predicted that high-energy electrons play a critical role in investigating the frontier of QED [37–40] and anticipate that the theory transitions into a fully nonperturbative regime [41–43]. But the lack of experimental tools is the reason why the research slows down at times and facilities try to reach higher laser intensities or accelerate charged particles to higher energies.

However, experiments are unable to provide all the answers and physics research is therefore supported by numerics. One of the primary computational method for examining the interactions between high-energy charged particles and electromagnetic fields is the particle-in-cell (PIC) [44, 45] technique. This method is recognized as a fundamental approach for studying a wide variety of topics. These include interactions between lasers and relativistic plasmas [46–49], plasma-based acceleration [50, 51], and astrophysical phenomena involving relativistic conditions [52, 53]. Within the PIC framework, matter is represented as a collection of macro-particles. These macro-particles are moved according to relativistic equations of motion. The resulting charge currents then serve to update the electromagnetic fields, thereby enabling a self-contained representation of the interactions [44]. These fields are typically updated using finite-difference time-domain (FDTD) algorithms. Yee was among the pioneers in proposing a staggered grid for solving the Maxwell equations using this approach [54].
This computational approach provides a robust framework for studying laser-plasma interaction under relativistic conditions. PIC simulations can be extended for various

cases, allowing for the fine-tuning of conditions to isolate specific events or phenomena for detailed study.

As may already have become apparent, the present thesis aims to delve into configurations for the study of QED events, focusing primarily on nonlinear Compton scattering [55] and multi-photon Breit-Wheeler pair production [56]. These phenomena, as already established, have remained largely unexplored in experimental setups, partly due to the limitations in generating high-intensity laser fields and energetic particle beams. However, with upcoming potential parameters in sight, QED processes will soon become accessible for investigation.
The thesis examines this topic by using PIC simulations and extending the existing PIC-code `VLPL` [45, 57]. Developed numerical tools, implemented in the existing PIC-code, offer insights into potential methodologies for studying QED effects. Concerning numerical instabilities are studied as well as they may threaten the results of the simulations. Afterwards, understanding QED effects in possible configurations enabled by innovations in particle accelerators and high-energy laser facilities is investigated. An existing scheme, namely a head-on collision of ultrarelativistic bunches, modified for study of QED processes, is considered. The other configuration involves high-intensity lasers incident on a solid-state target at a grazing angle. Here, an abundant production of secondary particles due to QED processes is examined.
Eventually, the introduction of these configuration can be used in new experiments once the currently build laser facilities are finished and give insight on experimentally unexplored regimes.

1.1 Outline

The thesis is structured as follows. Chapter 2 is an overview of the underlying physics discussed throughout the thesis. Topics that will be addressed are general properties of plasma and high-energy laser-plasma interactions. Afterwards, radiation processes in the classical regime are explained and the chapter concludes with an overview of the complex regime of strong-field QED. Here, processes like the high-energy photon emission and the decay of such a photon into an electron-positron pair are a likely occurrence. In a sufficiently strong field, the repetition of photon emission and pair production may lead to development of a QED cascade resulting in a build up of an electron-positron plasma. The following chapter 3 targets the methods and algorithms used in this thesis. Here, the particle-in-cell (PIC) method will be described and its extension through various physical modules and merging algorithms. Benchmarks for

the merging algorithm will be shown as well. These introductory chapters are followed by the main part containing three chapters. The main chapters are devoted to the research topics conducted by the author. The first topic tackles the suppression of non-physical radiation losses in chapter 4. It is important to suppress non-physical behaviour in the upcoming simulations, since additional strong-fields could increase secondary particle production and alter the final result. Next up, in chapter 5 a previously introduced head-on bunch collision configuration is investigated under a modification of the author. The effects of the introduced modification are studied and its impact on reaching the fully nonperturbative QED regime is discussed. Finally in chapter 6, a second configuration is investigated. Extraction and acceleration of electrons from a solid-state target irradiated with a high-intensity laser is researched. Here, the production of secondary particles due to QED processes during the interaction of the extracted electrons with a counter-propagating laser is discussed. The thesis finishes with a conclusion on the topics in chapter 7.

1.2 Publication in peer-reviewed journals

The specific contributions are given at the end of the summary of each chapter. Following studies have passed a peer-review process:

- **M. Filipovic**, C. Baumann, A. M. Pukhov, A. S. Samsonov and I.Yu. Kostyukov, *Effect of transverse displacement of charged particle beams on quantum electrodynamic processes during their collision, Quantum Electronics* **51** *807*(2021)

- A. S. Samsonov, E. N. Nerush, I. Yu. Kostyukov, **M. Filipovic**, C. Baumann and A. Pukhov, *Beamstrahlung-enhanced disruption in beam–beam interaction, New Journal of Physics* **23** *103040*(2021)

- **M. Filipovic**, C. Baumann, and A. Pukhov, *Suppression of errors in simulated ultrarelativistic bunch propagation using the X-dispersionless Maxwell solver, Physical Review Accelerators and Beams* **25**, *054405*(2022)

- **M. Filipovic** and A. Pukhov, *QED effects at grazing incidence on solid-state targets, European Physical Journal D* **76**, 187 (2022)

- A. S. Samsonov, I. Yu. Kostyukov, **M. Filipovic**, and A. Pukhov, *Generation of electron–positron pairs upon grazing incidence of a laser pulse on a foil*. Kvantovaya Elektronika, **53**(2), *160-164*, (2023).

1.2.1 Proceedings

Following proceeding has been published;

- L. Reichwein, **M. Filipovic**, X. F. Shen, K. Jiang, C. Baumann, and A. Pukhov, *Interaction of Extremely Intense Flows of Electromagnetic Energy and QED Processes in Supercritical Fields*, published for the NIC Series (2022).

2 Underlying Theory

Within the following chapter, the important theory, which appears in this study, is discussed in detail. First, an in-depth overview of the physics and characteristics of a plasma will be elaborated (see section 2.1). Subsequently, the chapter delves into the influence of radiation losses on ultra-relativistic electrons, presented within a classical framework (see section 2.3). The chapter concludes with a comprehensive description of the QED effects examined in this study (see section 2.4). The content of this chapter is an overview of the books on plasma theory and lectures [58–61].

2.1 Plasma

Regarded as the fourth fundamental state of matter, alongside solids, liquids, and gases, plasma is a macroscopically neutral ensemble of unbound positive and negative particles, comprised of ions and free electrons. Plasma is therefore called quasineutral, since at microscopical lengths charge imbalances can be present, but observing it from afar and as a whole the medium is neutral. Each particle exhibits influence on the neighbouring particles via long-range electromagnetic forces. Due to their constant interaction various collective behaviors are observed in plasma. There are certain criteria that must be met in order to qualify a gas of ions and electrons as plasma. To define them, some insight into the behaviour of plasma is required.

2.1.1 Debye shielding

One of the most important features of a plasma is the so-called Debye shielding. As plasma consists of free charged particles, it possesses the ability to neutralize charge imbalances. This allows it to effectively shield charges that are introduced externally. Quasineutrality describes that the plasma may have differences in charge if locally observed, but overall plasma is electrically neutral. In general, plasma tries to compensate any charge imbalances to shield their electrostatic fields.

Coming back to introducing a charge into the plasma enables one to define the shielding process in more detail. As a test charge q is placed in a plasma consisting of electrons and protons, on one hand charges with the same charge as the test-charge are pushed back. On the other hand, charges with the opposite charge are attracted. Therefore, the charge will be shielded. To explain this effect, the distribution of charges in the plasma can be analyzed using the Poisson equation. The shielding described by the Poisson equation reads

$$\nabla^2\phi = -4\pi\left(q\delta\left(\mathbf{r}\right) + e\left(n_p - n_e\right)\right), \tag{2.1.1}$$

with ϕ representing the electric potential, $q\delta\left(\mathbf{r}\right)$ denotes a charge density of a point-charge in the origin, here test-charge q, e is the elementary charge and n_p and n_e being the density of protons and electrons respectively. Supposing that the electrons in potential ϕ have Boltzmann distribution

$$n_e = n_0 \exp\left(\frac{e\phi}{k_B T}\right), \tag{2.1.2}$$

with n_0 is the unperturbed plasma density, k_B is the Boltzmann constant and T being the temperature of electrons. Due to the large mass of protons it can be assumed that they are immobile at a typical time-scale of electron interaction. Assuming that the argument of the exponential function is $e\phi/\left(k_B T\right) \ll 1$ the electron distribution can be Taylor expanded and inserted into equation 2.1.1 leading to

$$\left(\Delta - \frac{1}{\lambda_D^2}\right) = -4\pi q\delta\left(\mathbf{r}\right), \tag{2.1.3}$$

with $\Delta = \nabla^2$ and

$$\lambda_D = \sqrt{\frac{k_B T}{4\pi n e^2}} \tag{2.1.4}$$

denotes Debye length. The Debye length describes the distance at which the potential drops to the order of $1/e$ of the initial potential. Performing a Fourier transformation obtains the solution to the Poison equation 2.1.3 and reads

$$\phi = \frac{q}{r}\exp\left(-\frac{r}{\lambda_D}\right). \tag{2.1.5}$$

This solution allows us to see that placing a test-charge in plasma will lead to the potential being shielded off. Additionally, the argument of the exponential function shows, that the potential decreases faster as a Coulomb potential with $\phi \propto 1/r$.

Understanding Debye shielding results in following additional criteria for classifying a medium as plasma. First, the extent of the plasma system needs to be larger than the Debye length, $\lambda_D \ll L$. Second, the number of particles in the volume to shield test-particles N_D has to be very large

$$N_D = \frac{4}{3}\pi\lambda_D^3 n_0 \gg 1. \tag{2.1.6}$$

2.1.2 Plasma frequency

As the key feature of plasma has been described, it is of interest to understand certain motions of plasma. Here, the notions of two new parameters, plasma frequency and critical density, merit discussion. In the case that one of the particles species, for example electrons, are shifted within the plasma, an electric field is induced between the different charged particles. This displacement leads to oscillation of the electrons within the plasma, as the plasma tries to restore the quasineutrality. The plasma frequency ω_p is a measure of how these oscillations in charge imbalances are restoring neutrality in plasma. To derive the frequency, one begins with Ampère's Law

$$\nabla \times \mathbf{B} = \frac{1}{c}\frac{\partial \mathbf{E}}{\partial t} + \frac{4\pi}{c}\mathbf{J} \tag{2.1.7}$$

and with no magnetic field present, $\mathbf{B} = 0$, eq. 2.1.7 simplifies to

$$-\frac{4\pi}{c}\mathbf{J} = \frac{1}{c}\frac{\partial \mathbf{E}}{\partial t}. \tag{2.1.8}$$

Here, $\mathbf{J}$ is the current density and reads

$$\mathbf{J} = -en\mathbf{v}, \tag{2.1.9}$$

where n is the number density of electrons and $\mathbf{v}$ is the velocity of the electrons. The motion of an electron under the influence of an electric field is described by

$$m_e\frac{d\mathbf{v}}{dt} = -e\mathbf{E}, \tag{2.1.10}$$

with m_e the electron mass. Next, it is assumed that the velocity $\mathbf{v}$ and the electric field $\mathbf{E}$ are small perturbation, so the equation can be linearized. Substituting the current density in Ampère's Law leads to

$$\frac{4\pi en}{c}\mathbf{v} = \frac{1}{c}\frac{\partial \mathbf{E}}{\partial t}. \tag{2.1.11}$$

To be able to substitute eq. 2.1.11 in the equation of motion another approximation is required. The total time derivative reads in detail

$$\frac{d\mathbf{v}}{dt} = \frac{\partial v\mathbf{v}}{\partial t} + (\mathbf{v}\cdot\nabla\mathbf{v}). \tag{2.1.12}$$

Assuming that a homogeneous and stationary plasma is at hand and perturbations are small the spatial derivatives can be neglected. The total time derivative approximates to $\partial\mathbf{v}/\partial t$.

Taking the time derivative of the equation of motion for electrons

$$\frac{\partial}{\partial t}\left(m\frac{\partial \mathbf{v}}{\partial t}\right) = -e\frac{\partial \mathbf{E}}{\partial t} \tag{2.1.13}$$

finally allows the substitution of eq. 2.1.11 into it, which transforms to

$$m\frac{\partial^2 \mathbf{v}}{\partial t^2} = -4\pi n e^2 \mathbf{v}. \tag{2.1.14}$$

For a sinusoidal velocity $\mathbf{v} \sim \exp(i\omega_p t)$ the transformed equation above becomes

$$-m\omega_p^2 \mathbf{v} = -4\pi n e^2 \mathbf{v}. \tag{2.1.15}$$

This equation can be solved for the plasma frequency ω_p:

$$\omega_p = \sqrt{\frac{4\pi n e^2}{m_e}}, \tag{2.1.16}$$

Plasma frequency is an essential parameter because it sets the timescale for many plasma processes, including wave propagation and scattering phenomena.

2.1.3 Electromagnetic waves in plasma

Due to the focus on laser-plasma interaction in the thesis it is important to examine the interplay between light waves and the plasma. Interaction between those can be connected by the dispersion relation of light waves in a plasma

$$\omega^2 = \omega_p^2 + c^2 k^2, \tag{2.1.17}$$

with ω the angular frequency of the light wave, c the speed of light and k the wave number. The dispersion relation shows us that only waves with a frequency ω_0 greater than the plasma frequency are able to propagate through a plasma. The physical reason is that electron oscillations cannot keep up with the wave as their response time is slower than the fast oscillation of the wave. But if the wave frequency is smaller than the plasma frequency, the electrons can respond to reflect the incoming wave. In this case, k becomes imaginary.

In such cases the skin depth l_s is the most important parameter to see how far a wave can enter the plasma and is described as

$$l_s = \frac{c}{\sqrt{\omega_p^2 - \omega_0^2}}. \tag{2.1.18}$$

As a second quantity to see, whether waves can penetrate plasma a description void of the plasma frequency is desirable. This quantity is the critical density n_{cr}, the density at

which the plasma frequency equals the frequency of an externally applied electromagnetic wave. In this case n_{cr} is the density of which a wave of frequency ω_0 can propagate through the plasma. It can be represented as

$$n_{\mathrm{cr}} = \frac{m_e \omega_p^2}{4\pi e^2} \approx \frac{11.15 \times 10^{12}}{(\lambda_0/\mathrm{cm})^2} \mathrm{cm}^{-3} \tag{2.1.19}$$

Again, if $n_e < n_{\mathrm{cr}}$ the plasma is transparent and called under-dense, where as $n_e > n_{\mathrm{cr}}$ the plasma is opaque and called over-dense for waves with a frequency of ω_0. The concept of critical density is crucial in applications like controlled fusion and plasma diagnostics. It is also an important normalization unit in numerical simulation and allows, at a glance to determine, if a plasma is opaque or transparent for a light with a frequency of ω_0.

2.2 Laser pulses

After covering one of the main topics of the theory in this thesis the second major part is laser pulses and their fields. It is important to provide some insight as one of the chapters will dive into laser-plasma interaction. This section will display only some aspects of the very broad subject of lasers. The content of this chapter is knowledge from books on laser pulses and lectures on electrodynamics [62–67], where a more in-depth description can be found.

To define a laser pulse, it is required that the pulse be a solution of the wave equation

$$\left(\Delta - \frac{1}{c^2}\frac{\partial^2}{\partial t^2}\right)\mathbf{E} = \vec{0}, \tag{2.2.1}$$

where $\Delta = \nabla^2$ denotes the Laplace operator and $\mathbf{E}$ the electric field vector. This equation describes the behaviour of electromagnetic waves in a vacuum.

Among various types of laser pulses, the thesis is mainly interested in Gaussian pulses due to their wide applicability and use within experiments. The main characteristic of such a pulse is the usage of a Gaussian distribution within its spatial and temporal profile. For a Gaussian pulse the electric field reads

$$E(r,z,t) = E_0 \frac{w_0}{w(z)} \exp\left[-\frac{r^2}{w(z)} - ikz - \frac{ikr^2}{2R(z)} + i\zeta(z)\right] \exp(i\omega t). \tag{2.2.2}$$

Here, E_0 is the peak amplitude, $w = w_0\sqrt{1+\left(\frac{z}{z_R}\right)^2}$ is the beam waist with $z_R = \pi w_0^2/\lambda_0$ the Rayleigh length, where λ_0 is the wavelength of the light and w_0 defines the focal spot

size. Further, $k = 2\pi/\lambda_0$ denotes the wavenumber and $R(z) = z\left[1 + \left(\frac{z_R}{z}\right)^2\right]$ being the radius of curvature. The final parameters of the eq. 2.2.2 are $\zeta(z) = \arctan(z/z_R)$ as the Gouy phase shift and ω the angular frequency of the pulse.

An important parameter which describes the strength of a laser and summarizes the most important quantities is the normalized laser vector potential or dimensionless vector potential

$$a_0 = \frac{eE_L}{m_e c \omega_0}. \tag{2.2.3}$$

The parameter demonstrates that as soon as a_0 exceeds unity the electron enters the relativistic regime. Specifically, it describes an electric field of strength E_L that accelerates an electron to an energy of $m_e c^2 \sqrt{1 + a_0^2}$ over the length of reduced wavelength $\lambda_0/(2\pi)$. The parameter can be cast into a form containing the peak intensity of a wave I_0 and reads

$$a_0 = \lambda_0 [\mu\text{m}] \times \sqrt{\frac{I_0 \left[\text{W cm}^{-2}\right]}{1.37 \times 10^{18} \times \zeta}} \tag{2.2.4}$$

with ζ the polarization of the wave. A $\zeta = 1$ would describe a linearly polarized wave, whereas a $\zeta = 2$ would be a circularly polarized wave.

2.3 Classical radiation reaction

So far, accelerating electrons to the relativistic regime has been described, but it also needs to be considered that electrons emit radiation within strong fields. In classical electrodynamics, the motion of an electron is not only influenced by the Lorentz force. An extra force accounts for the energy and momentum loss of an accelerated electron that emits electromagnetic waves. As a result, the trajectory of the electron is altered from the predicted one by Lorentz force alone. This phenomenon is considered as radiation reaction or short RR. One of the earliest historical descriptions of this force employs the Larmor formula [68]

$$P_L = \frac{2}{3} \frac{e^2}{m_e^2 c^3} \left(\frac{d\mathbf{p}}{dt}\right)^2. \tag{2.3.1}$$

This equation defines the power of the emitted radiation by an electron under an external force. It is necessary to include a radiation reaction dampening force since its recoil is not captured by the Lorentz force, which reads

$$\mathbf{F}_\text{L} = q\left(\mathbf{E} + \frac{\mathbf{v}}{c} \times \mathbf{B}\right), \tag{2.3.2}$$

with $\mathbf{F}_L$ the force of electromagnetic fields. The additional force can be encapsulated by the Lorentz-Abraham equation, the force experienced by a charged particle due to radiation reaction

$$\mathbf{F}_{\text{rad}} = \tau \frac{\mathrm{d}\mathbf{F}}{\mathrm{d}t} \tag{2.3.3}$$

with $\tau = \frac{2}{3}\frac{q^2}{mc^3}$ the time scale of radiation reaction. The problem of this equation is that it is not ideal, as it produces inconsistent runaway solutions. In order to find a better description the Landau-Lifshitz approach [35] in its covariant form

$$\mathbf{f}^{\mu}_{\text{LL}} = \frac{2q^3}{3mc^2}\left(\partial_\alpha F^{\mu\nu} u_\nu u^\alpha\right) + \frac{2q^4}{3m^2c^4}\left[F^{\mu\nu}F_{\nu\alpha}u^\alpha + \left(F^{\nu\beta}u_\beta F_{\nu\alpha}u^\alpha\right)u^\nu\right], \tag{2.3.4}$$

is able to eliminate most issues, where u^μ is the particle four-velocity and $F^{\mu\nu}$ being the electromagnetic tensor.

2.4 Strong-field quantum electrodynamics

Reaching even stronger fields will require to move on to a quantum mechanical description. The quantum non-linearity parameter is an important quantity to classify the regime and determine the occurrence of various processes in this regime. The parameter is defined as

$$\chi = \frac{e\hbar}{m^2c^3}\sqrt{\left(\gamma\mathbf{E} + \frac{\mathbf{p}}{mc}\times\mathbf{B}\right)^2 - \left(\frac{\mathbf{p}}{mc}\cdot\mathbf{E}\right)^2} = \frac{E_{\text{rest}}}{E_{\text{crit}}} \tag{2.4.1}$$

with $E_{\text{crit}} = m_e^2c^3/(e\hbar) \simeq 1.3\times10^{16}\text{Vcm}^{-1}$ being the critical field of QED [69]. The critical field, also known as the Schwinger limit [69], describes a limit for vacuum breakdown and the point at which the theory becomes nonlinear. The quantum non-linearity parameter can be perceived as the ratio of the electric field a charged particle experiences in its own rest frame to the critical field. If the quantum non-linearity parameter exceeds unity for a charged particle, QED effects become important.

As a support to understand quantum processes in the following and to implement numerically, an assumption is necessary. Typical fields are complex because they vary in time and space making calculations difficult. An assumption that can be made is that particles regard the local field as constant. This assumption is the locally constant-field approximation [55, 70]. It can be employed if the pair-formation length $l_C = \hbar/mc^2$ is much smaller than the field related length λ_0. Therefore, one can just use the local value of χ.

The obvious choice to apply this approximation is to establish a static magnetic field [55] or a constant-crossed field, where the fields are perpendicular to each other and have the

same magnitude. The latter case is of special interest as it helps to model laser-plasma interaction for relativistic particles.

With this assumption the key QED effects in this thesis will be described in the following subsections.

2.4.1 Nonlinear Compton scattering

One of the fundamental QED processes affecting a charged particle is the emission of radiation due to acceleration in an external field. The name of the process is the nonlinear Compton scattering, but it can be also described as the quantum synchrotron radiation.

To observe this process, no specific initial energy or intensity requirement needs to be met. The direction of the momentum of a photon emitted by a particle with $\gamma \gg 1$ is nearly parallel to the propagation direction of the emitting particles. The direction is defined by a cone with an opening angle of $\sim 1/\gamma$ [71].

A description of the process for an electron can be

$$e^- + n\hbar\omega \rightarrow e^- + \gamma, \tag{2.4.2}$$

with e^- as an ultra-relativistic electron interacting with a number of n photons $\hbar\omega$ provided by an external field.

The energy distribution of the probability rate of this process is given by

$$\frac{dW_{\mathrm{rad}}\left(\varepsilon_\gamma\right)}{d\varepsilon_\gamma} = -\frac{\alpha m^2 c^4}{\hbar\varepsilon_e^2}\left\{\int_x^\infty \mathrm{Ai}\left(\xi\right)d\xi + \left(\frac{2}{x}+\chi_\gamma\sqrt{x}\right)\mathrm{Ai}'\left(x\right)\right\} \tag{2.4.3}$$

with $x = \left(\chi_\gamma/\chi_e\chi_e'\right)^{2/3}$, $\mathrm{Ai}\left(x\right) = \left(1/\pi\right)\int_0^\infty \cos\left(\xi^3/3+\xi x\right)d\xi$ the Airy function, $\chi_e' = \chi_e - \chi_\gamma$ and ε_e and ε_γ the energy of the initial electron and emitted photon respectively [72, 73]. Examining the energy distribution of the probability rate, it is clear that the equation describes the process of an electron with energy ε_e losing energy and becoming an electron, which emitted a photon of energy ε_γ. Through integration of 2.4.3 one can derive the total emission rate [74]

$$W_{\mathrm{rad}} = \int_0^{\varepsilon_e}\frac{dW_{\mathrm{rad}}\left(\varepsilon_\gamma\right)}{d\varepsilon_\gamma}\mathrm{d}\varepsilon_\gamma = \frac{\alpha}{3\sqrt{3}\pi}\frac{mc^2}{\hbar\gamma}\int_0^\infty \frac{5x^2+7x+5}{\left(1+x\right)^3}K_{2/3}\left(\frac{2x}{3\chi}\right)\mathrm{d}x \tag{2.4.4}$$

with $K_{2/3}(\cdot)$ the modified Bessel function of the second kind. Taking the inverse of the equation 2.4.4 describes the photon emission time by an ultra-relativistic electron. The

photon emission time estimates the time between two emission processes of a particle. Should the implementation of this process be considered it is preferred to suppress the integral expression in 2.4.4. In order do that, one can use a precalculated table for various integral solutions. The upper limit of the integration cannot be higher than the initial electron energy ε_e. Here the total emission rate can be described by using asymptotic expressions in the limit of a large quantum non-linearity parameter [72]

$$W_{\text{rad}} \approx 1.46 \frac{\alpha m_e^2 c^4}{\hbar \varepsilon_e} \chi_e^{2/3}, \chi_e \gg 1. \tag{2.4.5}$$

2.4.2 Multi-photon Breit-Wheeler pair production

The second important QED process focused on is the conversion of a high-energy photon into an electron-positron pair, also known as the multi-photon Breit-Wheeler pair production process [56]. Similar to the nonlinear Compton scattering process one can establish the energy distribution of the probability rate by hard photons, photons with an energy of $\varepsilon_\gamma \gg mc^2$, which reads

$$\frac{dW_{\text{pair}}(\varepsilon_e)}{d\varepsilon_e} = \frac{\alpha m^2 c^4}{\hbar \varepsilon_\gamma^2} \left\{ \int_x^\infty \text{Ai}(\xi)\, d\xi + \left(\frac{2}{x} - \chi_\gamma \sqrt{x} \right) \text{Ai}'(x) \right\}, \tag{2.4.6}$$

with $x = \left(\chi_e / \chi_\gamma \chi_\gamma' \right)^{2/3}$ [72, 75]. In this case the equation 2.4.6 describes the positron created by the process. Again, integrating the equation 2.4.6 yields the total rate for the process, which is here

$$W_{\text{pair}} = \frac{\alpha}{3\sqrt{3}\pi} \frac{m^2 c^4}{\hbar \varepsilon} \int_0^1 \frac{9 - x^2}{1 - x^2} K_{2/3} \left(\frac{8 m c^2 E_{\text{crit}}}{3(1 - x^2)\hbar \omega B} \right) \text{d}x. \tag{2.4.7}$$

For a simpler equation, equation 2.4.7 can be rewritten with an asymptotic expression for the limit of large χ_γ

$$W_{\text{pair}} \approx 0.38 \frac{\alpha m^2 c^4}{\hbar \varepsilon_\gamma} \chi_\gamma^{2/3}, \chi_\gamma \gg 1. \tag{2.4.8}$$

Taking the inverse of the total pair-creation rates 2.4.7 and 2.4.8 gives one the pair production time, the time until a photon with high enough energy converts to an electron-positron pair [72].

2.4.3 Neglected processes

These above mentioned processes are by far not the only QED effects that are important and occur at this fields. Additional effects are the pair annihilation to one photon as well as the absorption of a photon by an electron or positron in a strong external field [71, 76].

Both of these processes are neglected due to the assumption of constant crossed fields, as these processes are suppressed by the aforementioned process of nonlinear Compton scattering and pair production. Additionally, to simulate such processes the collision angle Θ between for an example an electron-positron pair for annihilation needs to be $\Theta \leq 10^{-5}$rad [71, 76].

3 Numerical tools and algorithms

To understand physical phenomena in complex situations, numerical tools are a great method to fully understand the mechanics behind it. Specifically for plasma dynamics and laser-plasma interaction, the toolset provided by particle-in-cell codes, in short PIC codes, is a great way to obtain results. Because of that, this chapter will first give an introduction to the PIC method in its basic form and explain further how to implement classical synchroton radiation, quantum-electrodynamic processes relevant in the high-energy regime and mitigation of abundance of macro-particles by QED processes to prevent ever increasing computational loads. These algorithms are deployed in the code `VLPL` developed by A. Pukhov [45, 57]. The merging module, which has been implemented throughout the thesis in the current version of `VLPL` are tested in the respective subsection.

3.1 General concept of PIC codes

PIC codes tackle a problem with plasma interaction. As it was previously established, plasma consists of a great number of particles (see section 2.1). If one were to consider simulating each particle in an electromagnetic field, the simulation will require a vast number of calculations to retrieve new particle positions and updated momenta. There are three key points the PIC codes generally need to accomplish. Firstly, in order to minimize the computational effort particles should be summarized into macro-particles, a charge density of particles. Theses macro-particles must abide by the same physical laws as particles not grouped. In doing so the number of calculations is significantly reduced and even becomes practicable on slower computer cores. Secondly, electromagnetic

fields need to be updated for the ongoing simulation. Therefore, the Maxwell equations

$$\nabla \times \mathbf{E} = -\frac{1}{c}\frac{\partial \mathbf{B}}{\partial t} \tag{3.1.1}$$

$$\nabla \times \mathbf{B} = \frac{1}{c}\frac{\partial \mathbf{E}}{\partial t} + \frac{4\pi}{c}\mathbf{J} \tag{3.1.2}$$

$$\nabla \cdot \mathbf{E} = 4\pi\rho \tag{3.1.3}$$

$$\nabla \cdot \mathbf{B} = 0 \tag{3.1.4}$$

need to be solved numerically. But in doing so errors are often introduced. Most Maxwell solvers have cases where they suppress errors in certain situations [45, 77–79], while others introduce only a general small error [80]. Finally, the particles need to undergo a momentum change once a force is applied to them. Here, particle pusher algorithms are used and expanded with additional modules.

These key points will be explained briefly in the following sections, but an extensive description for PIC codes can be found in [44].

3.1.1 The Vlasov equation

As a starting point for the PIC code it is important to understand the kinetics [57]. Here, the requirement is to find a source term which is the current density $\mathbf{j}$. To acquire this source term, the description of the distribution function

$$F^N(\mathbf{x}_1, \mathbf{p}_1, ..., \mathbf{x}_N, \mathbf{p}_N) \tag{3.1.5}$$

is necessary, with $\mathbf{x}_n$ the position and $\mathbf{p}_n$ the momentum of the n-th particle. It has been shown, that the single-particle distribution $f(\mathbf{x}, \mathbf{p}, t)$ for each species in the system is needed to have the information for the full system. The Boltzmann-Vlasov equation gives then the evolution of the single particle distribution in the following:

$$\frac{\partial f}{\partial t} + \frac{\mathbf{p}}{m\gamma}\nabla f + \frac{\mathbf{F}}{m}\nabla_p f = \mathrm{St} \tag{3.1.6}$$

Here, St is the collisional term. In the next step, this equation must be solved, but due to the complex nature of the equation solving it analytically will lead to a high computational cost.

Solving the partial differential equation can be done in two different ways. The first approach involves using finite differences in a grid structure of the phase space. Using this approach is straightforward, but harbors a great problem. This method requires

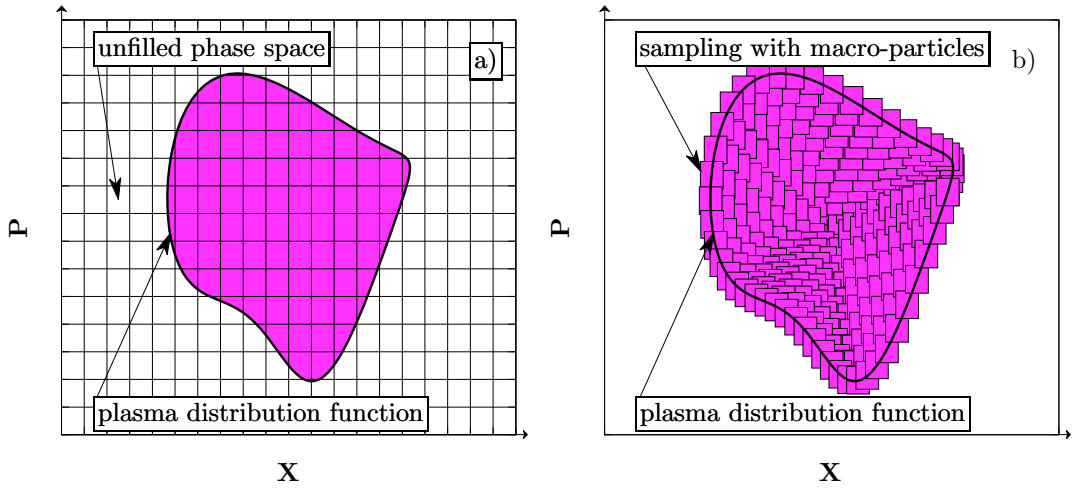

Figure 3.1.1: a) shows the plasma function distribution in a regular phase space at a certain time. b) Here, the plasma distribution function is sampled by numerical macro-particles.

intensive calculations and a massive amount of computational resources. Lots of the calculations might get "wasted" when considering phase space where no particles are present as figure 3.1.1 a) demonstrates. The grid spans across the whole phase space, including unfilled phase space.

Therefore, an additional simplification is necessary to solve the six-dimensional equation [57].

Introducing the finite element method allows to approximate the single-particle distribution function with finite phase-fluid elements

$$f(x,p) = \sum_n W_n^{ph} S^{ph}(x - x_n, p - p_n) \tag{3.1.7}$$

where W_n^{ph} is the weight of the n-th element and S^{ph} the shape in phase space. This method is showcased in figure 3.1.1 b) using macro-particles across the plasma particle distribution. Now the centers of the finite phase fluid elements can be developed to retrieve relativistic equations of motions

$$\frac{\mathrm{d}\mathbf{x}_n}{\mathrm{d}t} = \frac{\mathbf{p}_n}{m\gamma}, \tag{3.1.8}$$

$$\frac{\mathrm{d}\mathbf{p}_n}{\mathrm{d}t} = \mathbf{F} + \mathbf{F}_{\mathrm{St}} \tag{3.1.9}$$

with $\mathbf{F}_{\mathrm{St}}$ the collisional force by the collisional term in the Boltzmann-Vlasov equation. This allows the use of a grid configuration to solve Maxwell equations, since the grid now only has thee dimensions.

3.1.2 Maxwell solvers

To update the electromagnetic fields for each step it is required to solve the Maxwell equations 3.1.1, 3.1.2, 3.1.3 and 3.1.4 numerically. Different Maxwell solvers were developed over the last years [45, 54, 77, 81]. While using Maxwell solvers these algorithms normally impose criteria to guarantee stability over the simulation time. They are necessary to display field structures like laser pulses in detail without of loss of information due to the grid structure. Further, the Courant-Friedrichs-Lewy (CFL) [82] condition needs to be fulfilled to ensure stability, which reads:

$$c\Delta t \leq \frac{1}{\sqrt{\Delta x^{-2} + \Delta y^{-2} + \Delta z^{-2}}} \tag{3.1.10}$$

Here $\Delta x, \Delta y$ and Δz are the grid steps in their corresponding direction and Δt the time step fields should not propagate further in a time step than a whole grid cell.

As mentioned, various Maxwell solvers are available for PIC codes, but the focus lies on two methods in this thesis. One solver is the historically first, which is the Yee solver [54], to give insight into the general approach of solving the equations numerically, and the X-dispersionless solver [77], otherwise known as Rhombi-In-plane (RIP) solver developed by A. Pukhov. Both of these solvers are capable of solving Maxwell's equations, but each one can exceed the other in different configurations. A comparison, where the RIP solver is significantly better than the Yee solver will be shown later in a study of an ultra-relativistic electron bunch propagation in vacuum.

In general, Maxwell solvers are using finite-difference time domain method, where derivatives are replaced by finite differences such as

$$\left.\frac{df(x)}{dx}\right|_{x=x_0} \approx \frac{f\left(x_0 + \frac{\delta}{2}\right) - f\left(x_0 - \frac{\delta}{2}\right)}{\delta}. \tag{3.1.11}$$

3.1.2.1 Yee algorithm

For the Yee solver, finite differences replace the derivatives in each component of the Maxwell equations 3.1.1 and 3.1.2. The other two Maxwell equations 3.1.3 and 3.1.4 are initial conditions [57]. Solving these equations leads to the update equations. For example the B_x-update equations reads

$$\frac{B^{n+\frac{1}{2}}_{x|i,j+\frac{1}{2},k+\frac{1}{2}} - B^{n-\frac{1}{2}}_{x|i,j+\frac{1}{2},k+\frac{1}{2}}}{\Delta t} = \frac{E^{n}_{y|i,j+\frac{1}{2},k+1} - E^{n}_{y|i,j+\frac{1}{2},k}}{h_z} - \frac{E^{n}_{z|i,j+1,k+\frac{1}{2}} - E^{n}_{z|i,j,k+\frac{1}{2}}}{\Delta t} \tag{3.1.12}$$

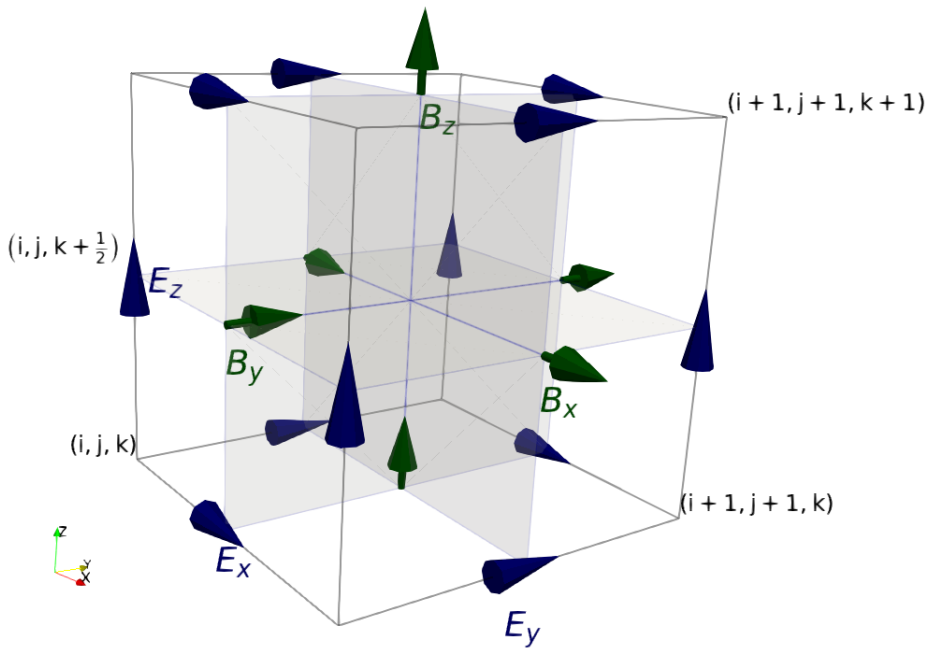

Figure 3.1.2: Grid placement of the Yee Maxwell solver. Magnetic fields are shifted by an half grid step.

with i, j and k indexing the grid index in the corresponding x, y and z direction, and n indexes the n-th time step. This equation can be rearranged for the variable $B^{n+\frac{1}{2}}_{x\|i,j+\frac{1}{2},k+\frac{1}{2}}$ so it can be used within the PIC code. The remaining update equations can be determined in the same way leading to the Yee solver.

3.1.2.2 X-dispersionless Maxwell solver

The RIP scheme, on the other hand, is a more complex Maxwell solver. The full description of this solver can be found in [77]. The key aspects of the Maxwell solver are that it is dispersionless along one dimension and that transverse fields are known on the same grid points. This benefits configurations simulating field propagation in one direction as it removes most numerical errors. To derive the RIP solver, the starting point is the Maxwell equations and electromagnetic waves propagating in X-direction. Following Maxwell equations are obtained per component

$$\frac{1}{c}\frac{\partial E_x}{\partial t} = \Gamma_x, \qquad \frac{1}{c}\frac{\partial B_x}{\partial t} = \Phi_x, \tag{3.1.13}$$

$$\frac{1}{c}\frac{\partial E_y}{\partial t} = -\frac{\partial B_z}{\partial x} + \Gamma_y, \qquad \frac{1}{c}\frac{\partial B_y}{\partial t} = \frac{\partial E_z}{\partial x} + \Phi_y, \tag{3.1.14}$$

$$\frac{1}{c}\frac{\partial E_z}{\partial t} = \frac{\partial B_y}{\partial x} + \Gamma_z, \qquad \frac{1}{c}\frac{\partial B_z}{\partial t} = -\frac{\partial E_y}{\partial x} + \Phi_z. \tag{3.1.15}$$

with $\vec{\Gamma}$ the vacuum diffraction of **E**, **J** the current and $\vec{\Phi}$ the vacuum diffraction operator of **B** reading

$$\Gamma_x = \frac{\partial B_z}{\partial y} - \frac{\partial B_y}{\partial z} - J_x, \qquad \Phi_x = -\frac{\partial E_y}{\partial z} + \frac{\partial E_z}{\partial y}, \tag{3.1.16}$$

$$\Gamma_y = \frac{\partial B_x}{\partial z} - J_y, \qquad \Phi_y = -\frac{\partial E_z}{\partial x}, \tag{3.1.17}$$

$$\Gamma_z = -\frac{\partial B_x}{\partial y} - J_z, \qquad \Phi_z = \frac{\partial E_y}{\partial x}. \tag{3.1.18}$$

Discretization of the transverse fields in a three-dimensional framework is done by a semi-implicit trapezoidal scheme. For the lattice indexing the same scheme is used as in the Yee lattice. Afterwards transport components are derived for the case $c\tau = h_x = \Delta$

$$E^{n+1}_{x|i} = \Delta\Gamma^{n+1/2}_{x|i} + E^n_{x|i}, \tag{3.1.19}$$

$$E^{n+1}_{y|i} = \frac{1}{2}\left(E^n_{y|i-1} + E^n_{y|i+1}\right) - \frac{1}{2}\left(B^n_{z|i+1} - B^n_{z|i-1}\right) + \\ + \frac{\Delta}{2}\left(\Gamma^{n+1/2}_{y|i-1/2} + \Phi^{n+1/2}_{z|i-1/2} + \Gamma^{n+1/2}_{y|i+1/2} - \Phi^{n+1/2}_{z|i+1/2}\right), \tag{3.1.20}$$

$$E^{n+1}_{z|i} = \frac{1}{2}\left(E^n_{z|i-1} + E^n_{z|i+1}\right) + \frac{1}{2}\left(B^n_{y|i+1} - B^n_{y|i-1}\right) + \\ + \frac{\Delta}{2}\left(\Gamma^{n+1/2}_{z|i-1/2} - \Phi^{n+1/2}_{y|i-1/2} + \Gamma^{n+1/2}_{z|i+1/2} + \Phi^{n+1/2}_{y|i+1/2}\right), \tag{3.1.21}$$

$$B^{n+1}_{x|i} = \Delta\Phi^{n+1/2}_{x|i} + B^n_{x|i}, \tag{3.1.22}$$

$$B^{n+1}_{y|i} = \frac{1}{2}\left(B^n_{y|i-1} + B^n_{y|i+1}\right) + \frac{1}{2}\left(E^n_{z|i+1} - E^n_{z|i-1}\right) + \\ + \frac{\Delta}{2}\left(-\Gamma^{n+1/2}_{z|i-1/2} + \Phi^{n+1/2}_{y|i-1/2} + \Gamma^{n+1/2}_{z|i+1/2} + \Phi^{n+1/2}_{y|i+1/2}\right), \tag{3.1.23}$$

$$B^{n+1}_{z|i} = \frac{1}{2}\left(B^n_{z|i-1} + B^n_{z|i+1}\right) - \frac{1}{2}\left(E^n_{y|i+1} - E^n_{y|i-1}\right) + \\ + \frac{\Delta}{2}\left(\Gamma^{n+1/2}_{y|i-1/2} + \Phi^{n+1/2}_{z|i-1/2} - \Gamma^{n+1/2}_{z|i+1/2} + \Phi^{n+1/2}_{y|i+1/2}\right). \tag{3.1.24}$$

The typical Yee grid (see figure 3.1.2) can be projected on a YZ-plane. Figure 3.1.3 displays the new planar grid where its second name stems from as it becomes a Rhombi-In-Plane. Here, it becomes apparent that the transverse fields are known on the same vertices. This is advantageous, because certain interpolations for field initialization are not necessary. Longitudinal fields like E_x and B_x are known at full integer vertices (i, j, k), where indexing is similar to the Yee solver. Transverse fields are located on points shifted by half grid step. This leads to the following exemplary diffraction and refraction equations for a full three-dimensional RIP solver

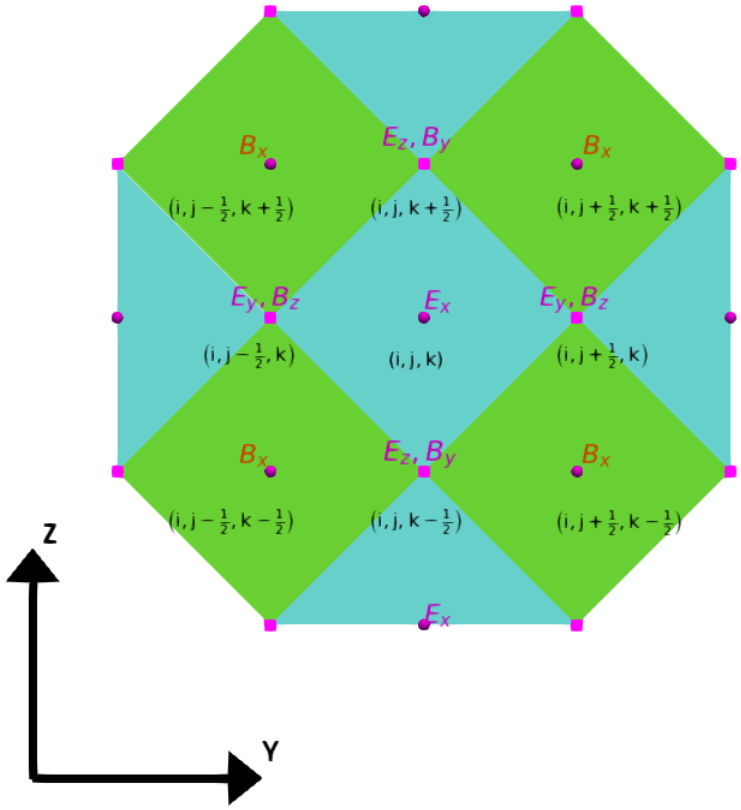

Figure 3.1.3: Rhombi-in-plane grid of the X-dispersionless Maxwell solver. One can see transverse fields are located on the same grid point.

$$\Gamma^{n+1/2}_{y|i+1/2,j+1/2,k} = \left(\frac{\partial B_x}{\partial z} - j_y\right)|^{n+1/2}_{i+1/2,j+1/2,k} = -\frac{1}{2}\left(j^{n+1/2}_{y|i,j+1/2,k} + j^{n+1/2}_{y|i+1,j+1/2,k}\right) + \\ + \frac{B^{n+1/2}_{x|i,j+1/2,k+1/2} + B^{n+1/2}_{x|i+1,j+1/2,k+1/2} - B^{n+1/2}_{x|i,j+1/2,k-1/2} - B^{n+1/2}_{x|i+1,j+1/2,k-1/2}}{2h_z}, \tag{3.1.25}$$

$$\Gamma^{n+1/2}_{z|i+1/2,j,k+1/2} = \left(-\frac{\partial B_x}{\partial y} - j_z\right)|^{n+1/2}_{i+1/2,j,k+1/2} = -\frac{1}{2}\left(j^{n+1/2}_{z|i,j,k+1/2} + j^{n+1/2}_{z|i+1,j,k+1/2}\right) - \\ - \frac{B^{n+1/2}_{x|i,j+1/2,k+1/2} + B^{n+1/2}_{x|i+1,j+1/2,k+1/2} - B^{n+1/2}_{x|i,j-1/2,k+1/2} - B^{n+1/2}_{x|i+1,j-1/2,k+1/2}}{2h_y}, \tag{3.1.26}$$

$$\Gamma^{n+1/2}_{x|i,j,k} = \left(\frac{\partial B_z}{\partial y} - \frac{\partial B_y}{\partial z} + j_x\right)|^{n+1/2}_{i,j,k} = -j^{n+1/2}_{x|i,j,k} + \\ + \frac{B^{n+1/2}_{z|i,j+1/2,k} - B^{n+1/2}_{z|i,j-1/2,k}}{h_y} - \frac{B^{n+1/2}_{y|i,j,k+1/2} - B^{n+1/2}_{y|i,j,k-1/2}}{h_z}, \tag{3.1.27}$$

$$\Phi^{n+1/2}_{y|i+1/2,j,k+1/2} = -\frac{E^{n+1/2}_{x|i,j,k+1} + E^{n+1/2}_{x|i+1,j,k+1} - E^{n+1/2}_{x|i,j,k} - E^{n+1/2}_{x|i+1,j,k}}{2h_z}, \tag{3.1.28}$$

$$\Phi^{n+1/2}_{z|i+1/2,j+1/2,k} = \frac{E^{n+1/2}_{x|i,j+1,k} + E^{n+1/2}_{x|i+1,j+1,k} - E^{n+1/2}_{x|i,j,k} - E^{n+1/2}_{x|i+1,j,k}}{2h_y}, \tag{3.1.29}$$

$$\Phi^{n+1/2}_{x|i,j+1/2,k+1/2} = -\left(\frac{\partial E_z}{\partial y} - \frac{\partial E_y}{\partial z}\right)|^{n+1/2}_{i,j+1/2,k+1/2} \\ = -\frac{E^{n+1/2}_{z|i,j+1,k+1/2} - E^{n+1/2}_{z|i,j,k+1/2}}{h_y} + \frac{E^{n+1/2}_{y|i,j+1/2,k+1} - E^{n+1/2}_{y|i,j-1/2,k+1/2}}{h_z}. \tag{3.1.30}$$

Equations for the fields are obtained in a similar way as previously, except fields and currents are shifted by a half time step [77].

Additional comparison regarding numerical Cherenkov instability in the regime of QED will be discussed in chapter 4. In order to use the RIP solver, an additional condition is imposed on grid steps and time steps of the simulation. To guarantee stability the grid step, in the direction where a dispersionless property is desired, needs to be equal to the normalized time leading to $h_x = c\Delta t$. Stability of the Maxwell solvers is also part of chapter 4.

3.1.3 Particle pusher

To update the momentum of a particle different particle pushers were developed. One which has been widely used is the Boris scheme [44, 83]

$$\frac{\mathbf{p}_1 - \mathbf{p}_0}{\Delta t} = e\left(\mathbf{E} + \frac{1}{c}\frac{\mathbf{p}_1 + \mathbf{p}_0}{2\gamma_{1/2}} \times \mathbf{B}\right). \tag{3.1.31}$$

Here momenta indexed 0 are before being updated and 1 after applying the Lorentz force. The γ-factor $\gamma_{1/2}$ is the factor at half time step Δt. $\mathbf{E}$ and $\mathbf{B}$ fields in the scheme are interpolated to the particle position. This scheme can be analytically solved for the updated momentum making it usable for the PIC method. The method used throughout

the thesis is the implicit mid-point pusher

$$\mathbf{a} = \mathbf{p}_0 + \frac{q\Delta t}{2}\mathbf{E}, \tag{3.1.32}$$

$$\mathbf{b} = \frac{q\Delta t\mathbf{B}}{2}, \tag{3.1.33}$$

$$s = \frac{1 + a^2 - b^2}{2}, \tag{3.1.34}$$

$$\gamma_1 = \sqrt{s + \left[s^2 + b^2 + (\mathbf{a}\cdot\mathbf{b})^2\right]^{1/2}}, \tag{3.1.35}$$

$$\mathbf{p}_1 = 2\frac{\gamma_1^2\mathbf{a} + \gamma_1\mathbf{a}\times\mathbf{b} + (\mathbf{a}\cdot\mathbf{b})\mathbf{b}}{\gamma_1^2 + b^2} - \mathbf{p}_0 \tag{3.1.36}$$

of which derivation can be found in [57, 77] is used. The pusher will also be extended by the dampening force imposed by the radiation reaction later on. These are by far not the only pusher for PIC codes. Various other groups developed their own particle pusher. For example the particle pusher of Li *et al.* developed in their work [84] a particle pusher that works in 9D space, using analytical solutions to advance momentum and spin. They also implement semi-classical radiation reaction as well as spin evolution described by the Bargmann-Michel-Telegdi equation. Gordon *et al.* also improves certain expressions within the 9D pusher to develop the special unitary particle pusher [85] which upgrade push rates and preserve invariance properties.

3.1.4 Basic PIC loop

With the key steps explained, a PIC code can be built. In general, a PIC code progresses a simulation through time steps, during which various algorithms are performed. These time steps are repeated until the desired number of time steps has been reached.

At first the configuration file is read, which provides information on the grid, modules, fields and particles in the simulation domain. Modules in this case describe, whether collisional ionization, QED processes, or particle merging should be called during the simulation. It can also be decided whether particles dynamics are disabled for a certain period of time to reduce numerical fields and whether observed simulation domain shifts as time progresses. Boundary conditions for particles and fields are defined in the configuration file too, as well as which algorithm is used to solve the Maxwell equations and to interpolate fields for the particle pusher.

The PIC loop can then be summarized in four basic steps, beginning after the initialization of fields and density distribution within the simulation. A basic PIC loop is outlined in figure 3.1.4.

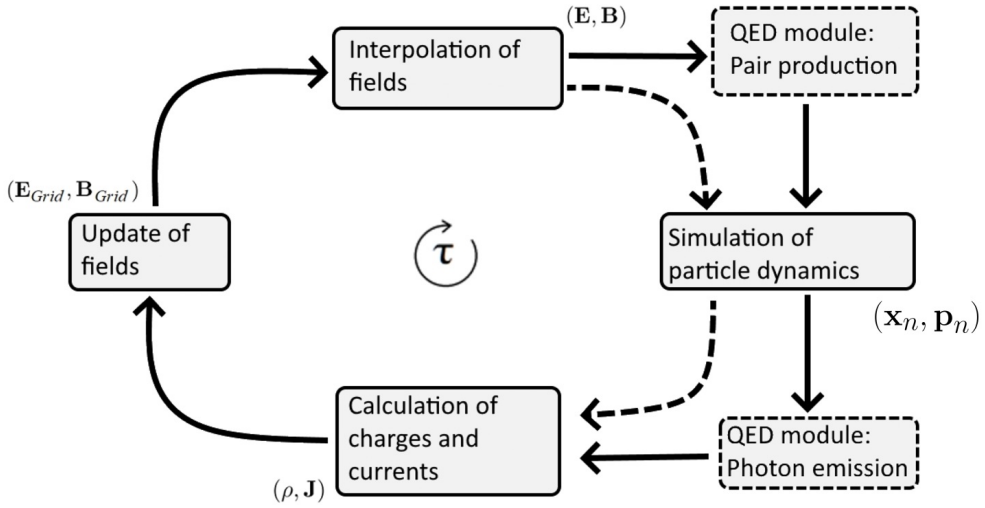

Figure 3.1.4: General scheme of a particle-in-cell time step with QED module location in VLPL. Here, the index n denotes the n-th particle and the index *Grid* describes that the fields are only known on grid vertices.

First, fields are interpolated, since the fields are stored on grid vertices, as clarified in the description of Maxwell solvers. This is necessary since the particle positions have an exact position $\mathbf{x}_n$. By interpolating the fields a more reliable particle motion can be ascertained.
Second, particles are pushed. The momentum of the particle is updated by the forces it interacts with. This can be done by the introduced particle pusher or various other ones [81, 83]. Additional forces can be added at this point.
Third, the updated particles deposit their currents on the grid after being sampled onto it. The fourth and final step is updating the fields with the new currents.

These steps conclude a PIC loop until the desired time is reached. The PIC code is reliable in displaying laser-plasma interaction if the aforementioned criteria for stability are guaranteed throughout the simulation. Additional modules can now be implemented to study new phenomena and specialize the code for certain research topics. VLPL is not the only PIC-code in use. Other PIC-codes are EPOCH [86], SMILEI [87], OSIRIS [88], WarpX [89] and many more. Further, modules are required to guarantee the functionality of the code in even higher field strengths, which are described in the following sections.

3.2 Poisson solver

In order to simulate an ultra-relativistic electron bunch in vacuum in chapter 4 the fields of the bunch need to be initialized before the simulation begins. A method of initializing these fields is the use of a Poisson solver.
The algorithm description and equations of this chapter are reused, adapted and extended from the *Suppression of errors in simulated ultra-relativistic bunch propagation using the X-dispersionless Maxwell solver*, by Filipovic, M., Baumann, C. and Pukhov, A. (2022). Physical Review Accelerators and Beams, 25(5), 054405, licensed under CC BY 4.0 (https://creativecommons.org/licenses/by/4.0/). The algorithm was developed by A. Pukhov and M.F. wrote the manuscript.

The Poisson-solver considers the implemented charge distribution $\rho(\mathbf{r})$ and assumes it propagates with the velocity $\mathbf{v}$. $\mathbf{v}$ is assumed to be close to the speed of light. Considering a cross-section where the charge distribution passes through, the section can be described as

$$\mathbf{j} = qc\rho. \tag{3.2.1}$$

Using the current density, one can calculate the magnetic field $\mathbf{B}$,

$$\nabla \times \mathbf{B} = \mathbf{j} \tag{3.2.2}$$

as well as

$$\mathbf{B} = \vec{\nabla} \times \mathbf{A} \tag{3.2.3}$$

with $\mathbf{A}$ being the magnetic vector potential. In the next step, a Fast-Fourier Transformation is applied on the charge density, resulting in

$$-\vec{\nabla}_{\perp}^2 \mathbf{A} = \mathbf{J} \tag{3.2.4}$$

The vector potential can be calculated by the Fourier image of the real current $\hat{\mathbf{J}} = \mathrm{FFT}[\mathbf{J}]$. One gets

$$\mathbf{A} = \frac{i}{k^2}\hat{\mathbf{J}} \tag{3.2.5}$$

for the vector potential. The Fourier image of the magnetic field is then

$$\hat{\mathbf{B}}_F = i\mathbf{k} \times \mathbf{A} \tag{3.2.6}$$

Finally, using an inverse Fast-Fourier transformation retrieves the magnetic field in the cell.

It is important to note that the exact implementation of the Poisson solver may vary in the PIC code depending on the Maxwell solver used. The reason lies within the structure of the grid. In the case of the Yee solver the electric and magnetic fields are shifted by a half step due to the structure of the update equation as displayed in figure 3.1.2. Due to the complexity of the grid the algorithm is only adapted for simulations using a single processing core. It has been considered that implementing it in a parallel computing environment would be unnecessary as newer and improved Maxwell solver exists. Previously, electromagnetic fields generated by moving charges were manually implemented by determining the electric and magnetic fields and entering them at simulation begin using a configuration file.
As for the RIP solver, the transverse field components are known on the same vertices of the grid (compare figure 3.1.3). This simplifies the interpolation process and the Poisson solver is modified to function on a single core as well as utilizing parallel computing.

3.3 Radiation reaction in particle-in-cell codes

After building a general PIC code, additional physical behaviours for particles can be added. So far, only the influence of the Lorentz force on particle motion has been implemented. Beyond that, once intensities increase charged particles emit high-frequency radiation. To include radiation reaction under the locally constant field approximation with the code an additional force on the momentum is required as a dampening force. The Lorentz-Abraham-Dirac (LAD) equation [34] is a first general description of the radiation reaction. But due to unpredictability such as pre-acceleration and runaway-solutions, it is not a perfect description. `VLPL` applies a damping force by determining the total emitted power, which is given by the relativistic Larmor formula [35],

$$P_{\mathrm{rad}} = \frac{2}{3}\,\alpha\,\frac{m^2c^4}{\hbar}\,\chi^2. \tag{3.3.1}$$

This leads to a radiation reaction force of

$$\mathbf{F}_{\mathrm{RR}} = -\frac{2}{3}\,\alpha\,\frac{mc^2}{\hbar}\,\chi^2\,G(\chi)\,\frac{\mathbf{p}}{\gamma} \equiv -\nu_{\mathrm{RR}}\,\mathbf{p} \tag{3.3.2}$$

with ν_{RR} the characteristic radiation loss frequency. Additionally, the gaunt factor $G(\chi)$ mitigates errors once the quantum non-linearity parameter approaches unity and QED effects may become important [90, 91]. The Gaunt factor is

$$G(\chi) = -\int_0^\infty \frac{12 + 5\chi s^{3/2} + 12\chi^2 s^3}{\left(1+\chi s^{3/2}\right)^4}\,\mathrm{Ai}'(s)\,s\,\mathrm{d}s. \tag{3.3.3}$$

One can see it includes an integral leading to a high computational effort if calculated within the PIC code. VLPL uses an approximation to speed up calculation of the factor reading

$$G(\chi) \approx \left(1 + 18\chi + 69\chi^2 + 73\chi^3 + 5.806\chi^4\right)^{-1/3}. \tag{3.3.4}$$

The quantum non-linearity parameter is calculated by averaging its value before and after the particle push.

In a final step, the radiation reaction force is applied to the momentum of the particle. In the case of VLPL, the dampening force is directly applied after the particle push algorithm by using

$$\mathbf{p}_{\mathrm{RR}} = \frac{\mathbf{p}_1}{(1 + \nu_{\mathrm{RR}}\tau)}, \tag{3.3.5}$$

with $\mathbf{p}_1$ being the momentum after the particle push.

One has to note, that once the criteria $\chi > 1$ is met, the classical description of these radiation losses is not valid. The code needs to use a different approach for this physical phenomenon, since the classical approach describes the losses as continuous. If the quantum non-linearity parameter exceeds unity greatly, the classical description will result in photon emission with energies greater than the emitting particle and violate conservation of energy. Therefore, the following section will discuss the implementation of a QED module in the regime of $\chi \gg 1$.

3.4 QED events in particle-in-cell codes

Moving onto even stronger fields, where particles interact with stronger forces, new physical phenomena are assumed and discovered. These effects have to be implemented as well in the PIC code. The effects that become visible are the QED processes such as the nonlinear Compton scattering and Breit-Wheeler pair production. QED processes were previously mentioned in the theory section of this thesis, but an adequate algorithm is required for their thoughtful implementation in PIC codes. Various groups have developed successful QED-PIC codes with the underlying principle of incorporating the stochastic nature of it using a Monte-Carlo algorithm. As one of the key aspect of this thesis, a QED module has been implemented in the current VLPL version and corresponds the alternative event generator from the publication by Elkina *et al.* [72].

The implementation of the QED module in VLPL has been split into two blocks. One block simulates the high-energy photon emission, otherwise known as the nonlinear Compton scattering process. The second block is the pair production for the Breit-Wheeler process.

Starting with the photon emission algorithm, the PIC code iterates through each macro-particle. Every particle that is able to emit high energy photons enters the routine. First, the module generates a uniformly distributed random number $r_1 \in [0,1]$. r_1 is used to guess a possible photon energy

$$\varepsilon_\gamma = r_1 \varepsilon_e, \tag{3.4.1}$$

as a fraction of the initial particle energy ε_e with $\varepsilon_e = (\gamma_e - 1) m_e c^2$ being the emitted particle's energy. r_1 also leads to the momentum of the photon that might be emitted:

$$\mathbf{p}_\gamma = r_1 \mathbf{p}_e \tag{3.4.2}$$

Here, $\mathbf{p}_e$ is the momentum of the emitting particle. The direction of the emitting photon will be assumed to be in the same direction as the emitting particle. Afterwards, the quantum non-linearity parameter is calculated for both the emitting particle (χ_e) and the possible photon (χ_γ). The code uses the interpolated fields on the particle position. With these information one can calculate the energy distribution per unit time of an emitting particle $\mathrm{d}W_{\mathrm{rad}}/\mathrm{d}\varepsilon_\gamma$. For the Airy-integral within this expression, a pre-calculated table of values is loaded at runtime. This table contains 10^5 entries for various lower limits of the integral. Solving such an integral numerically is time consuming and has been avoided by this method. The probability that this generated photon is emitted in the current time step of the simulation Δt is defined as

$$W_{\mathrm{rad}} = \frac{dW_{\mathrm{rad}}(\varepsilon_\gamma)}{d\varepsilon_\gamma} \varepsilon_e \Delta t. \tag{3.4.3}$$

To determine whether the particle is emitted, a second uniformly distributed random number $r_2 \in [0,1]$ is generated and compared to the probability 3.4.3. If $r_2 < W_{\mathrm{rad}}$ is fulfilled, the event occurs. This means a photon with ε_γ and $\mathbf{p}_\gamma$ will be emitted. In the PIC code, a new photon macro-particle is implemented with the energy and momentum used in the algorithm at the position of the emitting particle. The emitting particle gets its properties adjusted and modified by the conservation of momentum reading

$$\mathbf{p}_{e,\mathrm{new}} = \mathbf{p}_e - \mathbf{p}_\gamma. \tag{3.4.4}$$

The criteria which the module needs to uphold is

$$\Delta t \ll \left[\frac{dW_{\mathrm{rad}}(\varepsilon_\gamma)}{d\varepsilon_\gamma} \varepsilon_e \right]^{-1}. \tag{3.4.5}$$

If the condition is not fulfilled the process cannot be resolved in the time step of the simulation.

The process for converting a high-energy γ-photon into an electron-positron pair is similarly structured as the photon emission block. Every γ-photon will be subject to this algorithm. The algorithm produces a random number that is uniformly distributed $r_1' \in [0.1]$ and uses its value to declare an electron momentum

$$\mathbf{p}_{e^-} = r_1' \mathbf{p}_\gamma. \tag{3.4.6}$$

Again, the quantum non-linearity parameters for the converting photon and the electron of the pair are calculated and used to derive the probability for the process of pair production by a decaying photon

$$W_{\text{pair}} = \frac{dW_{\text{pair}}(\varepsilon_{e^-})}{d\varepsilon_{e^-}} \varepsilon_\gamma \Delta t. \tag{3.4.7}$$

The pair production process occurs if a second generated uniformly distributed random number $r_2' \in [0,1]$ satisfies $r_2' > W_{\text{pair}}$. Should the condition be met, the macro-particle representing the photon is deleted from the simulation, and macro-particles for both an electron and positron are added. The weight of the new macro-particles is equal to the deleted photon macro-particle. The remaining positron momentum can be determined by following the conservation of momentum

$$\mathbf{p}_{e^+} = \mathbf{p}_{e^-} - \mathbf{p}_\gamma. \tag{3.4.8}$$

These two blocks conclude the QED module of the PIC code and are found in `VLPL`.

These concludes the theoretical background and numerical tools for the QED processes. In the following the code `VLPL` will be extended with a merger module mitigating the increase of computational load by the production of vast secondary particles by QED processes.

3.5 Merging algorithms

PIC codes can also benefit from extending their functionality without implementing new physical phenomena. Certain configurations may create drawbacks, such as QED experiments [72, 92–94] and ionization processes [95, 96]. In these cases, an abundance of new particles is introduced to the simulation, leading to more calculation operations that increase compute time. Subsequently, the increased number of particles may lead to load imbalance if the code is run with multiple nodes working on different domains of the

simulation. Various research groups have attempted to tackle this issue by introducing algorithms that merge particles with similar properties into a new more massive macro particle [97, 98]. It is important, that after the merge algorithm is performed, physical phenomena are still coherent with particles which have not undergone the merge algorithm.
The simple merging algorithm, currently implemented in VLPL, attempts to overcome the problem of great numbers of macro-particles. But the simple merging algorithm had significant drawbacks in configurations where the scattering and various particle trajectories were present. These drawbacks lead to not upholding the conservation of momentum and energy and inaccurate particle behaviour. An explanation of the algorithm and its drawbacks will be given in the subsequent subsections.

To facilitate a comprehensive discussion about merging algorithms, it is important to establish a framework where the algorithms and functions can be called. The module allows different settings. Settings include the choice of merger algorithm, a threshold of minimum particles per cell to start a merging attempt, and the time period to determine how much time should pass until the next merge attempt. Additional settings become available once an algorithm is chosen in order to fine-tune the merge process.

This section tackles the implementation of merger algorithms within VLPL. The code was extended by two new merger algorithms and compared to the current algorithm to be available for future simulations. First, the simple merging algorithm and its problems will be explained. Secondly, a brief summary of the new mergers will be given. The algorithms discussed are the Two-particle merger by Vranic *et al.* [99] and the Voronoi merger by Luu *et al*. [100]. But of course there exist many more algorithms [101–103]. Finally, the mergers will be compared in different simulations to see, whether physical properties are retained and how efficient the merger rate is.

3.5.1 Simple merging algorithm

As the first implemented particle merger in VLPL, a simple summation of particles was considered.
Before merging, the algorithm retrieved the maximum allowed number of particles per cell from the configuration file. If the number of particles exceeds this value the merger starts the actual merging process. Here, the list of all particles within the cell is retrieved. This list is then sorted in ascending order according to particle weight. Afterwards, the merging algorithm picks the first two particles of the sorted list, which are now the lightest particles, and compares their weights. The heavier particle will become the

particle where the other particle will be merged into. Merging two particles will be done by averaging particle position and particle momentum. Once the averaged position and momentum is given to the heavier particle the weight of the lighter one is added to it. Finally, the lighter particle is deleted from the simulation and the list gets adapted. The algorithm continues until the initially given particle limit per cell is reached.

This method of particle merging guarantees a reduction of particle at all times despite huge variances in their physical properties. The algorithm is also fast since it uses built-in functions by C++, simple averaging to merge particles, and requires no temporary storage of data.

But the simplicity is also one of its biggest disadvantages, since already mentioned similarity in physical properties are not considered. This can be fatal if particle bunches are set up in a collision and the number of particles abruptly rises within cells. Particles get merged into a single particle and momentum and energy might not be conserved, which will be shown later. Super massive particles will dominate the simulation and eliminate the physical properties of particles initially not merged. Certain scenarios like QED processes can be disastrous with those particles, since they are the biggest source of secondary particle. These problems will be later seen in the benchmarks provided in the upcoming sections. Therefore, extending the PIC code with improved mergers is essential

3.5.2 Two-particle merger

One of the merger algorithms added over the course of the work on this thesis in the tool set of `VLPL` is the merging algorithm by Vranic *et al.* [99]. Figure 3.5.1 demonstrates the general scheme of the merging algorithm. After initializing the module, each spatial merge cell exceeding the previously set minimum particle per cell number is subjected to the merge algorithm. First, the minimum and maximum of each spatial cell in each direction is determined. Figure 3.5.1 (a) shows a random distribution of particles in a local grid cell, where 15 particles of the same species are located. In the next step, the spatial cell is divided into sub-groups in momentum space, which can be considered as momentum cells (compare figure 3.5.1 (b) arrows indicate the momentum vector of the particle.). The number of momentum cells can be determined by the merge module. At this point, information of the momentum cells are retrieved. This includes the minimum and maximum momentum per component and the range between those values. Each particle is now grouped in the corresponding merge cell. It can be assumed, that particles

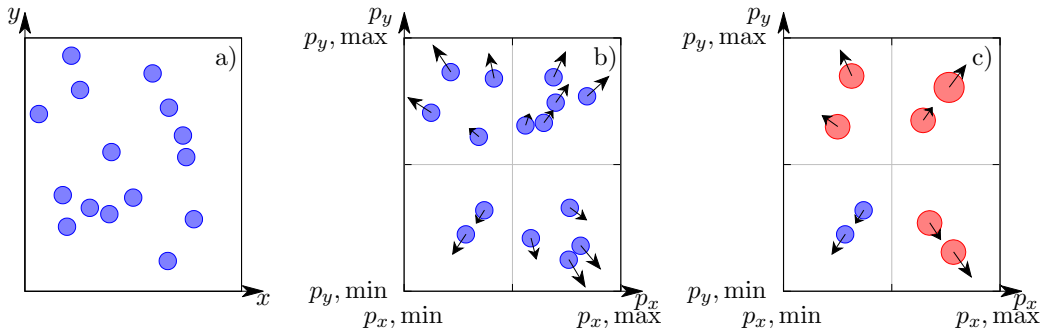

Figure 3.5.1: General scheme of two particle merger [99]. a) shows the local space of a grid cell, b) particles are grouped in momentum cells, c) macro-particles in a momentum cell are merged into two new macro-particles. Newly merged particles are red and have a bigger radius due to their higher weight.

of the same species in each momentum cell exhibit similar properties as they are closely grouped spatially and similar in momentum.

After the grouping, general data of the momentum cell are retrieved. The algorithm calculates the total weight w_{tot}, momentum of the cell $\mathbf{p}_{\text{tot}}$, and energy of the cell ε_{tot} by

$$w_{\text{tot}} = \sum_{i=1}^{N} w_i, \tag{3.5.1}$$

$$\mathbf{p}_{\text{tot}} = \sum_{i=1}^{N} w_i \mathbf{p}_i, \tag{3.5.2}$$

$$\varepsilon_{\text{tot}} = \sum_{i=1}^{N} w_i \varepsilon_i \tag{3.5.3}$$

with N the number of particles of a species, w_i the weight, $\mathbf{p}_i$ the momentum and ε_i the energy of the i-th particle in the momentum cell respectively. The particles of a momentum cell can be merged if the cell has more than two particles in it. Having less than three particles in a momentum cell indicates that the momentum cell is finished with the merging. The reason for merging into two particles is is the conservation of energy and momentum simultaneously. An example given by Vranic *et al.* in their work [99] involves the merge process between two particles with opposite momenta. Calculating the total statistics of the cell would lead to a total momentum of $\mathbf{p}_{\text{tot}} = \vec{0}$, $w_{\text{tot}} = 2w$ and $\varepsilon_{\text{tot}} = 2w\varepsilon$. Appointing the total statistics to the newly merged particle would lead to an invalid energy to momentum connection, as a zero value for a momentum cannot lead to a non-zero energy. But in the case of merging into two new particles these quantities can

be conserved with

$$w_{\text{tot}} = w_1 + w_2, \tag{3.5.4}$$

$$\mathbf{p}_{\text{tot}} = w_1\mathbf{p}_1 + w_2\mathbf{p}_2, \tag{3.5.5}$$

$$\varepsilon_{\text{tot}} = w_1\varepsilon_1 + w_2\varepsilon_2 \tag{3.5.6}$$

with index 1 and 2 indicating the new particles the algorithm merges into. Additionally, one needs to distinguish between photons and electrons due to their mass. The two new particles will have the same weight and the momentum can be constructed with

$$\mathbf{d} = (\pm\Delta p_x, \pm\Delta p_y, \pm\Delta p_z), \tag{3.5.7}$$

$$\cos(\omega) = p_{\text{tot}}/(w_{\text{tot}}p_1), \tag{3.5.8}$$

$$\mathbf{e}_1 = \mathbf{p}_{\text{tot}}/p_{\text{tot}}, \tag{3.5.9}$$

$$\mathbf{e}_2 = \mathbf{e}_1 \times \mathbf{e}_3, \tag{3.5.10}$$

$$\mathbf{e}_3 = \frac{\mathbf{d} \times \mathbf{e}_1}{d} \tag{3.5.11}$$

with $p_1 = \varepsilon_1$ for photons and $p_1 = \sqrt{\varepsilon_1^2 - 1}$ for electrons. With these equations the new particle momenta are

$$\mathbf{p}_1 = p_1(\cos(\omega)\mathbf{e}_1 + \sin(\omega)\mathbf{e}_2), \tag{3.5.12}$$

$$\mathbf{p}_2 = p_1(\cos(\omega)\mathbf{e}_1 - \sin(\omega)\mathbf{e}_2). \tag{3.5.13}$$

Figure 3.5.2 illustrates the different momenta, their connection with each other and the construction of the two new particle momenta.
The new particles are now placed in the simulation domain (see figure 3.5.1 subplot c)). Choosing a location for the new particles can involve either taking an arbitrary particle position of the to be merged particles or by averaging the particle position between those particles. After placing the new particles the old particles are deleted. A special case can be constructed if all particles are propagating in the same direction. If this is the case, the particle merging algorithm merges the particles into one particle as the total momentum of the cell $\mathbf{p}_{\text{tot}}$ is parallel to the direction vector $\mathbf{d}$ leading to the support vector $|\mathbf{e}_3| = 0$.

Settings that can be adjusted for this algorithm are the dimension of the momentum cell as well as the number of partitions of the momentum cell in each direction. Additionally, the momentum cells can be divided into more packets if the particle number is significantly greater than two per momentum cell, to avoid drastically reducing the number of particles in the simulation.
An improvement on the algorithm can be considered if the momentum of particles varies over several magnitudes. In this case the binning of the momentum cells can be changed from a linear approach to a logarithmic one. Enabling such a feature should only be considered on a case by case situation.

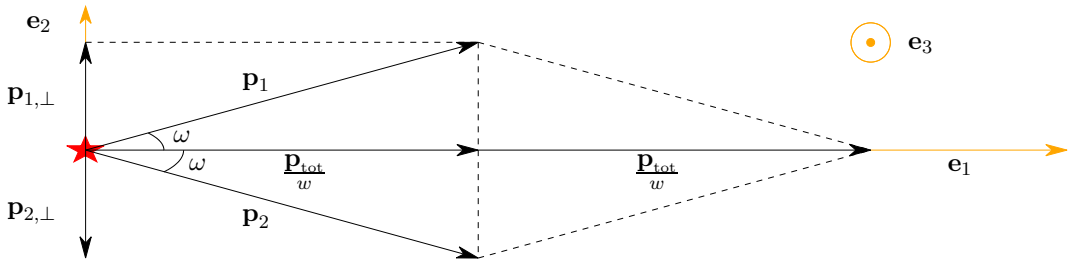

Figure 3.5.2: Plane of the new particles momentum. Based on [99]. The red star is the summation of information of a single momentum cell. The frame of the merging process is given by $(\mathbf{e}_1, \mathbf{e}_2, \mathbf{e}_3)$.

3.5.3 Voronoi centroid merger

Having thoroughly examined the first merger algorithm to be included in `VLPL`, a second algorithm is now introduced. The Voronoi particle merging algorithm by Luu *et al.* in their work [100] is described next. There an extensive description can be found. The merge algorithm shows similarities to the two-particle merger algorithm by Vranic and can incorporate merging into two particles. The major difference lies in dividing the particles to be merged in reasonable groups. As the name implies, the grouping uses the Voronoi diagram [104]. Figure 3.5.3 shows an example cell with particles of the same particle species. On the right hand side, the cell is divided by the Chebyshev partitioning into a Voronoi diagram. The Chebyshev distance is described as

$$\text{dist}\,(\mathbf{p},\mathbf{q}) = \max|q_i - p_i| \tag{3.5.14}$$

with $\mathbf{p}$ and $\mathbf{q}$ two vectors of an arbitrary quantity [100].

The algorithm works as follows. Before beginning a merge attempt, two parameters need to be set by the user. These parameters are the tolerances for position T_r and momentum T_p. Beginning with the initial cell, the algorithm declares this cell as the first Voronoi cell with all particles. Similar to the two-particle merger by Vranic and their group, the total weight W_0 is calculated, as well as the average position $\mathbf{R}_0$ and momentum $\mathbf{P}_0$. These averages together create the centroid of the Voronoi cell, described by capital letters. Next, the standard deviation in each dimension j of the phase space is calculated

$$\sigma_{\mathbf{R}_0,j} = \sqrt{W_0^{-1}\sum_i w_i \left(x_{i,j} - \mathbf{R}_{0,j}\right)^2}, \tag{3.5.15}$$

$$\sigma_{\mathbf{P}_0,j} = \sqrt{W_0^{-1}\sum_i w_i \left(p_{i,j} - \mathbf{P}_{0,j}\right)^2}. \tag{3.5.16}$$

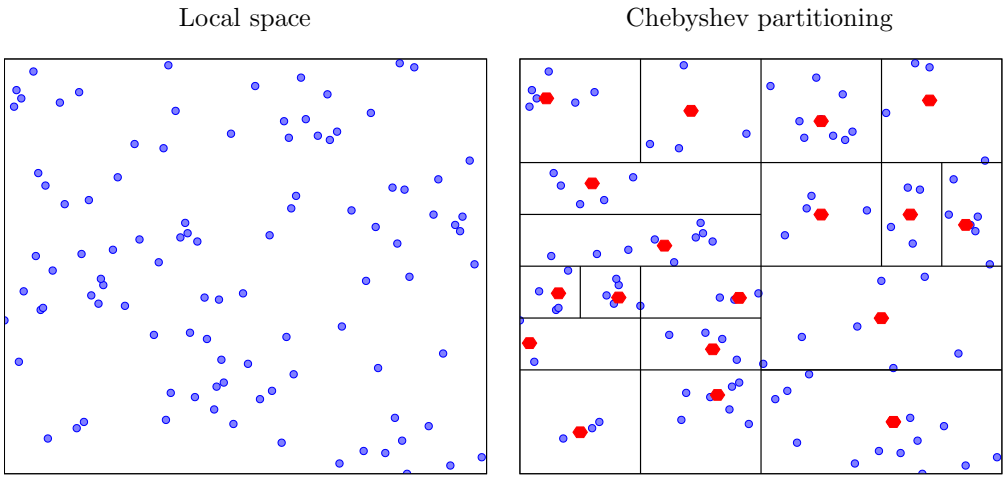

Figure 3.5.3: Chebyshev measure used for Voronoi diagram. Enclosed areas are Voronoi cells with red hexagons indicating Voronoi centroid of the cell cell.

Afterward, the so-called coefficient of variation Δ is determined for each direction by

$$\Delta_{\mathbf{R}_{0,j}} = \frac{\sigma_{\mathbf{R}_{0,j}}}{L_{\mathbf{R}_{0,j}}}, \tag{3.5.17}$$

$$\Delta_{\mathbf{P}_{0,j}} = \frac{\sigma_{\mathbf{P}_{0,j}}}{\mathbf{P}_{0,j}} \tag{3.5.18}$$

with $L_{\mathbf{R}_0}$ the lengths of the first Voronoi cell. Now a condition is imposed on the Voronoi cell. If the coefficient of variations is bigger than the tolerances in any of the six dimensions of the phase space, the Voronoi cell is subject to be divided into smaller Voronoi cells. Division of the cell is along the dimension where the coefficient of variation has the largest deviation. As the Voronoi cell is divided the particles within the cells are redistributed between the two new cells. From this point on the algorithm repeats from the point where its statistics W, R and $\mathbf{P}$ are calculated. Further division continues until every new Voronoi cell succeeds in the condition of coefficient of variations being smaller than the chosen tolerances. At this point the values of the centroids are chosen as merged particles and the old particles are deleted. It can be noted that after the particles are distributed into meaningful Voronoi cells, instead of using the centroids as new particles, the two-particle merge algorithm can be used.

This concludes the description of the two algorithms and their implementation into the current version of `VLPL`. The following section discusses the algorithms in benchmarks for reliability and rate of success.

3.5.4 Comparison

To benchmark the merger algorithms in VLPL two commonly used tests are performed for each algorithm and compared against simulations without applying a merger module. The first test uses two plasma blocks propagating towards each other. Here, the number of particles will be reduced as the two blocks overlap. In a second test a magnetic shower will be simulated, where the simulation domain, full of energetic charged particles, is under the influence of a constant magnetic field. Secondary particles are emitted by the charged particles and the emitted photons decay into electron-positron pairs.

3.5.5 Overlapping plasma blocks

As mentioned earlier, the general merge capabilities are tested with propagating plasma blocks that overlap. Therefore, two plasma blocks of electrons are initialized in the framework of two-dimensional PIC simulations. The normalization of all lengths in this case is $l_0 = 0.8\mu\text{m}$. Each block has a length and height of $2l_0$. The initial momentum of each particle in one block is $+150m_e c$, and in the other block, it is $-150m_e c$. The grid parameters are $0.1l_0$ as step width in both the x- and y-directions. The time step chosen is $\Delta t = 0.005l_0/c$. Each cell is initiated with 15 particles, and the merge module triggers as soon as more than 15 particles are located within a cell. The density of each cell is $100n_{\text{cr}}$, with $n_{\text{cr}} \approx 1.74 \times 10^{21}\text{cm}^{-3}$, the critical density for l_0. To avoid observing additional physics, the interaction of the fields with particles has been disabled. The additional parameters for the Voronoi particle merging algorithm are tolerances $T_r = 0.4$ and $T_p = 0.015$. A merge attempt is performed every time step.

In this simulation, the plasma blocks only propagate through each other and end up on the opposite side. This test allows one to determine whether the phase-space is preserved with this method. Therefore, the density distribution of the plasma block is captured as well as the momentum distribution. Figure 3.5.4 displays the density distribution at the end of the simulation. The simple merger clearly fails to retain the block shapes and densities. Looking at the particle merging algorithm of Luu and Vranic, the shapes of the plasma blocks retain their initial dimensions. Examining the density distribution for Vranic shows a compression at the front of the plasma blocks, where the density increases to $126.64n_{\text{cr}}$. These are the areas, where the plasma blocks first experienced the overlap. Certain cells undergo multiple merge attempts and merged multiple macro-particles, while removing them in a different column. In the case of the Voronoi merger merging attempt with the plasma blocks, the density distribution remains unchanged compared to the data obtained without a merger.

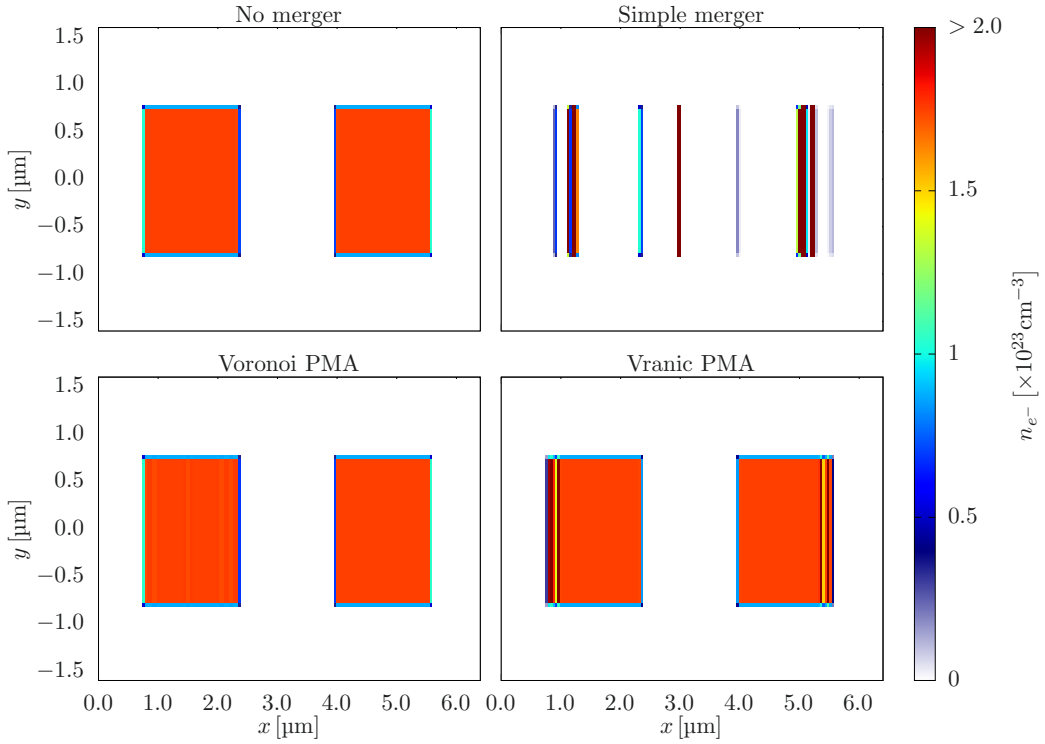

Figure 3.5.4: Density distribution at the end of the simulation for different particle merging algorithms. Simulation of temporally overlapping plasma blocks.

For the momentum distribution (see figure 3.5.5), all simulations, except for the simple merger, demonstrate similar results by maintaining the same numbers of particles at $\pm 150 m_e c$. Both newly implemented mergers effectively preserve the momentum distribution. As for the number of particles in figure 3.5.6, the simulation holds 46800 particles, at the end of the simulation Vranic particle merging algorithm reduces the number of particles to 17316, whereas Voronoi particle merging algorithm merges them to a total number of 15093 macro-particles. Both new particle merging algorithms continue merge operations until the blocks stop overlapping.

In an attempt to minimize the compression of the plasma blocks, the time between merge attempts is increased and merges are only attempted at the point of complete overlap. Therefore, the merge period, which defines the time between merging attempts, is set at $400\Delta t$. In the case of Vranic merger, the number of particles is still significantly reduced to 18720 particles, while the Voronoi algorithm reduces them to 15600 particles. The density distribution is now better retained for the Vranic merger, as seen in figure 3.5.7. It is important to ensure that the merging frequency is not smaller than the characteristic time scale of the system. Otherwise, there is no guarantee that all relevant physics are

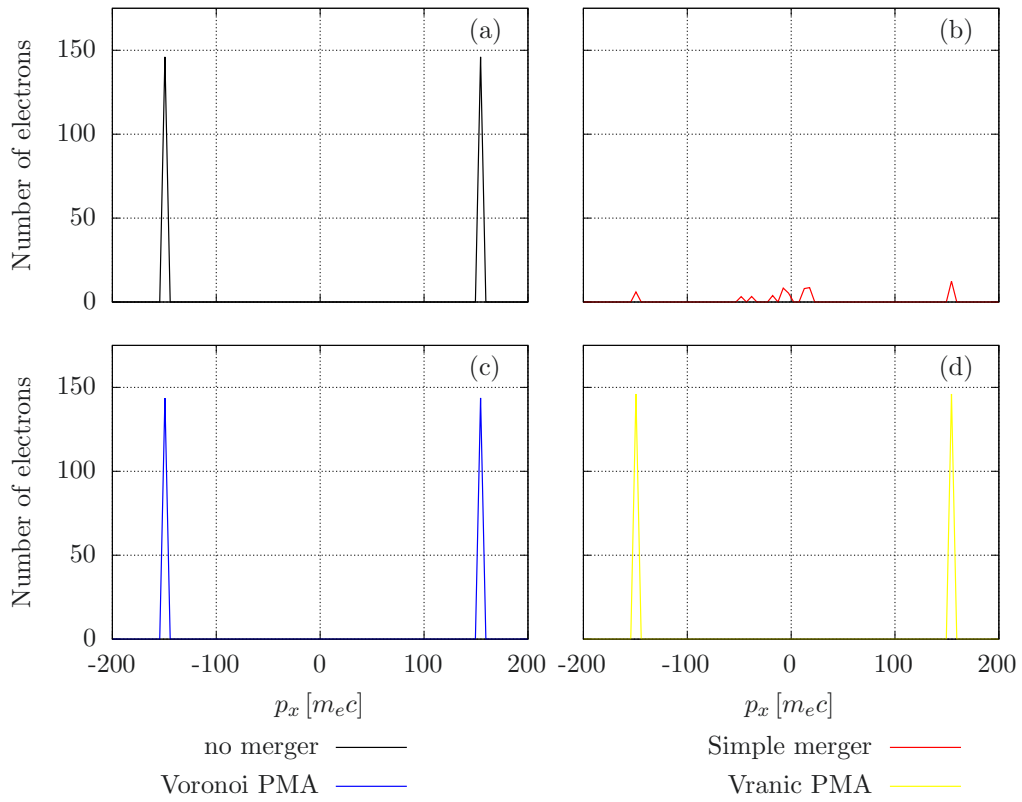

Figure 3.5.5: Phase space distribution at the end of the simulation for different particle merging algorithms. Simulation of temporally overlapping plasma blocks.

accurately modeled [99]. Vranic *et al.* suggests merging after every five time steps in general.

3.5.6 Magnetic shower

The second test employs the QED module to enable QED effects within the simulation. The test uses initial electrons with non-zero momentum and a strong external magnetic field to trigger a QED cascade due to multiple photon emissions and pair production processes. Electrons are assigned a momentum of $p_x = 3000 m_e c$ in an external magnetic field of $B_z = 2800(2\pi m_e c^2)/l_0 = 7.47 \times 10^{10}$G. The simulation is performed in a two-dimensional PIC framework. The spatial grid width is $0.04 l_0$ in all directions and a time step of $\Delta t = 0.005 l_0/c$ is chosen, with $l_0 = 4 \times 10^{-4}$cm the normalization of all lengths. Each cell has five particles per cell and the merge algorithm is triggered if at least 10

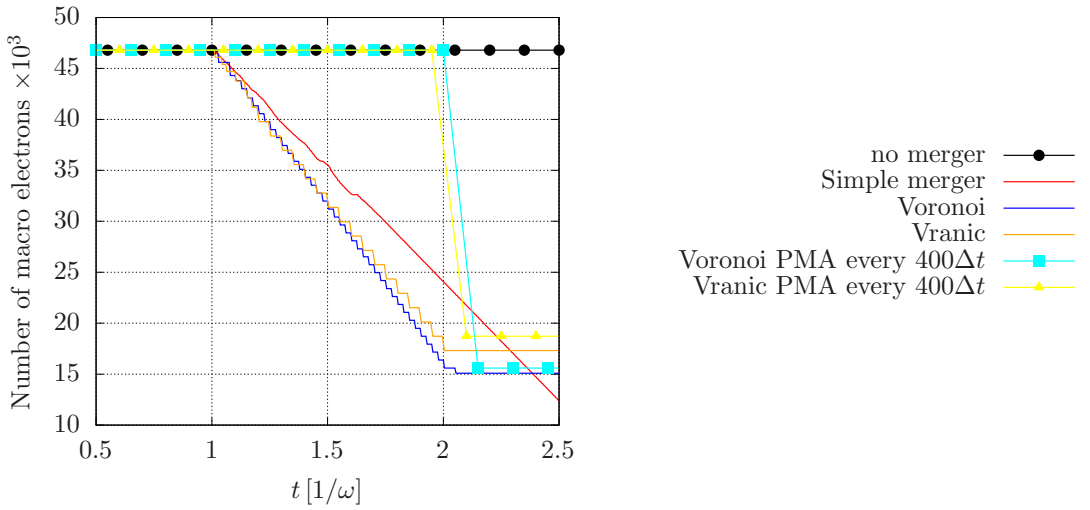

Figure 3.5.6: Number of macro-particle in the electron particle specie over time for different particle merging algorithms. Simulation of temporally overlapping plasma blocks.

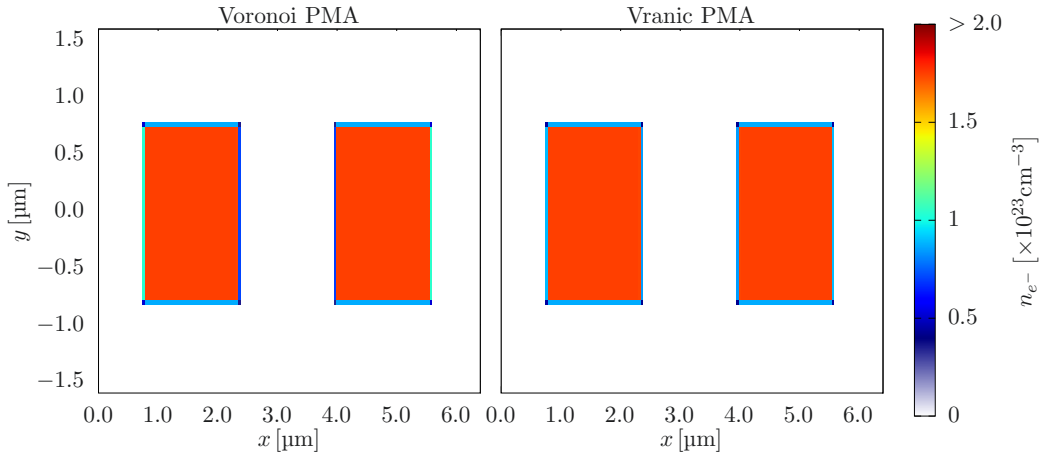

Figure 3.5.7: Density distribution at the end of the simulation for different particle merging algorithms. Merge period set at $400\Delta t$. Simulation of temporally overlapping plasma blocks.

particles are in a cell. Voronoi particle merging algorithm uses the tolerances $T_r = 1.0$ and $T_p = 0.2$. Merge period in this simulation is $50\Delta t$.

In this test, the initial electrons emit photons by interacting with a strong external magnetic field. These photons in fact can decay into electron-positron pairs, giving the simulation an abundance of secondary particles. This is a useful test as it challenges the merging algorithms with a dynamic number of particles while trying to retain physical properties like energy spectra. These quantities can once again be compared with an

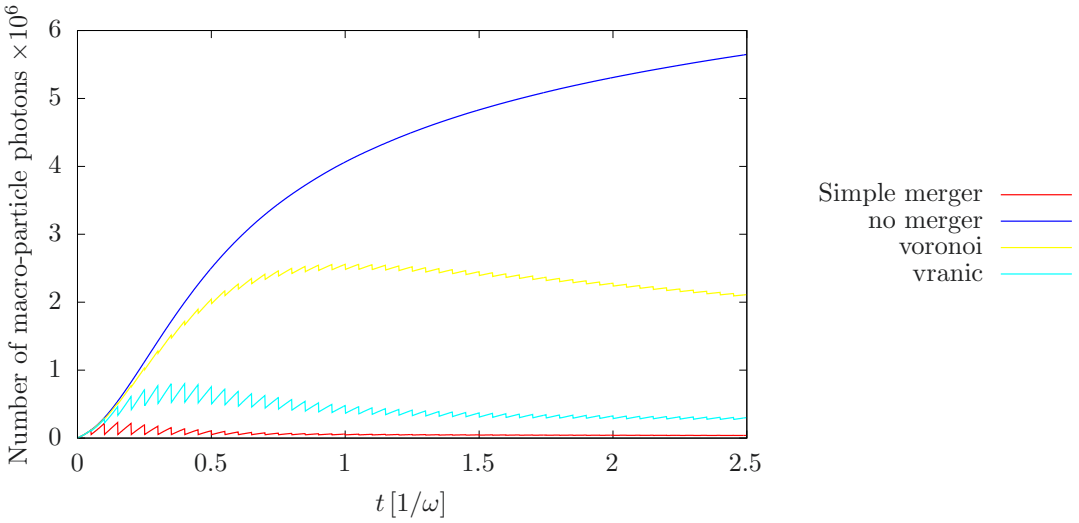

Figure 3.5.8: Number of macro-particle in the photon particle specie over time for different particle merging algorithms. Simulation of a magnetic shower.

initial simulation conducted without using a merger. Energy spectra are particularly useful as they allow an observation of what kind of particles are merged and the energy they obtain. This information could be helpful in identifying which particles are prone to merging.

Figure 3.5.8 shows the time evolution of photon macro-particles. Photons were chosen because they are the majority of secondary particles produced, and low-energy photons are unable to decay into an electron-positron pair. Both particle merging algorithms cap the number of macro-particles within the domain. Energy is correctly conserved, as can be seen in figure 3.5.9. Only the simple merger fails to conserve the energy in the system. Finally, energy spectra are obtained at the end of the simulation and summarized in figure 3.5.10. The Voronoi particle merging algorithm is in great agreement for the photons. Slight differences are only visible in the low energy part of the spectrum. The reason for that is the momentum tolerance T_p for this simulation. Greater differences are visible in the simulation using the Vranic particle merging algorithm. Here, it appears that a broader range of low-energy photons have been merged by the algorithm, leading to a peak in the spectra at $\sim$ 3MeV. For energies above 30MeV, both particle mergers are in good agreement with the reference simulation that did not use a merger. Particle spectra for electrons and positrons are nearly identical. Differences are only visible in the low-energy region, where the noise in the spectrum appears to have been merged into higher energies.

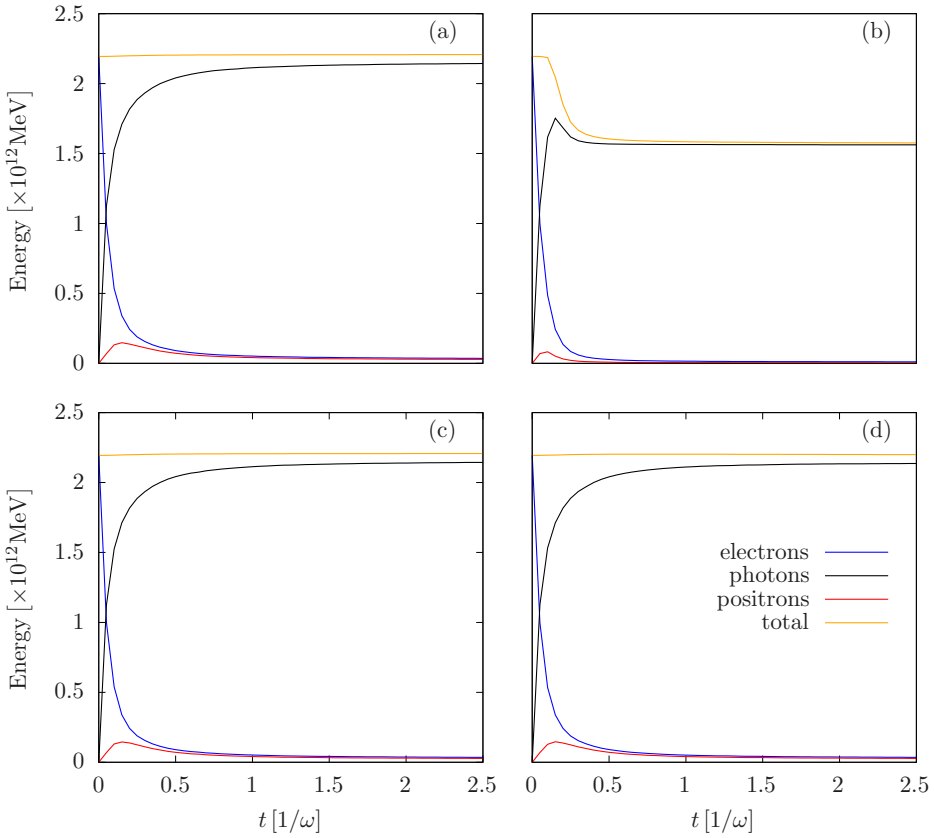

Figure 3.5.9: Energy of particle species over time for different merger. ((a) no merger, (b) simple merger, (c) Vranic particle merging algorithm and (d) Voronoi particle merging algorithm). Simulation of a magnetic shower.

3.5.7 Summary

This section has conducted an in-depth comparative analysis of three distinct merging algorithms: the simple merger, the two-particle merger by Vranic and the Voronoi particle merger. The central focus of the investigation revolved around two tests, designed to probe the efficiency and reliability of these algorithms.

Both the two-particle merger and the Voronoi particle merger demonstrated improvement over the simple merger. In the first test, these algorithms showed good capabilities in successfully merging while retaining the underlying physics. The second test further corroborated these results, with both algorithms accurately reproducing the correct energy spectra. These outcomes substantially reinforce the viability of these two algorithms as robust computational tools within the PIC code `VLPL`

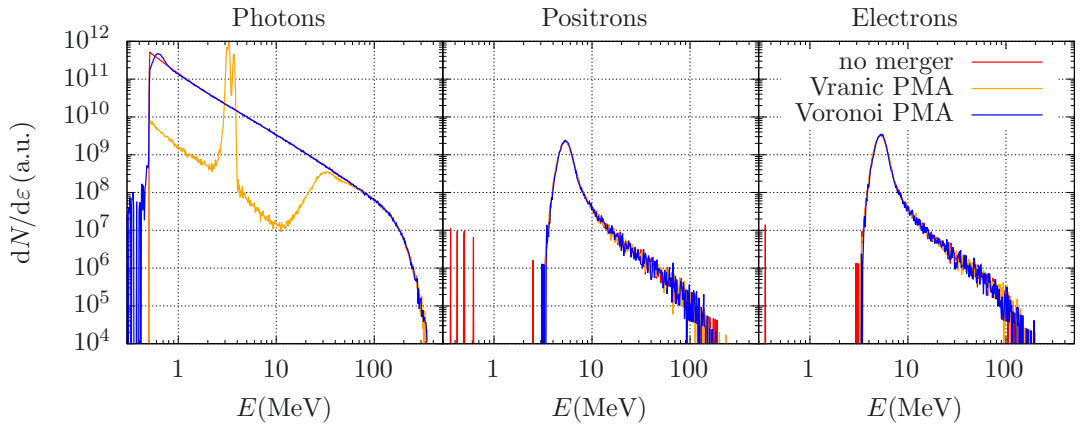

Figure 3.5.10: Particle spectra for photons, positrons and electrons in the magnetic shower test. Simulation of a magnetic shower.

It is important to note that a reasonable merge period is necessary to prevent non-physical merge attempts from accumulating and introducing new structures in the simulation. An inadequately calibrated merge period could potentially undermine the reliability of the algorithms, rendering the resulting data susceptible to inaccuracies.

Contribution of the author: The contribution of the author to the subsection 'Merging algorithms' is detailed here. M.F. implemented the framework for the merging algorithm and the merging algorithms. M.F. carried out all simulations and performed data analysis. M.F. also wrote the code for the data analysis.

4 Mitigation of errors in simulation of ultra-relativistic bunch propagation

After covering the numerical tools necessary for the study within this thesis, the following chapter will investigate the numerical tools further. As mentioned in the previous chapter, numerically solving the equations for the electromagnetic fields might introduce additional errors. Since most configurations in this thesis are using one-dimensional field propagation it is possible to mitigate them with the RIP solver.
Therefore, the following chapter aims to discuss the suppression of errors by the RIP solver in comparison to the Yee solver. The subject of study is the propagation of an ultra-relativistic electron bunch in a vacuum. Such bunches, used in bunch-bunch collisions in the following chapter, provide a good introduction to the subsequent chapters. Problems that may arise are the numerical Cherenkov instability and the phenomenon of self-interaction. For this purpose, the electron-bunch is propagated with the Yee solver for an initial review and then compared to the simulation with the RIP solver. It becomes visible that the simulation with the Yee solver deforms the electron bunch. On the other hand the RIP solver preserves the electron bunch density profile over the whole simulation.

In a second simulation series radiation reaction has been enabled. With radiation reaction, the instability that appeared in the simulation with the Yee solver lead to additional nonphysical behaviour. The electron bunch in the simulation with the Yee solver lost $\sim 91.4\%$ of its energy. Such nonphysical losses are mitigated if the RIP solver is used for the bunch propagation. Finally, selected particle trajectories will be shown for the Yee simulation to demonstrate the deformation of the bunch.

The results and content of this chapter are reused in a shortened form and adapted from the *Suppression of errors in simulated ultra-relativistic bunch propagation using the X-dispersionless Maxwell solver*, by Filipovic, M., Baumann, C. and Pukhov, A. (2022). Physical Review Accelerators and Beams, 25(5), 054405, licensed under CC

 In detail, section 4.1 is reused in a shortened version and sections 4.2, 4.3 and 4.4 are reused from [105], with the RR results and conclusion also being extended.

4.1 Introduction

The Yee algorithm, introduced in section 3.1.2, is subject to numerical errors, which results in a reduced velocity along all axes except maybe the grid diagonals. This is known as numerical dispersion and may trigger numerical instabilities, thus giving rise to non-physical behavior. One prominent example is the numerical Cherenkov instability (NCI) in relativistic plasma simulations [83, 106, 107]. The instability is linked to the well-known Cherenkov radiation that is emitted when charges are faster than the phase velocity in the current medium. The numerical counterpart arises accordingly, i.e. when charged particles are faster than the numerical phase velocity, it comes to a nonphysical coupling between electromagnetic modes and the particles. Physically, there should be no Cherenkov radiation in plasmas, because the phase velocity of electromagnetic modes in a background plasma is higher than the speed of light c. Unfortunately, simulations using the FDTD method such as the Yee scheme may show reduced phase velocities due to numerical dispersion. Therefore, NCI becomes visible once particle speed and phase velocity match.

The NCI has been studied by several groups over the past years [78, 79, 108–112] and solutions to suppress it have already been proposed since its first observation. Different options on how to achieve this are suggested in the literature like, for instance, the artificial increase of the speed of light in the field equations [107, 113], the definition of magnetic and electric field on the same spatial grid [107], the Galilean grid shift for a plasma flowing with uniform velocity [114] and other modification to the finite-difference time-domain algorithm [78]. Some other Maxwell solvers have also achieved the suppression of non-physical Cherenkov radiation from a relativistic beam [79, 111]. Implementations of the latter methods are described in the works [109, 115–119].

Apart from NCI, the Yee solver can also lead to a phenomenon known as numerical self-interaction. In that context, consider an ultra-relativistic high-current beam with Lorentz factor $\gamma_0 \gg 1$ and normalized velocity $\beta_\parallel \approx 1$ in vacuum. From the physics point, the electromagnetic self-field generated by such a beam is mainly transverse in the laboratory frame, and its electric and magnetic field are linked via the relation $B_\perp = \beta_\parallel E_\perp$ [120]. These beam fields cause an intrinsic force on a beam electron with

charge $-e$ itself,

$$F_\perp = -e\left(E_\perp - \beta_\parallel B_\perp\right) = -e\left(E_\perp - \beta_\parallel^2 E_\perp\right) = -\frac{eE_\perp}{\gamma_0^2}, \tag{4.1.1}$$

which is negligible in the ultra-relativistic limit. It is also noted, that relativistic electrons are subjected to a similar force when they are co-propagating with a laser wave [121].

Unfortunately, the Yee scheme can overestimate the intrinsic self-force by orders of magnitude, which is a result from the staggered definition of electric and magnetic fields on the Yee lattice. As will be shown later, this causes dramatic energy losses of the high-current beam with time when the RR effect is taken into account. Such artifacts of induced radiation losses due to the numerically enhanced self-interaction are highly undesirable for many reasons. First, they hinder the analysis from numerical modeling of RR, as it might be unclear what causes specific energy losses. And second, they can strongly alter the dynamics of a system. This is especially unwanted when radiation losses have to be avoided (see, for instance, the discussion on the fully nonperturbative regime of QED in references [37–40]). In other words, the Yee solver is not optimal for high-energy particle beams and should not be the first choice for accurate modeling.

In this chapter, the aforementioned problems will be tackled through the RIP solver initially developed for plasma-based acceleration [77]. The solver is dispersionless along the field propagation direction and the fields build rhombi-in-plane patterns. The scenario in which the problems are studied will be the vacuum propagation of a relativistic bunch, where non-physical Cherenkov radiation has been observed and linked to the Yee solver [78, 79].

4.2 Vacuum bunch propagation with different Maxwell solvers

Numerical simulations of the propagation of an ultra-relativistic electron bunch in vacuum are performed. The simulations are run with the two different solvers, namely the Yee and the RIP solver. Please note that the simulations are first conducted without considering RR.

4.2.1 Simulation setup

The vacuum bunch propagation is simulated within the framework of full three-dimensional PIC simulations using the code `VLPL` [45, 57]. This code can either use the Yee or the

RIP [77] Maxwell solver to advance electromagnetic fields. All simulations utilize the moving window approach in a simulation box with dimensions $20\sigma_0 \times 40\sigma_0 \times 40\sigma_0$ in $X \times Y \times Z$ direction, where σ_0 represents the normalization of length. The transverse cell size is always set to $0.1\sigma_0 \times 0.1\sigma_0$. However, the longitudinal cell size is different for the two Maxwell solvers. Along X, it is $0.1\sigma_0$ for Yee and $0.05\sigma_0$ for RIP. The difference in the longitudinal step size results from the stability condition of the different solvers. The time step is $c\tau = 0.05\sigma_0$ in all simulations. The implemented electron bunch is configured as a spherical cloud with a Gaussian density profile $n_e = n_0\, e^{-r^2/\left(4\sigma_r^2\right)}$, where n_0 and σ_r are the bunch's peak density and root mean square (rms) width, respectively. In these simulations, 8 particles per cell are used. Further, the electrons are propagating in x-direction with a momentum of $\mathbf{p}_0 = (p_{x0}, 0, 0)$. The boundaries of the simulation domain are absorbing for particles. At the beginning of the simulation, the fields on the grid generated by the electron bunch are initialized with a Poisson solver, using periodic boundaries as the initial condition. For the fields, the transverse boundaries are periodic and the longitudinal ones are absorbing.

In particular, the specific simulation parameters are: the peak density is $n_0 = 5n_c$ (here, $n_c = m_e c^2 \pi / e^2 \sigma_0^2$ is the "normalized density"), the initial momentum is $p_{x0}/(m_e c) = 2.5 \times 10^5$ (m_e is the electron mass), and the radius parameter is $\sigma_r = \sigma_0 = 10$ nm (Density in this configuration is normalized in a similar way as in laser plasma simulations, since `VLPL` is a relativistic PIC-code for such applications and ties densities to the normalization of all lengths.). Please note that the parameters are motivated by the electron bunch used in [38]. Such ultra-relativistic particle beams may radiate massively due to numerical self-action. For that reason it is important to minimize numerical errors and to ascertain the origin of the radiation. This numerical instability can pose a limitation on the bunch length when simulating beam-beam collisions. Increasing the bunch length as an example in beam-beam collisions [38] increases the total simulation time where numerical errors can occur. In these simulations, the particles are not pushed until time $\approx 9\,T_b$, where T_b is the inverse of the relativistically corrected beam plasma frequency,

$$T_b = \omega_b^{-1} = \sqrt{\gamma_0 m_e / \left(4\pi e^2 n_0\right)}. \tag{4.2.1}$$

This time-frame ensures that small non-physical fields emerging due to bunch initialization are cleared away and do not spoil the particle dynamics once momentum updates are applied. In this sense, the bunch propagates in self-consistent numerical grid fields, so that vacuum propagation can be simulated with higher accuracy for the case using the Yee solver. Subsequently, time $t = 0$ is measured relative to this time period.

4.2.2 Simulation results

Figure 4.2.1 presents data in the x-y-plane for the electron density and the transverse force obtained in simulations with the Yee solver [see subplots (a) and (c)] and the RIP solver [see subplots (b) and (d)]. After a simulation time of $t/T_b = 10$, the electron bunch is strongly deformed with the Yee solver [see Fig. 4.2.1(a)]. The bunch has been compressed which increases the peak density to $18.3 n_c$. In addition, the initial Gaussian density profile cannot be recognized anymore. The right-hand side of the bunch focuses and the left-hand side smears out. Similar observations can be seen in the transverse force. It should be noted that the transverse force is slightly redefined with respect to Eq. (4.1.1). From now on, the transverse force is calculated from $F_y = E_y - B_z$, which has the advantage to be expressed solely by the fields and corresponds to ultra-relativistic particles moving with nearly speed of light, $\beta = 1$. Figure (4.2.1)(c) shows similar deformations also in the force. One can see waves at the rear that are too slow to co-move with the bunch and form the Cherenkov cone. In addition, the force has built up significant amplitudes during the simulation. For instance, peak values of approximately $29\, m_e c^2/\sigma_0$ can be retrieved from the data which are definitely not negligible, so clearly indicating the onset of an instability.

The RIP solver in comparison does not create any visible numerical error during the simulation. The initial density profile is still preserved, which is expected for an ultra-relativistic electron bunch propagating in vacuum as it experiences almost no self-interaction. The transverse force in this case is 10 orders of magnitude lower than in the simulation with the Yee scheme after the same simulation time. Moreover, the RIP simulation precisely reproduces the prediction for the self-force. Analytically, the self-force can be written along the y-axis as $F_y(y) = -eE_y(y)/\left(2\gamma_0^2\right)$ [see the additional factor $1/2$ compared to Eq. (4.1.1) due to the re-definition of $F_\perp$]. Figure 4.2.2 shows the transverse force F_y as a function of y at time $t/T_b = 10$ for a fixed x-value of $(x-ct)/\sigma_0 = 10$. The analytical solution is in a good agreement with the simulation data obtained by the RIP solver, whereas the data obtained by the Yee solver is ruined by numerical artefacts. Here, the faulty transverse force has been amplified and is 10 orders of magnitudes bigger than the expected analytical solution. The transverse force obtained by the RIP solver shows a small discrepancy at large values of y ($|y| > 7.5\sigma_0$) in comparison to the analytical solution. This is due to the chosen periodic boundary conditions, which means that there is another electron bunch beyond the transverse boundaries. Their fields are directed such, that they cancel the field of the main bunch at large coordinates and therefore the transverse force decreases faster in the simulations than the analytical solution. This effect becomes less prominent if one increases the

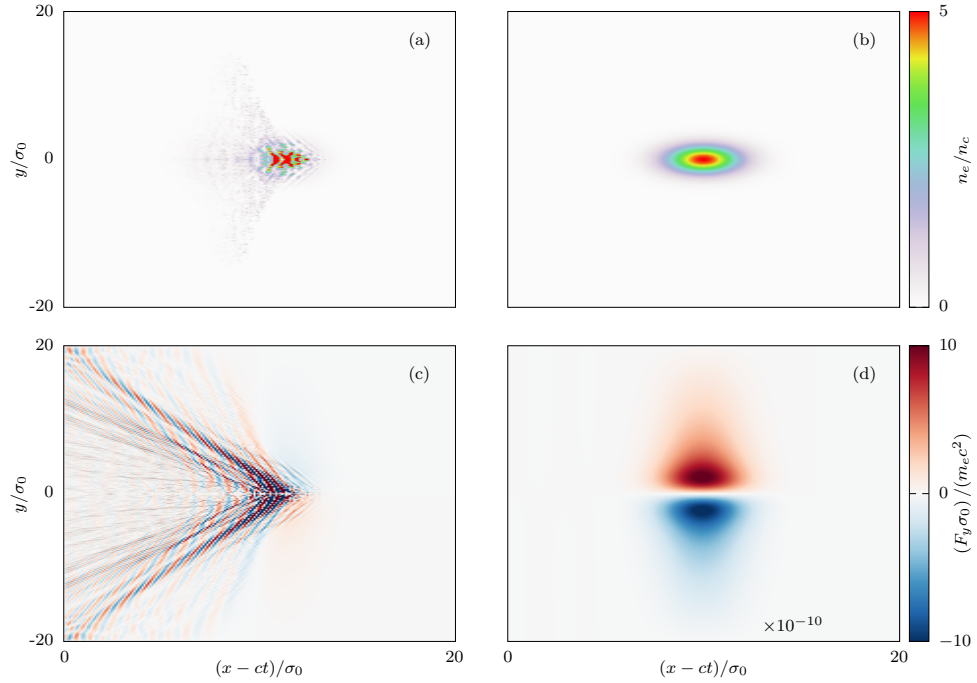

Figure 4.2.1: Ultra relativistic electron bunch propagating in vacuum without RR. Data for electron density [see (a) and (b)] and transverse force [see (c) and (d)] are shown at time $t/T_b = 10$. Subplots (a) and (c) show the results for the Yee solver, while (b) and (d) show the results for the RIP scheme. It is further noted that the data in (d) are scaled in order to apply the same colorbar. *Source: [105], licensed under CC BY 4.0* (https://creativecommons.org/licenses/by/4.0/).

transverse size of the simulation domain. It can already be seen that the RIP solver yields a reduction of numerical errors.

4.2.3 Numerical Cherenkov instability in Maxwell solvers

To identify the observed numerical error in the configuration as the NCI, a brief explanation is necessary to understand how the numerical approach gives rise to instabilities in the simulation. For that reason, it is important to take a look at the dispersion relation of the algorithms which are used to solve Maxwell equations.

The numerical instability appears if the dispersion relation of a numerical Maxwell solver allows electromagnetic modes which have a lower phase velocity v_{ph} than the speed of

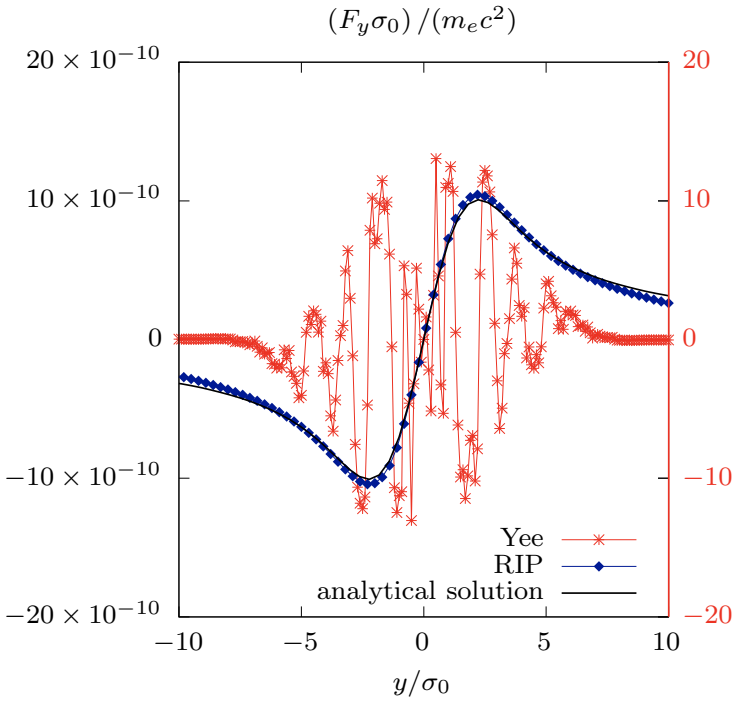

Figure 4.2.2: Transverse force at $t/T_b = 10$ for a fixed x-value of $(x-ct)/\sigma_0 = 10$. Transverse force obtained by the Yee solver uses red y-axis. *Source: [105], licensed under CC BY 4.0* (https://creativecommons.org/licenses/by/4.0/).

light c. Particles that travel close to c are now able to excite these modes and produce numerical Cherenkov radiation [114]. Therefore, it is likely that an ultra-relativistic electron bunch propagating in vacuum can excite such modes.

To determine the modes that are excited, it is first necessary to find the dispersion relations for the Maxwell solvers. This is usually done by inserting plane waves of the form

$$\mathbf{A} = \mathbf{A}_0 \exp\left(-i\omega t + i\mathbf{kr}\right) \tag{4.2.2}$$

into the numerical marching equations of the Maxwell solver (a detailed calculation can be found in [122]). The plane-wave analysis gives for the Yee solver

$$\frac{1}{h_x^2}\sin^2\left(\frac{k_x h_x}{2}\right) + \frac{1}{h_y^2}\sin^2\left(\frac{k_y h_y}{2}\right) + \frac{1}{h_z^2}\sin^2\left(\frac{k_z h_z}{2}\right) = \frac{1}{c^2\tau^2}\sin^2\left(\frac{\omega\tau}{2}\right) \tag{4.2.3}$$

and for the RIP solver in the special case of $c\tau = h_x$

$$\begin{aligned}\frac{1}{h_x^2}\sin^2\left(\frac{\omega h_x}{2c}\right) = \frac{1}{h_x^2}\sin^2\left(\frac{k_x h_x}{2}\right) + \\ + \left[1-\sin^2\left(\frac{k_x h_x}{2}\right)\right]\left[\frac{1}{h_y^2}\sin^2\left(\frac{k_y h_y}{2}\right) + \frac{1}{h_z^2}\sin^2\left(\frac{k_z h_z}{2}\right)\right].\end{aligned} \tag{4.2.4}$$

The Yee dispersion relation suffers from v_{ph} different of c for all wavenumbers except electromagnetic waves running along the grid diagonals, of $k_x = k_y$, $k_x = k_z$ or $k_y = k_z$ under the upper limit of the Courant-Friedrichs-Lewy (CFL) condition. The RIP solver is dispersionless for propagations along the x-axis and exhibits similar properties in one dimensional problems as the 1D advective solver by Birdsall and Langdon [44, 77]. Both solvers store the transverse fields on the same integral positions and require the longitudinal grid step to be equal to the timestep. These properties suppress non-physical effects for $kh_x \sim \pm\pi$ [44]. Inserting $k_y = k_z = 0$ in the RIP dispersion relation (Eq. 4.2.4) the equation reduces to $k_x = \omega/c$. For purely transverse wavenumbers with $k_x = 0$ the RIP dispersion relation transforms to the 2D Yee dispersion relation [77]. One needs to be aware, that just by plugging in $k_y = k_z = 0$ into the Yee dispersion relation the Maxwell solver does not become dispersion free. Stability of a Maxwell solver is as above mentioned also described by the CFL-condition. The condition describes whether the used domain step sizes of the grid and the timestep can guarantee, that the propagation of fields is not faster than the phase velocity. The CFL condition of the Yee solver in a 3D-space reads $c\tau < 1/\sqrt{(1/h_x)^2 + (1/h_y)^2 + (1/h_z)^2}$ [54, 80]. The dispersionless property of the RIP solver should become advantageous for the considered configuration in this chapter, since the electron bunch produces an electromagnetic field, which co-propagates along the x-axis.

Linking the observed instability to the numerical Cherenkov instability can be confirmed the same way as performed by Lehe et al. in their study of the numerical Cherenkov effect [79]. Here, the solution of the Yee dispersion relation for excitable modes by the NCI are calculated and compared the 2D-FFT of the E_y-component. Figure 4.2.3 displays the FFT of the component and highlighting the excitable mode with a dashed line similarly. This figure greatly coincides with the result in the work of Lehe et al. [79].

4.3 Vacuum bunch propagation with radiation reaction

In this section, the impact of RR on the vacuum bunch propagation of an ultra-relativistic electron bunch is studied for two Maxwell solvers. The other simulation parameters are unchanged with regard to the previous section. Figure 4.3.1 shows the results of the simulations with the additional force, again showing the density of the electron bunch [see Fig. 4.3.1(a) and (b)] and the transverse force F_y [see Fig. 4.3.1(c) and (d)]. Again, one can observe a disruption of the electron bunch when using the Yee solver

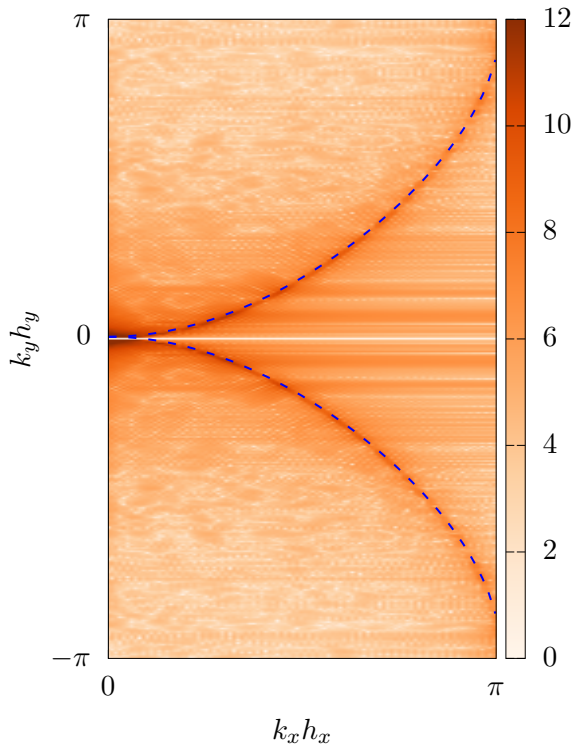

Figure 4.2.3: Intensity of the spatial 2D-FFT E_y-component for $k_z = 0$ at time $t/T_b = 10$. Dashed line indicate the mode satisfying dispersion relation for $v_{ph} = c$. *Source: [105], licensed under CC BY 4.0* (https://creativecommons.org/licenses/by/4.0/).

[Fig. 4.3.1(a)]. This time the peak electron density is about $\approx 11.96 n_c$ which is lower in comparison to the case Yee solver without RR. This already indicates that RR further alters the bunch dynamics. In contrast, the RIP solver once more does not show an instability and preserves the distribution of the electron bunch.

The maximum value of the transverse force is reduced in comparison to the simulation without RR [Fig. 4.3.1(c)], which is a result of the stronger electron bunch defocusing. One can see that the simulation performed with the RIP solver does not show these shortcomings and the behavior of the electron bunch is similar to the previous simulation, so that it is not further influenced by enabling RR.

In the next step, spatial Fourier transforms of the field E_y will be used as a diagnostic for NCI. Figure 4.3.2 shows the Fourier transform of E_y for all previous simulations in the x-y plane. The Yee-scheme produces, regardless of whether the radiation reaction is enabled or not, the typical signal, which was earlier concluded to be the one excited through the NCI. The proposed RIP scheme produces no additional transverse signals and has only visible amplitude at low k_x values. Since the signal is not visible in the

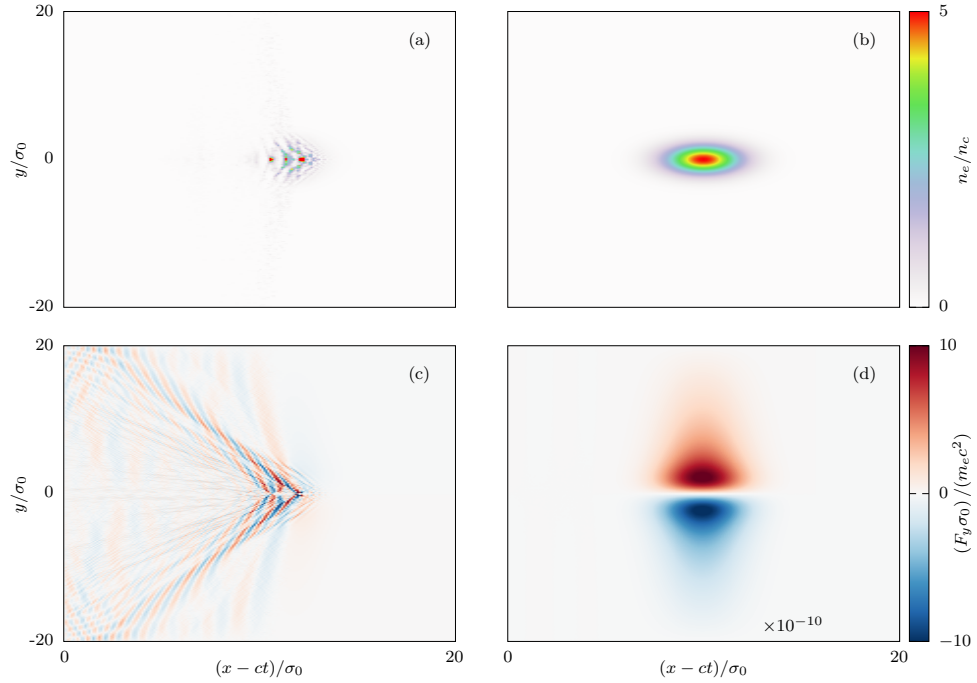

Figure 4.3.1: Ultra-relativistic electron bunch propagating in vacuum with RR. Normalized electron density in n_e/n_c and the transverse force in dimensionless unit $(F_y\sigma_0)/(m_ec^2)$ are shown after $t/T_b = 10$. Subplots (a) and (c) show the data of the Yee solver and subplots (b) and (d) the RIP solver. RR force is enabled in both simulations. Peak density of the data produced with the Yee solver increases to $n_e \approx 11.96 n_c$. *Source: [105], licensed under CC BY 4.0* (https://creativecommons.org/licenses/by/4.0/).

simulation data produced with the RIP solver, numerical Cherenkov radiation has been suppressed in this diagnostic.

In principle, an ultra-relativistic bunch propagating purely along X should not be accompanied by a longitudinal magnetic field component B_x [120]. Therefore, the field energy associated with the longitudinal magnetic field component,

$$W_{B_x} = \frac{1}{8\pi} \int B_x^2 \, \mathrm{d}V, \tag{4.3.1}$$

can be used as a further tool to check for the validity of all simulations. Figure 4.3.3 presents the longitudinal magnetic field energy (calculated with eq. 4.3.1) as a log-plot. The data show that both simulations with the RIP solver generate a negligible field, which is many orders of magnitudes below the level of the Yee simulations. Moreover, the RR does not impact the RIP simulations. On the contrary, one can immediately see

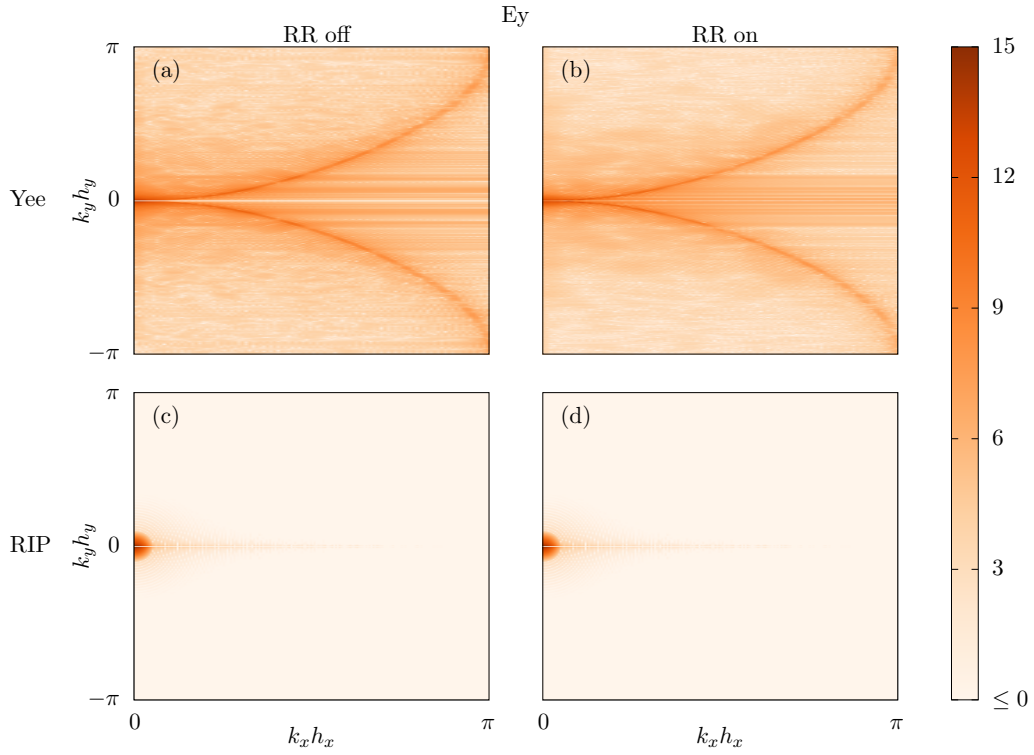

Figure 4.3.2: Intensity of the 2D-FFT E_y-component for $k_z = 0$ at time $t/T_b = 10$. Subplots (a) and (b) are the solution of the Yee scheme and (c) and (d) subplots data of the RIP scheme. (a) and (c) have disabled RR, (b) and (d) have enabled RR. NCI is visible for Yee solver, because of the evident outline of a mode.

that significant longitudinal magnetic fields are generated in the Yee simulations, which rise further within the simulation. In the beginning, the evolution of W_{B_x} shows a linear course in the log-plot and is also independent of the RR force. After the distortion of the electron bunch the linear trend changes and a second jump becomes apparent. In the following, one can observe that the evolution with and without RR splits up, and the simulation with enabled RR increases further to a certain value after which it slowly decays. The data obtained without RR rises slower from that time, so that it looks like the instability is enhanced when the RR force is included.

It can be seen that the RR leads to additional numerical artifacts in the vacuum propagation when using the Yee solver. However, there is even another quantity that gets strongly affected and clearly shows non-physical behavior. As the correct self-force is miniscule $[(F_\perp \sigma_0)/(m_e c^2) \sim 10^{-10}$ according to Eq. (4.1.1)], the characteristic radiation loss time ν_{RR}^{-1} is very long compared to the timescale T_b. Physically, this means that electrons should not suffer synchrotron radiation losses. Figure 4.3.4 depicts the simulation results

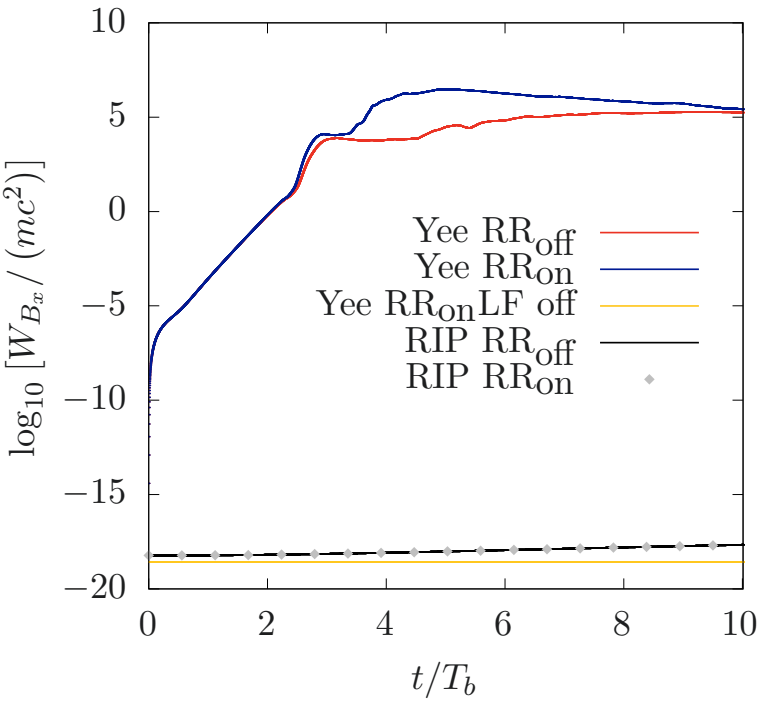

Figure 4.3.3: Longitudinal magnetic field energy evolution for different Maxwell solvers and with or without accounting for RR. Additionally, the yellow line represents the simulation, where the fields are updated with the Yee solver, and the particles are solely pushed by the RR force, i.e. the momentum change by the Lorentz force (LF) has been ignored. *Source: [105], licensed under CC BY 4.0* (https://creativecommons.org/licenses/by/4.0/).

for the energy ε of the electron bunch as a function of time (Yee and RIP solver with and without RR). In the simulation with RR and the Yee solver (blue curve), the particles are losing a significant amount of their initial energy ε_0 over time. The onset of the energy loss starts at time $t/T_b \approx 2$, which is also roughly the time at which the NCI begins. Afterwards a major drop of the particle energy can be observed. Till the end of the simulation time the energy of the electrons is reduced by $\sim 91.4\%$. Such a dramatic drop in energy cannot be observed in any of the other simulations, so that it is not the result of the NCI alone.

In the other simulations, the particles are losing $\sim 4.4\%$ of their initial energy, and the energy loss scales linearly with time. This linear behavior comes from the non-vanishing field E_x, which is doing work of $-eE_xct$ on the bunch electrons. Thereby, the RIP simulation is in excellent agreement with the corresponding loss of energy when using the numerical data for E_x. The E_x field emerges in the PIC simulations because of the

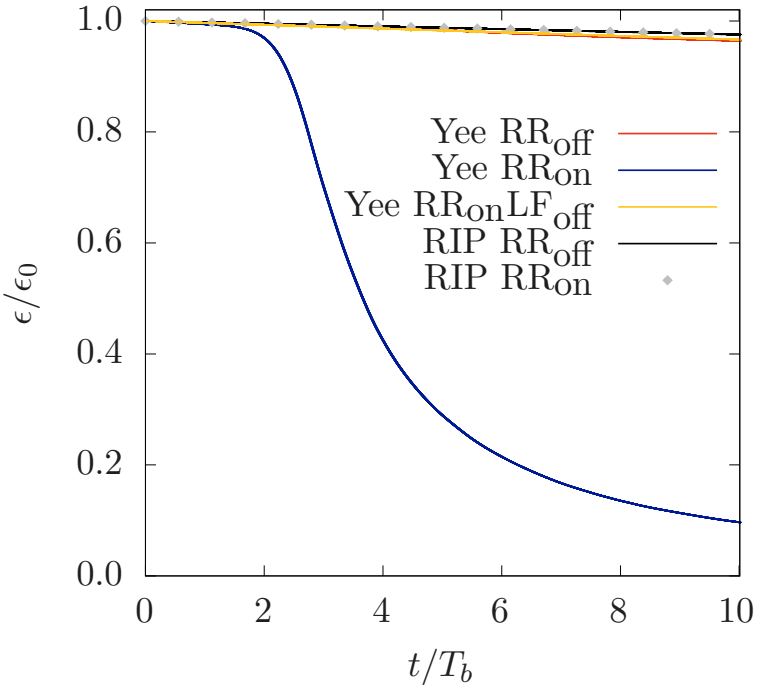

Figure 4.3.4: Relative particle energy over time for an ultra-relativistic electron bunch propagating in vacuum. Additionally, the yellow line represents the simulation, where the fields are updated with the Yee solver, and the particles are solely pushed by the RR force, i.e. the momentum change by the Lorentz force (LF) has been ignored. *Source: [105], licensed under CC BY 4.0* (https://creativecommons.org/licenses/by/4.0/).

finite transverse size of the simulation box $L_\perp$ and scales as $E_x \sim L_\perp^{-2}$.

In a next step, it is of interest to confirm, whether the rapid growth of the instability is due to the feedback loop between the emission of electromagnetic fields and their influence on the particle. To clarify the instability, an additional simulation has been performed with the same parameters, but removed the Lorentz force from the particle pusher. Yet, the radiation reaction force is kept being calculated on the electromagnetic fields at the particle position. In this regard the feedback of emitted fields is suppressed on particles via Lorentz force.

The simulation data shows that indeed the radiation of the electron bunch does not change significantly in this case. A relative energy loss of 5.82% at $t/T_b = 10$ has been recorded and can be seen in Figure 4.3.4 (yellow curve). Therefore, the enabled RR force is not the primary factor causing the massive energy loss that has been observed earlier with all forces taken in consideration. Figure 4.3.5 shows the maximum quantum parameter in a cell with the electrons density overlapped at $t/T_b = 10$ with subplot (a) showing the slice

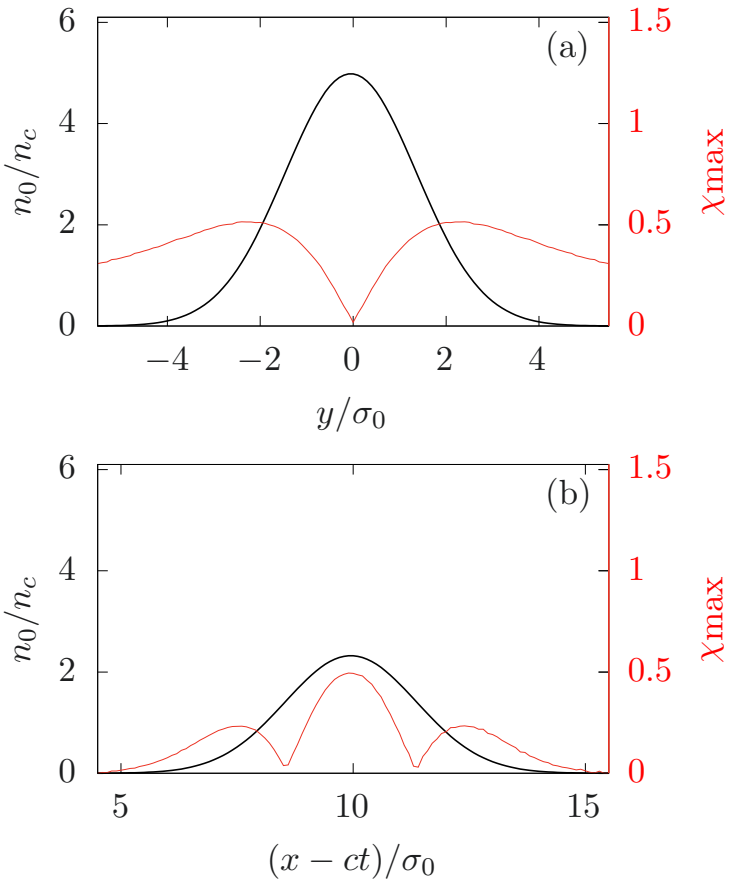

Figure 4.3.5: 3D PIC simulation result of an electron bunch propagating in a vacuum. Simulations have been performed with the Yee solver, activated radiation reaction force and disabled Lorentz force. Subplot (a) shows the electron density in critical densities and maximum quantum parameter within a cell for a fixed $(x-ct)/\sigma_0 = 20$ and $z/\sigma_0 = 0$. Subplot (b) shows electron density and χ_{max} for a fixed $y/\sigma_0 = 1.8$ and $z/\sigma_0 = 0$, which slices the domain through the highest recorded quantum parameter value. *Source: [105], licensed under CC BY 4.0* (https://creativecommons.org/licenses/by/4.0/).

through the maximum electron density and (b) the slice through the maximum quantum parameter. Here, the electron bunch has not been deteriorated by the RR force alone. The reason for that lies within the quantum parameter, which is still low and higher values can only be found at low electron density regions, as the maximum quantum parameter is not located in the center of the bunch. In contrast the maximum quantum parameter rises to a value of 153.16 at $t/T_b \sim 2.68$ for the simulation with both the Yee mesh and the RR-module used. This brings the electron bunch into a region, where QED effects would

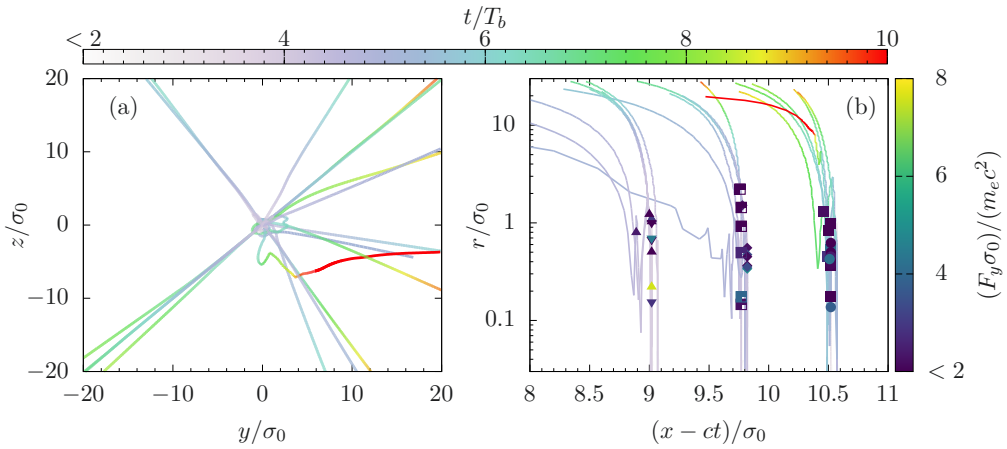

Figure 4.3.6: 3D PIC simulation result of an electron bunch propagating in a vacuum. Here, 18 different particles have been tracked and the transverse force in their cell documented. Simulations have been performed with the Yee solver and activated radiation reaction force. Subplot (a) shows the particle displacement in x and y direction. (b) shows the tracked particles in a $x-r-F_y$-plot. The trajectories are colored according to the simulation time. The points on certain times is color coded according to the transverse force within the cell, where the particle is currently located. Only transverse force values bigger than 2 have been displayed. Forces are displayed for 2 particles at an initial $(x-ct)/\sigma_0 = 9.00$, $(x-ct)/\sigma_0 = 9.75$ and $(x-ct)/\sigma_0 = 10.50$. *Source: [105], licensed under CC BY 4.0* (https://creativecommons.org/licenses/by/4.0/).

become likely and the RR force applies a strong dampening on the particles. Therefore, the Lorentz force is necessary to grow the feedback between the fields and the dynamics of the particles and characteristic for a numerical Cherenkov instability.

Finally, to advance the discussion of particle dynamics within the electron bunch several particles have been tracked through the vacuum propagation computed with the Yee solver and taking the RR force in consideration. Particles which have been tracked were chosen at various position within the electron density. The tracked particle results are summarized in figure 4.3.6. Subplot (a) shows the trajectories of the tracked particle in the yz-plane with the time being color coded. Once the instability takes place particles are scattered to the edge. Subplot (b) adds the transverse force F_y while showing the radial and longitudinal displacement. Particles start to deflect only radially first, since they are impacted by the transverse force. The first major transverse force influence occurs at $t \sim 2.5T_b$. Once the initial displacement takes place all particles decelerate and fall behind, reducing their initial x-position within the bunch. No strong transverse force

can be seen at that point. After getting decelerated the particles start to leave the moving simulation domain and are finally lost.

In summary, the data of the energy loss show that the Yee solver may lead to completely wrong predictions. This in turn can have major impact on the system dynamics.

4.4 Conclusion

In this chapter, the vacuum propagation of an ultra-relativistic electron bunch was studied in the framework of PIC simulations. Special focus was laid on the question how the bunch dynamics will change if different Maxwell solvers are used. The standard Yee solver was shown to be plagued with the NCI. As a result, the density profile of the ultra-relativistic electron bunch was significantly deformed over time. The addition of the RR effect in the simulation aggravates numerical problems of the Yee solver and leads to non-physical energy losses. The bunch electrons lost about 90% of their initial energy.

In contrast, these numerical artefacts were absent when using the RIP solver. This solver has the advantage to define electric and magnetic field at same grid points and to be dispersion-free. The density profile of the electron bunch remained preserved over the entire simulation time.The incorporation of the RR force did not cause any numerical problems in this case. In particular, non-physical radiation losses were not detected.

In conclusion, the RIP solver showed very good results in the considered configuration and is a potential method to suppress the NIC as well as non-physical radiation losses and thus is a very good choice for high energy physics simulations. It makes it possible to study high-energy particle beams in quasi 1D problems for several periods, such as long bunch propagation, beam-beam collisions along one axis with high bunch lengths, and laser wake field acceleration.

This research topic is essential as it functions as an introduction to the following study of the collision of ultra-relativistic electron bunches. It helps establish that the RIP solver is a great Maxwell solver for these kind of scenarios and will be used onward in this thesis.

As a prospect for future studies the improvement of the current Maxwell solvers can be considered since one-dimensional field propagation are not the only topics in laser-plasma interaction. In a later chapter the laser approaches the target under an angle and scatters on the surface, therefore a different Maxwell solver might be beneficial and should be compared for different solvers.

Contribution of the author: The chapter contains the results and discussion of the publication [105]. A.P. conceived the configuration and M.F. carried out all simulations and performed data analysis. M.F. wrote the code for the data analysis. C.B., M.F. and A.P. clarified details of the physics. C.B. wrote the part about self-force in the introduction and the implementation of RR and M.F. wrote the rest of the manuscript. All authors commented on it.

5 Reaching nonperturbative QED in modified bunch collision configuration

After establishing that the RIP Maxwell solver is the preferred option in simulating field developments for one dimensional propagation, the study shifts the focus on configurations to study QED processes. Therefore, a previously published discussion on bunch-bunch collision [38] is revisited to research the possibility to reach an extremely high-value of the quantum non-linearity parameter with a modification of the configuration. The modification at hand shifts the propagation axis of both bunches slightly in transverse direction. The aim is that each bunch propagates through the field maximum of the counter-propagating bunch to interact with strong fields. This leads to an increased production of secondary particles by QED effects. It is conjectured that when the quantum non-linearity parameter χ reaches ~ 1600, the QED theory becomes fully nonperturbative [42, 43]. Nearly $\sim 33\%$ of the initial particles reach the fully nonperturbative regime in the modified configuration.

Additionally, longer bunches and their influence on secondary particles were considered. The bunch length has been increased in 10nm increments. These results were compared to literature [123, 124], where they were in a great agreement for shorter bunch lengths. For longer bunch lengths the results were still in a good agreement, but the ratio of new particles per initial particles hints at a different trend.

The results and content of this chapter are adapted and reused from the *Effect of transverse displacement of charged particle beams on QED processes during their collision* by Filipovic, M., Baumann, C., Pukhov, A., Samsonov, A. and Kostyukov, I. (2021), Quantum Electronics, 51, 807. In detail, section 5.3 has been reused and sections 5.4 and 5.5 have been reused and extended from the aforementioned work [125].

5.1 Introduction

With the previous chapter finishing the discussion of numerical tools and instabilities the following parts propose configurations for the study of QED effects. As already covered in section 2.4 the quantum parameter χ classifies different regimes. The supercritical regime is defined as $\chi \gtrsim 1$ [126] and for $\chi \gtrsim 1600$ the theory becomes fully nonperturbative. Reaching these regimes is desired as they are only partially understood. QED theory was already probed for $\chi \lesssim 1$ with the experiment E-144 at the Stanford Linear Accelerator Center [27, 28]. In these experiments four laser photons interact with an electron during multiphoton Compton scattering which are in agreement with theories, as well as inelastic light by light scattering producing positrons is observed. Other experiments followed in the study of QED [127–129], but were not able to achieve $\chi \gg 10$.

At stronger fields and higher particle energies, radiative corrections become increasingly important. Here, cascade-like behaviour can be observed. High-energy particles emit virtual photons and high-energy photons temporary decay in a virtual electron-positron pair occurs. Multiple generations of these processes can be described as a QED cascade. It was conjectured by Ritus and Narozhny that the perturbative approach of the loop corrections breaks down after realizing the condition $\alpha\chi^{2/3} \geq 1$ [41, 42] with α being the fine structure constant. Therefore, reaching the fully nonperturbative QED requires the quantum non-linearity parameter of ~ 1600.

Experimentally it is not yet feasible to achieve the fully nonperturbative QED regime, but various initial analytic studies were conducted [43, 130, 131] and configurations proposed [39, 40, 132]. A different approach and the focus of the chapter is the proposed configuration of Yakimenko *et al.* [38] that uses collisions between high-energy electron bunches or electron bunch on positron bunch to reach the regime. These bunches require energies of 100GeV and to be tightly compressed and focused to minimize radiation losses. The electromagnetic field generated by the ultra-relativistic bunches would suffice to reach the threshold of the fully nonperturbative QED regime. The particle bunches propagate towards each other on the same axis and have Gaussian charge-density distributions similar as in section 4.2.3. Parts of high-density bunches of charged particles interacting with the field of the counter-propagating bunch would reach the fully nonperturbative QED regime.

Here, a modification on the configuration of Yakimenko *et al.* [38] is proposed. The propagation axes of the high-density bunches are shifted. It is desired that the peak density of one bunch interacts with the maximum field of the counter-propagating electron bunch. Doing so, an increased secondary particle production by the nonlinear Compton scattering and multi-photon Breit-Wheeler pair production is witnessed. Triggering in

general more of these processes will also result in higher energy losses of the electron bunches. Further, shifting the propagation axis has an influence on beam dynamics as the self-generated fields disrupt the counter-propagating bunch and should be compared in-depth with the head-on collision. It is necessary to study such a configuration as the QED theory is not established in the regime of fully nonperturbative QED.
One might contemplate replacing one of the electron bunches with a laser to achieve a sufficiently strong electromagnetic field to reach the fully nonperturbative QED regime and to mitigate the difficulties of performing a precise head-on collision. But even in facilities with a peak power of 10PW the collision would require an electron bunch with a Lorentz factor of $\gamma = 10^7$. Therefore this approach is difficult to be seen in the near future and the focus remains on bunch-bunch collisions.

In this chapter, the nonperturbative collider configuration proposed by Yakimenko *et al.* [38] will be compared by the configuration with shifted propagation axes proposed in this thesis. Thereafter, the influence of longer bunches in the head-on collision and configuration with shifted propagation axis is studied. In the framework of three-dimensional PIC simulations the comparison of particle yields, energy spectra and particles reaching the $\chi \gtrsim 1600$ threshold for the fully nonperturbative QED regime will be discussed.

5.2 Reference particle collider to reach nonperturbative QED regime

Yakimenko *et al.* proposed in their work [38] the use of a bunch-bunch collider to probe the fully nonperturbative QED regime. The reason for such an approach is the mitigation of radiative losses through beamstrahlung. The proposed configuration uses 100 GeV electron-electron bunch or electron-positron bunch collisions to reach the regime. Both bunches should have similar parameters with $\sigma_x = 10$nm bunch length, $\sigma_r = 10$nm bunch radius and $I_A = 1.7$MA peak current. These parameters are chosen, because they achieve a disruption parameter of $D \ll 1$. The disruption parameter defines the transverse motion of the particles within a bunch. The disruption parameter scales as

$$D \sim \frac{N\alpha\lambda_C\sigma_x}{\sigma_r^2} \tag{5.2.1}$$

with N the number of particles per bunch, $\alpha \approx 1/137$ the fine-structure constant and λ_C the reduced Compton wavelength [38]. An illustration of the scheme can bee seen in figure 5.2.1. Both bunches propagate towards each other on the same axis to facilitate

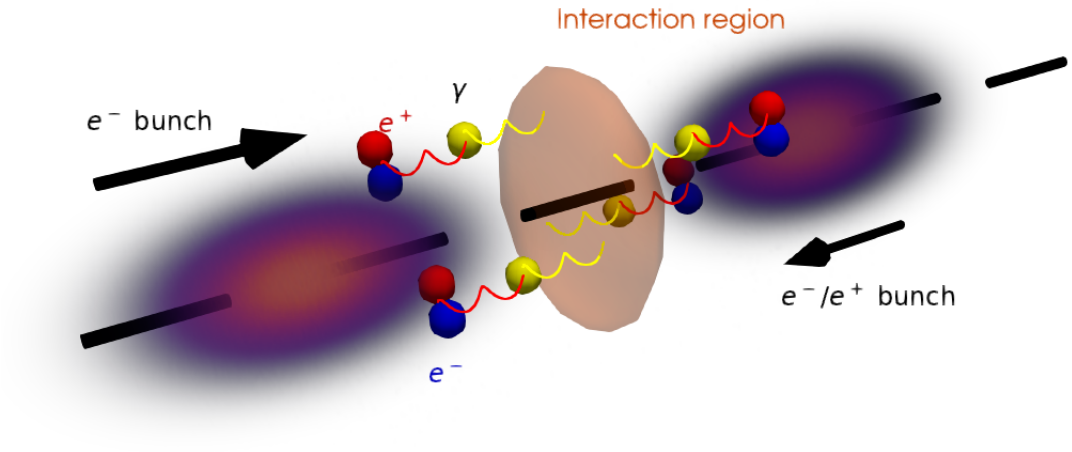

Figure 5.2.1: Scheme of the bunch-bunch collider proposed by Yakimenko *et al.* [38]. Arrows indicate the propagation direction. In the interaction region both bunches start to overlap and nonlinear Compton scattering and Breit-Wheeler pair production process can occur.

their interaction.

Their simulation results, which were presented to demonstrate the feasibility of the collider, showed that 38% of the bunch electrons reached the fully nonperturbative QED regime, satisfying the requirement $\alpha\chi^2/3 \geq 1$. During the collision, the bunches lost a maximum of only $\lesssim 5\%$ of their beam energy [38]. These simulations will be replicated with similar parameters in the following.

5.3 Transverse displacement of electron bunches during their collision

To compare the collision of bunches, numerical simulations by the particle-in-cell (PIC) method using the virtual laser plasma laboratory (VLPL) code [45, 57] in three-dimensional geometry are performed. The simulation domain is $20\sigma_0$, $30\sigma_0$, and $30\sigma_0$ along the x, y, and z axes, respectively, where $\sigma_0 = 10$nm is the characteristic spatial

size used for normalization in each simulation. The grid steps are $0.025\sigma_0$, $0.1\sigma_0$, and $0.1\sigma_0$ along the same axes. The diameter and length of the bunches are 10nm (unless indicated otherwise), the peak current is $I_{\max} = 1.7$MA, the Lorentz factor of the particles is $\gamma = 2.5 \times 10^5$, and a Gaussian ellipsoid is used as the density profile. For all the calculations performed, the transverse boundary conditions are periodic, and the longitudinal ones are absorbing. QED processes in this code are simulated using the Monte Carlo method [72, 133]. In the calculations performed, two QED processes are taken into account, the nonlinear Compton scattering and the Breit–Wheeler process. In this chapter, two possible configurations are considered. In the first configuration, hereinafter called 'undisplaced', the transverse positions of the centres of the two electron bunches coincide. The second configuration, called 'displaced', is schematically shown in Figure 5.3.1. In this case, one of the two electron bunches is displaced relative to the other in the direction of the y axis by a distance d_0. This distance is chosen such that the density maximum of one electron bunch passes through the electric field maximum of the counter-propagating bunch. The expressions for the electric and magnetic field strengths can be derived from the Gauss theorem [120]:

$$\mathbf{E} = -\frac{4\pi\sigma_r^2 n_0 e}{r} \exp\left(-\frac{(x-vt)^2}{2\sigma_x^2}\right)\left[1-\exp\left(-\frac{r^2}{2\sigma_r^2}\right)\right]\mathbf{e}_r \tag{5.3.1}$$

$$\mathbf{B} = -\frac{4\pi\sigma_r^2 n_0 e}{r}\frac{v}{c} \exp\left(-\frac{(x-vt)^2}{2\sigma_x^2}\right)\left[1-\exp\left(-\frac{r^2}{2\sigma_r^2}\right)\right]\mathbf{e}_\phi \tag{5.3.2}$$

where σ_r is the root-mean-square bunch radius; σ_x is the root-mean-square length of the bunch (note that below the results of modelling with different bunch lengths σ_x will be presented); $v \approx c$ is the speed of the bunch particles; and n_0 is the peak density of bunch particles [120]. For the simulation parameters above, the maximum electric field $E_{\max} = 13.8\left(2\pi m_e c^2\right) \times (e\sigma_0)^{-1}$ is achieved at $r_{\max} \approx 1.59\sigma_r$. Thus, the optimal shift for the displaced configuration is $d_0 = r_{\max} \approx 15.9$nm.

5.4 Results

First of all, particles were able to reach the fully nonperturbative QED regime, realised under the condition $\alpha\chi^{2/3}$, or $\chi \geq 1600$. Figure 5.3.2 shows the maximum values of the parameter χ in the yz plane at complete overlap of both bunches. Large χ values are observed in a ring around the bunch propagation axis for an undisplaced configuration (Fig. 5.3.2(a)) and in two rings for a displaced configuration (Figs 5.3.2(b), 5.3.2(c)). The reason for this distribution of the parameter χ is related to its dependence on the

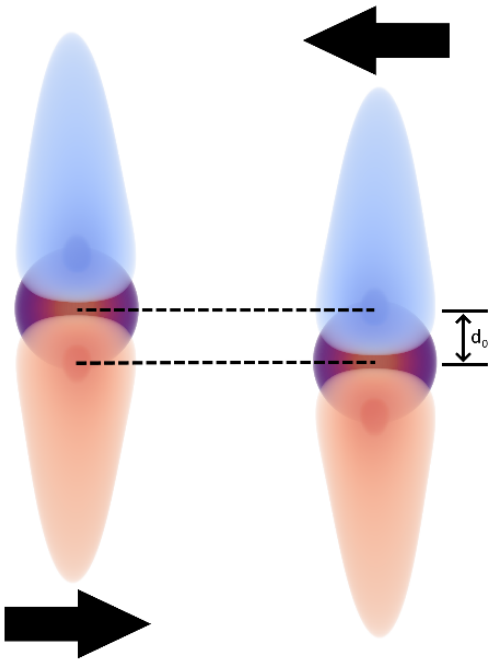

Figure 5.3.1: Scheme of the modified electron-bunch collision configuration. Purple and yellow spheres are the electron density of each bunch, E_y-component of the electron bunch are illustrated in red-blue colour scheme. Arrows indicate propagation direction direction of the respective bunches. Dashed lines are the propagation axis of each bunch as they intersect with the maximum (densest part of field) of the counter-propagating field. Source: [125] ©2021 Kvantovaya Elektronika and IOP Publishing Limited. Reproduced with permission. All rights reserved.

strength of the electric field, which has axial symmetry and possesses a maximum at some distance from the centre of the bunch (see Eq 5.3.1). The maximum value of χ is 1695 in both configurations, which confirms reaching of the fully nonperturbative QED regime. An estimate shows that in an undisplaced configuration, about 34% of the bunch electrons reach this regime. This value is in agreement with the estimate obtained by Yakimenko et al. [38] where they achieved 38%. For comparison, the fraction of electrons reaching the supercritical regime in the displaced configuration is about 33%. Despite this, in the displaced configuration, the yield of both photons and electron–positron pairs is higher (see below). This spatial distribution of the parameter χ directly affects the QED processes. In particular, Fig. 5.4.1 shows the energy density distributions of the emitted photons in both configurations. Since the probability of photon emission is related to the value of the parameter χ, in the undisplaced configuration the emitted photons are located symmetrically around the bunch propagation axis and are almost absent in a small channel along the x-axis. In the displaced configuration, the photons are located

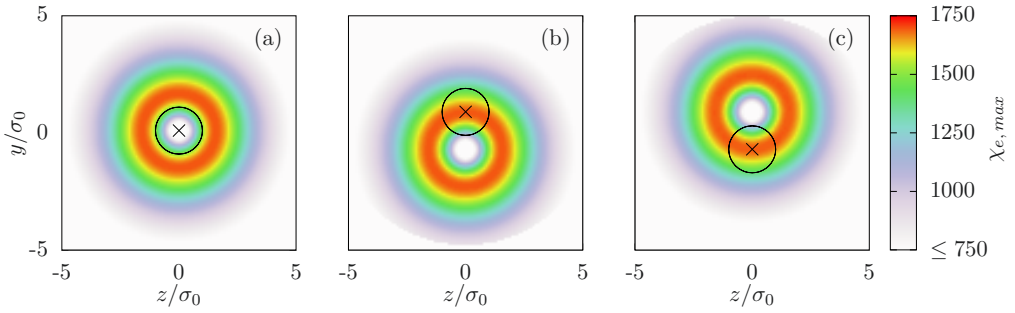

Figure 5.3.2: $\chi_{\max}$ of each cell at time of full overlap in yz-plane. Subplot(a) show the cross-section of undisplaced configuration, (b) and (c) show the displaced configuration and the bunch moving in positive x-direction and in negative x-direction, respectively. Black circle in subplot (b) and (c) have a radius of σ_r and the cross is the bunch center. Source: [125]

near the axes of propagation of both bunches because the centres of the bunches lie in the region of the maximum electric field. Before further analysis of the simulation results, estimates of the secondary particle yield are obtained from [123]. It shows that the ratio of the total number of photons to the initial number of electrons in the bunch can be expressed in terms of the average value of the parameter χ, which is analytically calculated for the Gaussian distribution of the bunch concentration as

$$\chi^{\text{av}} = \Upsilon \approx \frac{5}{12}\frac{N_{e_0}\alpha\gamma\lambda_{\text{C}}^2}{\sigma_r\sigma_x}, \tag{5.4.1}$$

where N_{e_0} is the initial number of electrons in the bunch. With the chosen interaction parameters and a bunch charge of 0.14nC, the parameter Υ is equal to 990. The average value χ^{av} of the parameter χ, calculated from the results of numerical simulation, is ~ 790 in the undisplaced configuration and ~ 787 in the displaced configuration at the moment of the complete overlapping of the bunches. Since the parameter χ^{av} is determined by the field of each bunch, its values are close in both configurations. In the limit $\Upsilon \gg 1$, the ratio of the number of photons to the initial number of electrons in the bunch can be estimated as

$$\frac{N_\gamma}{N_{e_0}} \approx 2.57\left(\frac{\sigma_x}{\gamma\lambda_{\text{C}}}\alpha\Upsilon^{2/3}\right). \tag{5.4.2}$$

Substitution of the value of the parameter Υ into this formula gives the ratio $N_\gamma/N_{e_0} \gg 0.193$, which is in good agreement with the simulation results, according to which this

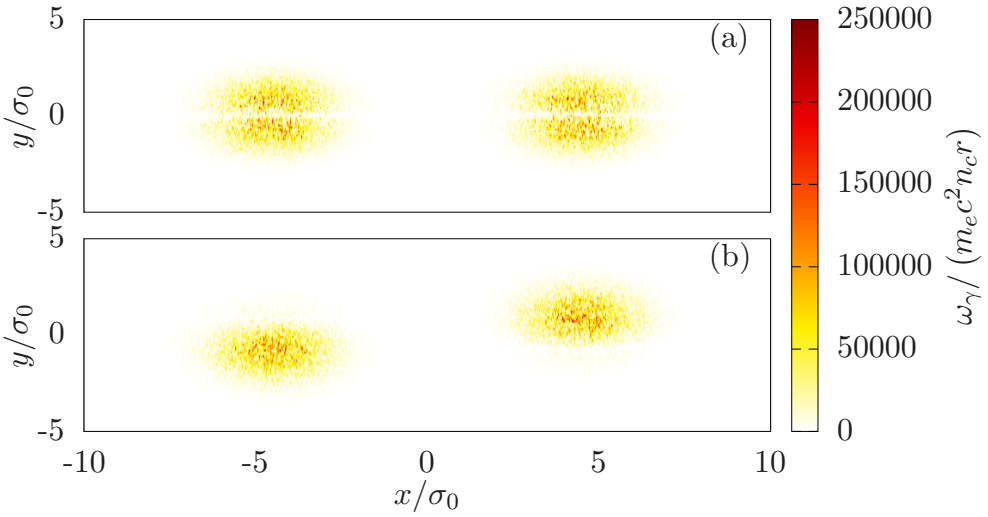

Figure 5.4.1: Photon energy density per cell in *xy*-plane after interaction. Subplot (a) shows the initial configuration and subplot (b) the modified configuration. Source: [125] ©2021 Kvantovaya Elektronika and IOP Publishing Limited. Reproduced with permission. All rights reserved.

ratio is ~ 0.203 for the undisplaced configuration and ~ 0.210 for the displaced one. It is also possible to estimate the energy losses ε_e, which are directly related to the emission of photons by electrons [123]:

$$\frac{\Delta\varepsilon_e}{\varepsilon_e} \approx -0.689 \left(\frac{\sigma_x}{\gamma\lambda_C} \alpha \Upsilon^{2/3} \right). \tag{5.4.3}$$

According to this estimate, the energy loss is $\Delta\varepsilon_e/\varepsilon_e \approx 5.18\%$ for the parameters used in the numerical simulation. This estimate also agrees well with the results of numerical simulations, in which $\Delta\varepsilon_e/\varepsilon_e \approx 5.01\%$ in the undisplaced configuration and $\sim 5.14\%$ in the displaced configuration.

Similar estimates can be made for another QED process under consideration, namely, the production of electron-positron pairs from photons emitted by electrons. In Ref. [124], the ratio of the number of produced electron-positron pairs to the initial number of electrons in the bunch is estimated as

$$\frac{N_{\text{pairs}}}{N_{e_0}} \approx \frac{10.4\sqrt{3}}{25\pi} \left(\frac{\sigma_x}{\gamma\lambda_C} \alpha \Upsilon^{2/3} \right)^2 \ln \Upsilon \tag{5.4.4}$$

for $\Upsilon \gg 1$. For the simulation parameters, this estimate gives the ratio $N_{\text{pairs}}/N_{e_0} \approx 0.0089$, which is in good agreement with the results of numerical simulations, according

to which $N_{\text{pairs}}/N_{e_0} \approx 0.0084$ in the undisplaced configuration and ~ 0.0087 in the displaced one.

5.4.1 Impact of increased bunch lengths on electron bunch colliders

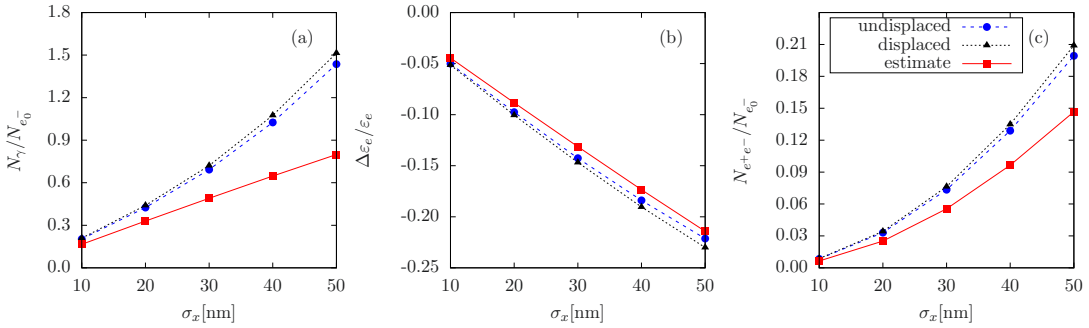

Figure 5.4.2: Fraction of quantities between secondary particles and initial number of electrons compared to literature [123] estimates (red line) acquired by equations 5.4.2 - 5.4.4. Subplot (a) emitted photons per initial electron number, (b) is the energy loss by electrons and (c) is the number of protons to initial electron number. Source: [125] ©2021 Kvantovaya Elektronika and IOP Publishing Limited. Reproduced with permission. All rights reserved.

Concluding with the initial comparison between the displaced and undisplaced configuration, the study now shifts to the effect of the bunch length on the applicability of analytical estimates. To this end, a series of numerical simulations is carried out for the bunch length varying with a step of 10nm. In this case, the maximum concentration of electrons and bunch size σ_r were the same as in the simulation described above. Figure 5.4.2(a) shows the ratios of the number of photons to the initial number of electrons in the bunch, obtained as a result of numerical simulation and using analytical estimate 5.4.2 under the assumption that $\chi^{\text{av}} \approx \Upsilon$. It can be seen that in both configurations the photon yield increases with increasing bunch length, and hence the bunch interaction time. The energy losses and the yield of electron–positron pairs shown in Figs 5.4.2 (b) and (c), respectively, reflect the same regularity. The simulation results show that the simultaneous displacement of the bunch centres and increase in their length generally increase the yield of secondary particles. Thus, in the displaced configuration for bunches with a length of 10nm, the photon yield increases by $\sim 3.3\%$, and the yield of electron-positron pairs by $\sim 4.4\%$ compared to the undisplaced configuration, while

for bunches with a length of 50nm, the increase is $\sim 5.4\%$ for photons and $\sim 4.9\%$ for pairs. It should be noted that the simulation results and analytical estimates are in good agreement for short bunches, but slightly differ for longer bunches. It can be seen from Fig. 5.4.2 that, although analytical estimates still give the correct order of magnitude for bunches with a length greater than 30nm, the predicted functional dependence is somewhat different from that observed in the simulation. This is partly explained by the fact that with increasing bunch lengths the transverse dynamics of particles becomes important.

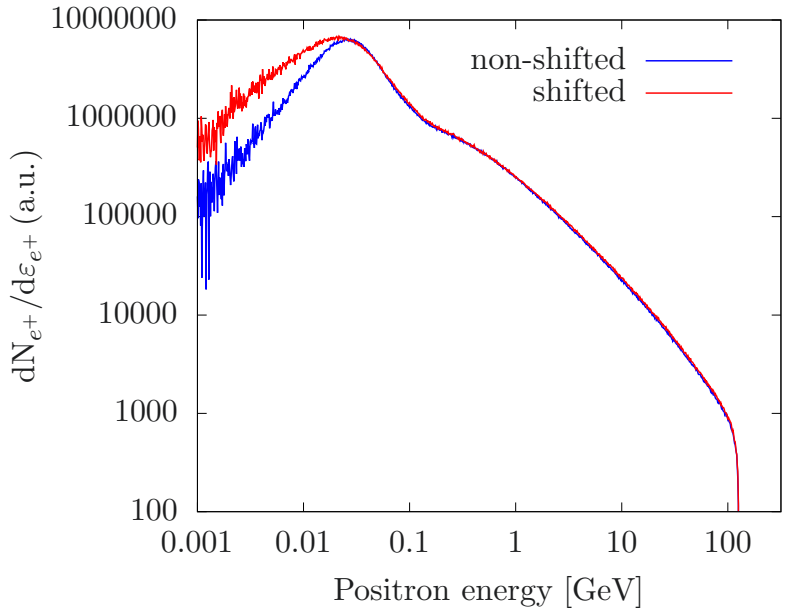

Figure 5.4.3: Spectrum of all positrons at the end of the simulation for electron bunches with a bunch length of 50nm. Axes are logarithmic. Source: [125] ©2021 Kvantovaya Elektronika and IOP Publishing Limited. Reproduced with permission. All rights reserved.

The average values of the transverse momentum of the initial electrons after a complete crossing of the bunches are presented in table 5.4.1, from which follows the direct dependence of this quantity on the bunch length. With an increase in the transverse momentum of the bunch particles, the change in the charge distribution in the bunch becomes more significant, which in turn leads to a change in the distribution of the electromagnetic field. This causes the discrepancy between the analytical estimates, which were obtained under the assumption that the field distribution remains unchanged, with the results of modelling the collision of extended bunches. An influence of transverse particle dynamics on collisions of bunches is studied in detail in Ref. [68].

In addition, the displacement of the propagation axis exhibits a difference on the energy

Bunch length σ_x/nm	$1000 p_\perp^{\mathrm{av}}/p_0$	
	undisplaced configuration	displaced configuration
10	0.69	0.72
20	1.36	1.39
30	1.97	2.02
40	2.51	2.59
50	2.97	3.10

Table 5.4.1: Average transverse momentum $p_\perp^{\mathrm{av}}$ of initial electrons after interaction in simulations with different bunch lengths. Here, p_0 is the intial momentum. Source: [125]

of secondary particles. Figure 5.4.3 shows the energy spectrum of positrons in both configurations for bunches with a length of $\sigma_x = 50$nm. One can see that the displaced configuration contains a greater number of low-energy positrons than the undisplaced one.

For the sake of completeness, it should be mentioned that disruption of bunches was studied in the work of Samsonosov *et al.* in [134]. Here, an analytical solution of the equation of motion was derived which also included radiation reaction. The model shows that the bunch radius and the quantum non-linearity parameter are of importance in the focusing or disruption of the bunches.

5.5 Conclusion

Thus, an improvement in the configuration by the previously proposed work [38], aimed at increasing the yield of particles, while remaining in the nonperturbative QED regime, has been suggested. Collisions with electron bunches, shifted across their axes so that the maximum density of one bunch passed through the maximum of the field of the counter-propagating bunch, have been considered. It was shown that in this configuration, a higher yield of both photons and electron-positron pairs compared to the collision of non-shifted bunches was observed. The study was carried out using three-dimensional modelling with the particle-in-cell method.

A comparison of the results obtained with previous works, which provided analytical estimates of the particle yield, shows that the data and the estimates are in good agreement

with the results of numerical simulations in the case of short bunches. However, they start to differ from the simulation results in the collision of long bunches, when the transverse dynamics of particles becomes essential.

This modification could be considered in experiments once particle accelerators are able to achieve similar particle bunch parameters. Also, the modified configuration and the initial proposal for the collider could finally be able to access the currently unexplored QED regime and establish a theory on light-matter interactions at these very strong fields. Whether or not the modification helps understand this regime, it is of great interest to observe the radiation losses in a non-perfect head-on collision.

Contribution of the author: The chapter contains the results and discussion of the publication [125]. C.B. conceived the configuration and M.F. carried out all simulations and performed data analysis. M.F. wrote the code for the data analysis. C.B., M.F., A.P. and I.K. clarified details of the physics. The first draft was written by M.F. and all author commented on it. Translating the manuscript into Russian was done by A.S.

6 Study of QED effects at grazing incidence on solid-state targets

So far, the thesis focused on using high-energy electron bunches produced in conventional accelerators to study QED effects. In the following chapter, the focus now lies to using near-future lasers with peak intensities of $> 10^{24}$W cm^{-2} to extract electrons from a target and accelerate them. Using such lasers would provide high-energy electrons and strong-fields to trigger QED effects as the perceived field by the electrons is then greater than the Schwinger limit. The configurations uses two high-energy lasers, which propagate towards a solid-state target. The lasers are aimed at the target at a grazing angle, nearly propagating parallel to the target. Furthermore, these lasers are propagating along the surface and approach symmetrically from two sides. Two-dimensional particle-in-cell simulations are performed in this study. Accelerated electrons and lasers interact with each other, fueling QED process. A minimum laser intensity of $\sim 10^{24}$W cm^{-2} is necessary to trigger pair production process and an even higher intensity to maintain the production of an electron-positron plasma. This plasma is created due to the repeated processes of photon emission and pair production.

Finally, it is shown, that using the solid-state target is beneficial in comparison of an imperfect vacuum, where remnants of electrons remain. Ionizing the vacuum is difficult, as more generations of QED effects are necessary to create an electron-positron plasma. Using the solid-state target as source of electrons is more advantageous, even though the acceleration path within an imperfect vacuum is unobstructed and allows for higher electron energies to be achieved.

The results and content of this chapter are reused and adapted from the *QED effects at grazing incidence on solid-state targets* by Filipovic, M. and Pukhov, A. (2022), The European Physical Journal D, 76(10), 187. In detail, sections 6.1 and 6.3 are reused and slightly modified from the aforementioned work [135]. Additionally, sections 6.4, 6.5 and 6.6 are reused from above mentioned work [135].

6.1 Introduction

Until now, QED effect have been studied with high-energy electron bunches, but with lasers that have an intensity of $> 10^{23}$W cm^{-2}, probing QED theory is attainable with these lasers as well. A high quantum parameter χ requires that the particles interact with a strong field, which was previously obtained by a counter-propagating beam and its field.

Future lasers-facilities will be able to provide the necessary parameter of $\chi \gg 1$ to witness relativistic particles and observe QED effects within promising configurations. Configurations using laser on near-critical plasma [136–139] or thin foils [140] have been previously proposed.

This chapter focuses on the interaction of high-intensity lasers at grazing incidence to study QED effects and QED cascades on a solid density target. Utilizing a laser to scrape the surface of a solid-state target, by approaching the target under a grazing incidence allows to extract and accelerate electrons. The counter-propagating laser also generates similar electrons but is primarily essential to overcome the Schwinger limit for the electrons accelerated by the other laser in their rest frame.
Consequently, the proposed configuration uses two high-intensity lasers that intersect on the target's surface. Employing a small grazing incidence for the lasers achieves a higher Lorentz-factor for the extracted particles and a greater current of the extracted electron bunch [141]. The extracted electrons can then interact with the field of the counter-propagating laser beam.

6.2 Acceleration of particles near surface

Before examining the simulation results a more in-depth look on the acceleration process is necessary. Here, only a brief explanation of the process is given. The content of this section summarizes the analysis of [141], where a more extensive discussion can be found. For now, it is considered that a p-polarized wave propagates at a grazing incidence towards a reflective surface. This surface would reflect a wave fully. The coordinate system places the x-axis parallel to the surface and z-axis normal to the polarization plane. The superposition of the incident and reflected fields is then

$$E_x = 2E_0 \sin\Theta \sin(ky \sin\Theta) \sin(kx \sin\Theta - \omega t + \phi_0), \tag{6.2.1}$$

$$E_y = 2E_0 \cos\Theta \cos(ky \sin\Theta) \cos(kx \cos\Theta - \omega t + \phi_0), \tag{6.2.2}$$

$$B_z = 2E_0 \cos(ky \sin\Theta) \cos(kx \cos\Theta - \omega t + \phi_0) \tag{6.2.3}$$

with E_0 the amplitude of the field, Θ the grazing angle, k the vacuum wavenumber, ω the angular frequency of the wave and ϕ_0 the initial phase [141]. Even though the incident and reflected fields are propagating under an angle, the superposition of those is a wave traveling along x with $v_{ph} = c/cos\Theta$ phase velocity of, and $\lambda_0 = \lambda/\cos\Theta$ denoting the wavelength [141].

Placing an electron in this field at $y = \lambda/(4\sin\Theta)$ at an initial time $t = 0$ and it is assumed that no transverse instability occurs the resulting transverse fields E_y and B_z are zero. Only the E_x component is non-zero. This field can accelerate an electron to relativistic energies if the amplitude is sufficiently high. How long a particle remains in the acceleration fields though depends on the initial phase and the incident angle [141].

With these information one can determine the phase displacement of the electron. Since the phase velocity of the wave is higher than the electron speed v_e the particle will only remain a certain number of periods N in the field. The phase displacement is then

$$\Delta\phi = 2\pi\frac{L_{wave} - L_e}{\lambda_0} \approx \frac{2\pi}{\lambda_0}\left(\frac{c}{\cos\Theta} - c\right)NT \tag{6.2.4}$$

where $L_{\text{wave}} = cNT/\cos\Theta$ is the distance the wave travels and $L_e \approx cNT$ is the distance an electron travels within the wave are [141]. Using this the number of field periods that an electron can remain at max in which it gets accelerated can be derived

$$N_{acc}(\Theta) = \frac{1}{2(1-\cos\Theta)} \tag{6.2.5}$$

and demonstrates that a small grazing angle is favourable [141]. Finally, with the maximum number of periods an electron can be accelerated, the attainable Lorentz-factor of the electron can be found as

$$\gamma_{\max} = 1 + \frac{|e|\overline{E_x}N_{acc}\lambda}{mc^2} \approx 1 + \frac{4|e|E_0N_{acc}\lambda\sin\Theta}{\pi mc^2} \approx 1 + \frac{4a_0\sin\Theta}{1-\cos\Theta} \tag{6.2.6}$$

with $\overline{E_x} \approx 4E_0\sin\Theta/\pi$ being the average over time of the E_x-component, m denoting the electron mass and e the electron charge [141].

6.3 Prediction on QED cascade occurrence

In this field, photon emission and pair production may continue repetitively and lead to QED cascades [72, 93, 142–147]. Here, an electron-positron plasma of high density builds up at the surface of the target. This happens, due to electrons and positrons

oscillating in the strong electromagnetic fields and emitting photons, while the new photons decay again to an electron-positron plasma. The new particle then have the possibility to repeat the cycle, if sufficient energy remains in the system.

In the work of Grismayer et al. [93] configurations maximizing the pair growth in QED cascades were studied. For this reason setups that provide the highest values of the quantum-parameter are likely to produce a cascade. The quantum-parameter as described in eq. 2.4.1 increases with greater γ-values. Taking a look now at laser beams at grazing incidence, which are used here, eq. 6.2.6 demonstrates lowering Θ gains higher γ-values. An estimation with eq. 6.2.6 gives a $\gamma_{\max}$ of $\sim 1.2 \times 10^4$ for $\Theta = 15^\circ$ and $a_0 = 400$ if the particle remains in the maximum number of field periods, where it can be accelerated [141]. These high-energy electrons support the cascade when considering the probability rates of photon emission and pair production.

Simple asymptotic expression in the limit of large χ_e for electrons and χ_γ were provided in [72] and previously mentioned in section 2.4 reading

$$W_{\text{rad}} \approx 1.46 \frac{\alpha m^2 c^4}{\hbar \varepsilon_e} \chi_e^{2/3} \tag{6.3.1}$$

and

$$W_{\text{pairs}} \approx 0.38 \frac{\alpha m^2 c^4}{\hbar \varepsilon_\gamma} \chi_\gamma^{2/3} \tag{6.3.2}$$

with W_{rad} the probability rate for photon emission, W_{pair} the probability rate for pair creation by hard photons and ε as the energy of the appropriate particle. Here, it can be seen that electrons with a high χ are more likely to emit photons and high-energy γ-photons decay easier to electron-positron pairs since the probabilities increase with higher χ. In the proposed configuration the second counter-propagating laser beam, respectively for both sides, supplies a strong electromagnetic field to increase the χ-parameter. Therefore, multiple generations of QED processes can occur, which leads to cascading.

6.4 Simulation setup

The particle-in-cell (PIC) simulations are performed in a two-dimensional (2D) geometry using the Virtual Laser Plasma Lab (`VLPL`) code [45, 57]. The simulation domain is $100\lambda_0$ and $50\lambda_0$ in x and y direction ($\lambda_0 = 910$nm is the laser wavelength) with a spatial grid step of $0.02\lambda_0 \times 0.05\lambda_0$, respectively. The electromagnetic fields are updated with

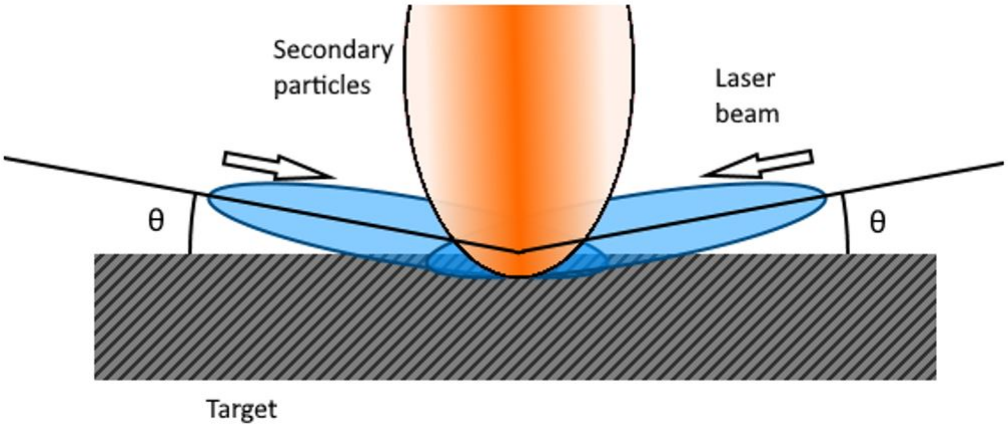

Figure 6.4.1: Configuration of two high-intensity lasers grazing a solid-state target. Arrows indicates the trajectory of each laser beam. The lasers are focused on the centre of the upper edge of the target. Both lasers are incident on the same angle Θ. The orange half ellipsis shows the region where secondary particles from QED effects will be located after the interaction. *Source: [135], licensed under CC BY 4.0* (https://creativecommons.org/licenses/by/4.0/).

the X-dispersionless Maxwell solver [77], also known as RIP-solver. The Maxwell-solver requires $h_x = c\tau = 0.02\lambda_0$ with h_x the longitudinal grid step and τ the time step. A simulation runs for $120T_0$ with $T_0 \approx 3.04$fs being the laser period. The basic configuration is shown in Fig. 6.4.1. The solid-state-target is located in the lower half of the simulation domain. The electron density is $505.55n_{cr}$. Here, $n_{cr} \sim 1.35 \times 10^{21}\text{cm}^{-3}$ is the critical density for the considered wavelength λ_0. Absorbing boundary conditions were chosen for the domain. The electrons are represented by four particles per cell.

Both lasers are linearly p-polarized Gaussian beams with

$$a = a_0 \exp\left(-\frac{(x-ct)^2}{\tau^2} - \frac{y^2}{\sigma_y^2}\right) \tag{6.4.1}$$

with $\tau = 8.240T_0$ and $\sigma_y = 5.978\lambda_0$. The two lasers are scraping the target at grazing angle in the range $2.5^\circ \geq \Theta \geq 15^\circ$ ($1/72\pi \geq \Theta \geq 1/12\pi$) and are initialized $75\lambda_0$ away from their point of incidence. Point of incidence of both laser propagation axes is at the centre of the upper edge of the target.

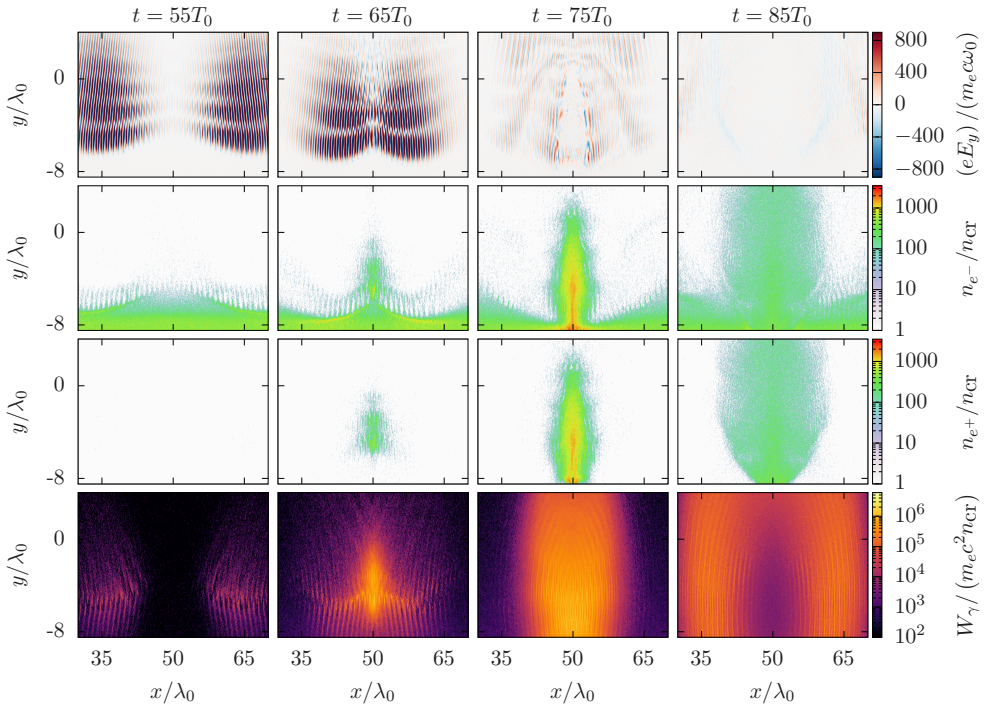

Figure 6.5.1: E_y-component in dimensionless units (first row), electron density distribution in critical densities (second row), positron density in critical densities (third row), and energy density of emitted photons (fourth row) at different time instances in QED-PIC simulation with parameters $a_0 = 1200$ and $\theta = 15°$. *Source: [135], licensed under CC BY 4.0* (https://creativecommons.org/licenses/by/4.0/).

6.5 Results

The first simulation presented uses lasers with an incident angle of $\Theta = 15°$ and an $a_0 = 1200$. After the initialization, the lasers propagate along the surface extracting, capturing and accelerating electrons in the electromagnetic fields of the lasers (see Fig. 6.5.1 first row). These electrons co-move with the laser along the surface (see figure 6.5.1 second row $t = 55T_0$). In the process the particles of the target emit photons, which can be seen in Fig. 6.5.1 (fourth row). The energy density of the emitted photons is similarly structured to the propagating electromagnetic waves since the probability rate of the process is tied to the χ-parameter, which includes the electromagnetic fields.

The trapped electrons and emitted photons produced by one laser beam collide with the counter-propagating laser beam and particles. In the interaction region, where both laser beams overlap, the non-linear Breit-Wheeler pair production becomes likely. At this point the χ-parameter rises to a value of 9.65 due to the strong field that a particle comes

in contact within its rest frame. Photons decay in an electron-positron pair, which is represented by Fig. 6.5.1 (third row) during the overlap (middle column) at $t = 75T_0$. An electron-positron plasma builds up in the region and expands outwards in the positive y-direction, where the target is not obstructing fields and particle dynamics, while reaching a higher peak density than the initial solid-state target. Recording of pair production processes start once the counter-propagating beam reaches the centre, since the fields near the surface are not sufficient to trigger the effect with the co-moving photons. In addition to the emitted photons by grazing the target, the collision of the extracted electrons and the counter-propagating laser triggers photon emission again, which fuels the electron-positron plasma. Once the field is partially absorbed by the electron-positron plasma, the new plasma is shielded by the remaining electromagnetic field (see Fig. 6.5.1 first row) at $t = 85T_0$. Several cycles of the emission of hard photons and the conversion of electron-positron pairs are observed leading to the electron-positron plasma by this QED cascade.

Figure 6.5.2 shows the spectra of electrons, positrons and γ-photons at four different time instances. At $t = 55T_0$ the energy spectra after extracting and accelerating some electrons by the incident laser beams are shown. Electrons, represented in subplot (a), are accelerated up to 3GeV. Pair production at the early stage without interacting with the counter-propagating electromagnetic field (see subplot c) occurs only in a low number. Here, it can be seen, that the positron spectrum at $t = 55T_0$ only shows some noise in the low energy region by a low number of pair production processes. This observation is in agreement with the rise of the electron-positron plasma shown earlier in Fig. 6.5.1.

Continuing with the photon emission, γ-photons are emitted at two points in the configuration. First, photon emission takes place once the laser beam comes into contact with the target and then continuously emits photons while scraping the surface, which can be seen in the energy densities of Fig. 6.5.1 (fourth row). The corresponding spectra to the displayed energy densities are shown in Fig. 6.5.2 (b). At $t = 55T_0$ the continuous photon spectrum contains mainly low-energy photons. Second, the accelerated and extracted electrons collide with the counter-propagating beam and radiate high-energy photons due to the stronger electromagnetic field perceived in the electrons rest frame. The photon spectrum at $t = 65T_0$ gains, in comparison to the previous time, photons across the whole recorded energy range, as the front of the counter-propagating laser reaches the point, where the propagation axes of both laser beams intersect at the surface (see Fig. 2 at $t = 65T_0$). In the time instance $t = 75T_0$ and forward the number of photons increases by several orders of magnitudes. The radiation-reaction is now significantly stronger leading to the great yield of emitted γ-photons. Additionally, the maximum energy of the γ-photons slightly decreases between the times $t = 65T_0$ and $t = 75T_0$. The reason for

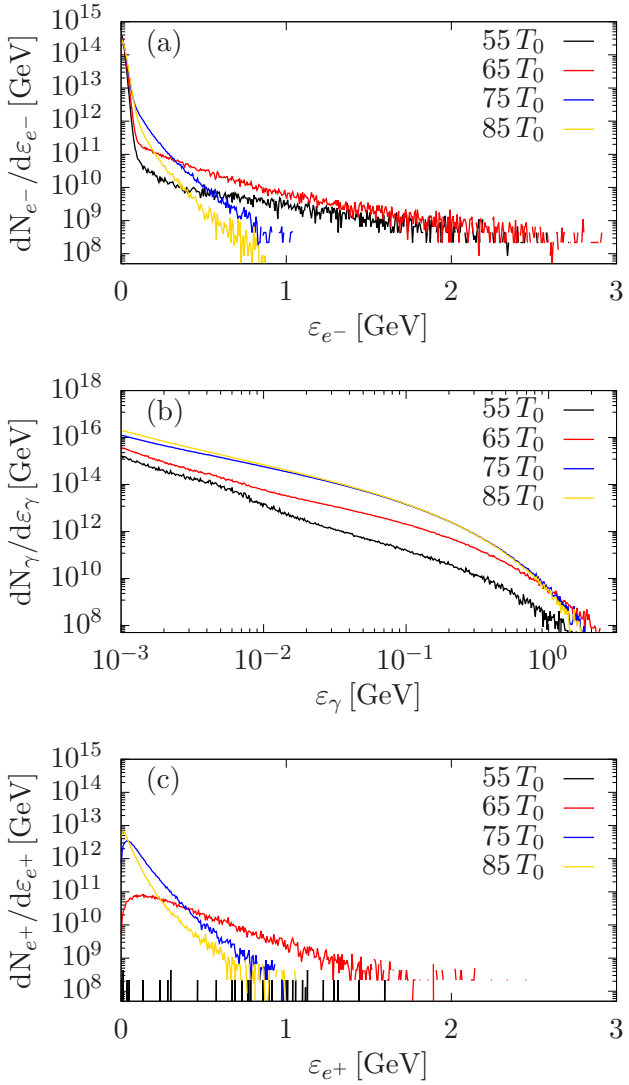

Figure 6.5.2: Particle spectrum of electrons (a), photons (b) and positrons (c) at $t = 55T_0, 65T_0, 75T_0$ and $85T_0$. The highest peak of the laser beam reaches the centre of the surface at $t = 75T_0$. Laser parameters are $a_0 = 1200$ and angle of incidence is $\Theta = 15°$. *Source: [135], licensed under CC BY 4.0* (https://creativecommons.org/licenses/by/4.0/).

this change is the high probability of high-energy photons undergoing the pair-production process.

As the electron beam interacts with the counter-propagating laser beam the number of positrons increases (see Fig. 6.5.2 (c)). This indicates that the probability for pair production processes became more likely and the process is triggered. Both the electron and positron spectrum roughly coincide. With both laser beams starting to overlap the

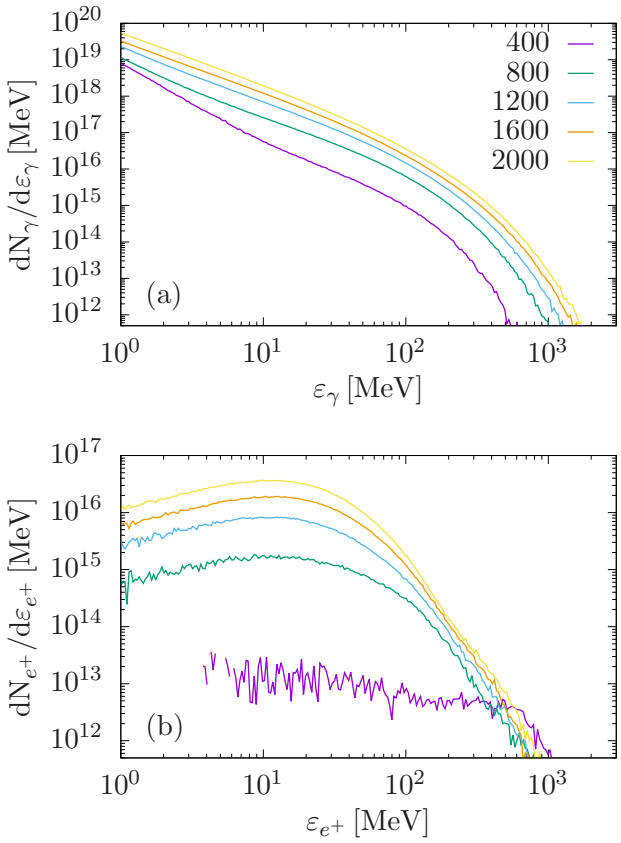

Figure 6.5.3: Double logarithmic spectrum of emitted photons (a), and logarithmic spectrum of positrons (b) after the overlap of the high-intensity lasers for different a_0 pulses. Angle of incidence for both configuration is $\Theta = 15°$. *Source: [135], licensed under CC BY 4.0* (https://creativecommons.org/licenses/by/4.0/).

maximum recorded electron and positron energy drops to $\sim$ 1GeV by $t = 75T_0$. The electrons and positrons lose their energy due to the radiation-reaction with the laser beams. It can be observed as the increase of low-energy electrons and positrons in their respective spectrum. At the same time more γ-photons are emitted that further produce electron-positron pairs. This is shown by the positron spectrum in subplot (c) at $t = 75T_0$.

In a next step, the influence of the laser parameters will be discussed. Figure 6.5.3 shows the photon spectrum and positron spectrum for different laser amplitudes ranging from 400 to 2000. In general, increasing the energy of the laser beam boosts the secondary particle spectra. Additionally, the cutoff energy of the photon drifts to a higher value by increasing a_0. In the special case of $a_0 = 400$ the characteristic spectrum of positrons is not reproduced since the statistic is insufficient and the electromagnetic fields are not strong enough to develop the positron spectrum. Only by reaching an $a_0 \sim 800$ pair

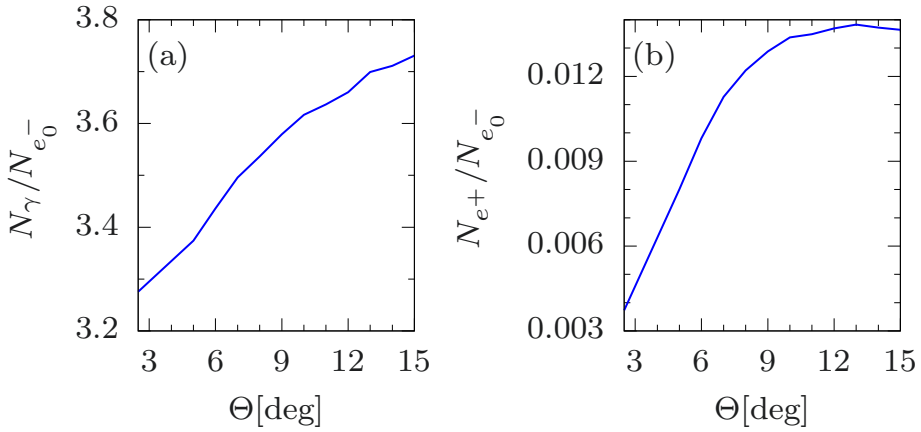

Figure 6.5.4: Ratio of emitted photons to the initial number of electrons (a), ratio of electron-positron pairs to the initial number of electrons (b). a_0 is set to 800. *Source: [135], licensed under CC BY 4.0* (https://creativecommons.org/licenses/by/4.0/).

processes are sufficiently witnessed and an electron-positron plasma builds up.

The other laser parameter in the proposed configuration is the angle of incidence Θ. In a second simulation series the angle has been varied between $2.5 - 15\,[\text{deg}]$ while maintaining the dimensionless vector amplitude at $a_0 = 800$. Figure 6.5.4 shows the ratios for emitted photons (subplot a) and positrons (subplot b) per initial electron. In general, fractions of secondary particles increase with a larger angle Θ. Further, positrons of the pair production per initial electrons are maximized at an angle of $\sim 10°$, whereas photons remain to increase with bigger angles. A possibility for this observation may be the energy loss of the electromagnetic fields. The lasers are absorbed by the electron-positron plasma in the interaction region. When the laser energy is depleted, the pair production ceases and the ratio of positrons per initial electrons is maximized. While this is the case for pair production, photons may still be emitted with a weaker field. Fraction of photons per initial electron continue to rise after an incident angle of 10°.

The previous results showed that QED effects were observed in the proposed configuration. In a final step, the configuration will be compared to a seeded vacuum cascade [92, 142, 148]. Setting up a configuration for a vacuum cascade appears to be simpler, therefore it is reasonable to compare both configurations. A seeded vacuum may resemble an imperfect vacuum, where a small impurity remains after trying to create a vacuum. Seed electrons are necessary to initiate QED effects in the code. Fig. 6.5.5 shows a comparison between the proposed configuration and the seeded vacuum within the secondary particle spectra for lasers with $a_0 = 800$ and $\theta = 12°$. 72 seed electrons are initialized in two cells where the propagation axis of both lasers intersect. The electron

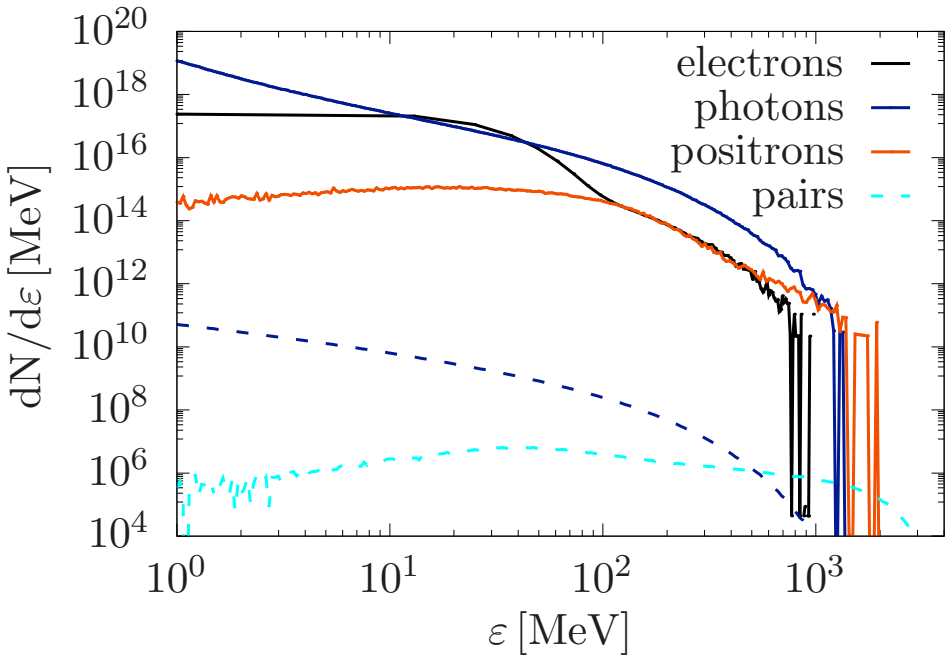

Figure 6.5.5: Double logarithmic spectrum of secondary particles. Solid line represents the configuration of grazing a solid-state target; dashed line is the seeded vacuum configuration. Spectrum after the overlap of the high-intensity lasers at $t = 90T_0$. Angle of incidence for both configuration is $\Theta = 12^\circ$ and $a_0 = 800$. Additionally, the cyan line represents the electron and positron spectrum, since both spectrum are equal due to the small number of seed electrons. *Source: [135], licensed under CC BY 4.0* (https://creativecommons.org/licenses/by/4.0/).

density in those cells is $7.39 \times 10^{-7} n_{cr}$. Here, the solid-state-target emits many order of magnitudes of photons more than the seeded vacuum cascade. While emitting less photons the vacuum cascade manages to accelerate the positrons created by pair production process to an energy of $\sim$ 3GeV seen in the increased cutoff energy. The proposed configuration still outperforms the vacuum scenario in the yield of pairs. However, the maximum photon energy achieved is $\sim$ 1400MeV.

6.6 Conclusion

In this chapter, the interaction of two high-intensity lasers and a solid-state target was studied in the framework of PIC simulations. Focus was placed on QED processes occurring where both lasers overlap and interact with extracted and accelerated electrons. The large number of extracted electrons escalates into a QED cascade, creating an

electron-positron plasma once the laser intensity becomes sufficiently high. A comparison of the plasma with a seeded vacuum cascade demonstrated that using a target outperforms an imperfect vacuum.

Furthermore, increasing the angle of incidence reached an upper limit on the pairs produced by QED effects in the electron-positron plasma and higher lasers intensities showed that a certain laser intensity is necessary to trigger pair production processes.

Additional studies should be performed using different potential target materials and other target shapes to enhance the achieved quantum parameter or increase the number of QED processes.

In the near future, when higher intensities are reached, this configuration may be replicated experimentally and help to achieve even not yet experimentally explored regimes like the fully nonpertubative regime.

Contribution of the author: The chapter contains the results and discussion of the publication [135]. A.P. conceived the configuration and M.F. carried out all simulations and performed data analysis. M.F. and A.P. clarified details of the physics. The first draft of the manuscript was written by M.F. and A.P. commented on it.

7 Conclusion

This thesis on the investigation of QED effects in strong-field interactions introduced numerical tools and configurations to prepare key experiments that will test QED in the near future. The study has focused on four key areas: merging algorithms in numerical particle-in-cell code simulations, mitigation of errors occurring in numerical simulations of ultrarelativistic particles, optimization of particle yield in the non-perturbative regime of QED, and the interaction of high-intensity lasers with solid-state targets.

Chapter 2 described the necessary theory behind plasmas, lasers and QED effects essential to the topic of the thesis and was followed by a short summary of the numerical techniques in chapter 3. This was necessary, since all simulation results have been obtained with the particle-in-cell code `VLPL`. Special focus was laid on the QED module in section 3.4, as the majority of the results included QED events. To improve the PIC code, new merging methods have been implemented. They are needed to compensate the increased load by the vast secondary particle production and are described in section 3.5. The merger module was then thoroughly benchmarked in section 3.5.4.

In the first part of the study, presented in chapter 4, the vacuum propagation of ultra-relativistic electron bunches was examined within the framework of particle-in-cell simulations. The central research question concerned the changes in bunch dynamics when different Maxwell solvers were used and the energy losses the electrons underwent. The results showed that the standard Yee solver encountered significant issues with numerical instabilities, leading to non-physical energy losses. Conversely, the X-dispersionless Maxwell solver (RIP solver) demonstrated excellent performance, maintaining the electron bunch's density profile and avoiding numerical problems, thus proving to be an ideal choice for high-energy physics simulations.
The source of the major instability was located within the numerical Cherenkov instability by identifying excited modes in the dispersion relation.
Afterwards, radiation reaction was considered in the simulation which increased non-physical radiation losses in the Yee simulation. Again, the density distribution was not maintained, but the electron bunch lost the majority of its initial energy. Tracking individual particles here showed that the particles interacted with a strong force and were

propagated outwards from the electron bunch. On the other hand, the simulation with the RIP solver sustained its distribution and exhibited minuscule energy losses. Comparing the E_y-component an excited mode was visible in the Yee simulations, but missing in the RIP solver. For future advancements, improving Maxwell stencils in PIC-code may reduce instabilities in numerical simulations. New Maxwell solver must again undergo similar benchmarks in that regard to be reliable in PIC simulations. Other improvements should be considered too, as particle pushers are also a source of introducing numerical instabilities.

Establishing that the RIP Maxwell solver for particle propagation in one direction is a suitable option, chapter 5 of the thesis proposed an adjustment to a previous work with the aim of achieving higher particle yields while reaching the fully non-perturbative regime of QED. Here, the fully nonperturbative regime of QED and its interest of study were described, as it is currently not experimentally observed. The configuration uses two ultra-relativistic electron bunches propagating towards each other. Since an electron bunch interacts with a strong electromagnetic field it was deduced that it would be sufficient to reach the new regime. The thesis introduced a shift of the propagation axis in order to interact the maximum electron density of one bunch with the maximum of the counter-propagating electromagnetic field generated by the respective other electron bunch. The main finding was that a transverse displacement of the bunch propagation axes in bunch-bunch collisions led to higher photon emission and pair production. This adjustment was supported by 3D PIC simulations and a comparison with previous literature, which agreed with the data. A slightly smaller amount of particles would reach the new regime, but the configuration would produce more secondary particles. Data and literature estimates were in a good agreement but had limitations with longer bunches. An additional phenomenon, which was observed, was the pinching of the bunches with increased bunch lengths. This phenomena should be studied further in its impact on secondary particle generation and reaching the fully non-perturbative QED regime.

Chapter 6 as the final part of the study, continued the study for possible configurations to understand QED effects further. Here, the interaction between two high-intensity lasers and a solid-state target was investigated using two-dimensional PIC simulations. The emphasis was placed on QED processes occurring in regions where both lasers converge and interfere with electrons that have been extracted and accelerated. Due to the accelerated electron interacting with a strong counter-propagating laser beam the quantum non-linearity parameter is high. This lead the particles to undergo QED processes. It has been determined that extracted electrons initiated multiple generations of QED processes, developing a plasma comprised of electrons and positrons. It was possible once the laser intensity reached $\sim 10^{24}\mathrm{W\ cm^{-2}}$. During such a numerical

experiment, the electrons would gain energy as the laser beam begins to scrape the surface of the target. After the interaction with the counter-propagating beam, most extracted electrons would lose their energy by emitting photons. The new photons would finally decay into an electron-positron pair. Theses processes repeat, leading to the mentioned QED cascade.
The study also analyzed the impact of different incidence angles of the lasers as well as different laser intensities. The former showed that by increasing the angle the secondary particle production by QED events would increase until a limit is finally reached. As for the latter simulation series, increasing the laser intensity allows more secondary particles to fuel the buildup of the electron-positron plasma. Finally, it was discovered that employing a target is more effective than using an imperfect vacuum, as the target supplies initial electrons for QED processes. This configuration should be further studied by shifting the incidence point of the lasers or using different materials. By doing this, the configuration can be further optimized until laser facilities are finally able to reach the necessary intensities and perform the experiments.

Questions discussed in this thesis are important for the field of high-energy physics, particularly in the development and optimization of particle acceleration and exploring QED. These configurations could not only help to validate predictions and models developed in this research but also uncover new phenomena and insights that can further advance the understanding of QED and high-energy physics. However, the study also has limitations, such as the need for further research into various target materials and shapes to maximize the quantum nonlinearity parameter and boost the quantity of QED processes. Future research is required to explore QED theory in leading facilities with appropriate experiments.
In addition to the immediate applications to study QED, the problems of this thesis are relevant for other related fields, such as astrophysics and nuclear physics. For instance, the study of QED processes in high-intensity laser-plasma interactions can provide valuable information on the behaviour of matter and radiation under extreme conditions, which are important to understand astrophysical phenomena such as gammma-ray bursts and neutron star mergers.

Acknowledgements

Here, I would like to thank you on all the people who have supported me throughout my time working on the thesis.

First, I would like to give my thanks to Professor Dr. Alexander Pukhov for giving me the opportunity to work in his research group and supporting me on the various research I performed. I am grateful for gaining new insights and valuable experiences in the vast tasks I have done during my time in his group.

I would like to also thank Professor Dr. Dr. Carsten Müller for being the second reviewer and encouraging and giving me advice on presentations in exercise groups.

My thanks also goes to Frau Ute Birkenkamp-Pickshaus who helped me with various bureaucracy as well as when times got difficult due to a lot of things.

I am also grateful to Eugen Braun who helped me multiple times with the mess I did on my office work station PC and things not running on the servers, because of me testing out things.

A big thank you also goes towards Dr. Christoph Baumann, who helped me settle in in the beginning, had helpful discussions, proofread my manuscripts and helped me on a lot problems I stumbled across my time here. Thank you to Dr. Lars Reichwein for helping me with students, proofreading the thesis and giving great advice for manuscripts.

I would like to thank you the Heinrich-Heine University Düsseldorf in regard of the payment of publication charges.

Finally, I would like to thank my parents Elizabeta Filipovic and Ljubisa Filipovic for always having my back; and Kevin Hungenberg for supporting me throughout the university time as a great friend.

Eidesstattliche Erklärung

Ich versichere an Eides Statt, dass die Dissertation von mir selbständig und ohne unzulässige fremde Hilfe unter Beachtung der „Grundsätze zur Sicherung guter wissenschaftlicher Praxis an der Heinrich-Heine-Universität Düsseldorf“ erstellt worden ist. Die Arbeit wurde bislang nicht in deutscher oder in einer anderen Sprache veröffentlicht.

Düsseldorf, den

Unterschrift

Bibliography

[1] Albert Einstein, "Strahlungs-Emission und Absorption nach der Quantentheorie," Deutsche Physikalische Gesellschaft **18**, 318–323 (1916).

[2] Theodore H Maiman *et al.*, *Stimulated optical radiation in ruby* (Elsevier, 1960).

[3] A. Ashkin, J. M. Dziedzic, and T. Yamane, "Optical trapping and manipulation of single cells using infrared laser beams," Nature **330**, 769–771 (1987).

[4] L. M. Barker and R. E. Hollenbach, "Laser interferometer for measuring high velocities of any reflecting surface," Journal of Applied Physics **43**, 4669–4675 (2003), https://pubs.aip.org/aip/jap/article-pdf/43/11/4669/7948385/4669_1_online.pdf .

[5] Donna Strickland and Gerard Mourou, "Compression of amplified chirped optical pulses," Optics Communications **55**, 447–449 (1985).

[6] *Whitebook ELI - Extreme Light Infrastructure: Science and Technology with Ultra-Intense Lasers* (2011).

[7] Wenqi Li, Zebiao Gan, Lianghong Yu, Cheng Wang, Yanqi Liu, Zhen Guo, Lu Xu, Min Xu, Yin Hang, Yi Xu, *et al.*, "339 j high-energy ti: sapphire chirped-pulse amplifier for 10 pw laser facility," Optics letters **43**, 5681–5684 (2018).

[8] C Hernandez-Gomez, SP Blake, O Chekhlov, RJ Clarke, AM Dunne, M Galimberti, S Hancock, R Heathcote, P Holligan, A Lyachev, *et al.*, "The vulcan 10 pw project," Journal of Physics: Conference Series **244**, 032006 (2010).

[9] JP Zou, C Le Blanc, Dimitrios Papadopoulos, G Chériaux, Patrick Georges, G Mennerat, Frédéric Druon, L Lecherbourg, A Pellegrina, and Philippe Ramirez, "Design and current progress of the Apollon 10 PW project," High Power Laser Science and Engineering **3**, e2 (2015).

[10] Xinliang Wang, Xingyan Liu, Xiaoming Lu, Junchi Chen, Yingbin Long, Wenkai Li, Haidong Chen, Xun Chen, Peile Bai, Yanyan Li, Yujie Peng, Yanqi Liu, Fenxiang Wu, Cheng Wang, Zhaoyang Li, Yi Xu, Xiaoyan Liang, Yuxin Leng, and Ruxin Li, "13.4 fs, 0.1 hz opcpa front end for the 100 pw-class laser facility," Ultrafast Science **2022**, 9894358 (2022).

[11] *Whitebook XCELS - Exawatt Center for Extreme Light Studies* (2009).

[12] Colin N Danson, Constantin Haefner, Jake Bromage, Thomas Butcher, Jean-Christophe F Chanteloup, Enam A Chowdhury, Almantas Galvanauskas, Leonida A Gizzi, Joachim Hein, David I Hillier, *et al.*, "Petawatt and exawatt class lasers worldwide," High Power Laser Science and Engineering **7**, e54 (2019).

[13] Jin Woo Yoon, Yeong Gyu Kim, Il Woo Choi, Jae Hee Sung, Hwang Woon Lee, Seong Ku Lee, and Chang Hee Nam, "Realization of laser intensity over $10^{23} w/cm^2$," Optica **8**, 630–635 (2021).

[14] W. P. Leemans, A. J. Gonsalves, H.-S. Mao, K. Nakamura, C. Benedetti, C. B. Schroeder, Cs. Tóth, J. Daniels, D. E. Mittelberger, S. S. Bulanov, J.-L. Vay, C. G. R. Geddes, and E. Esarey, "Multi-gev electron beams from capillary-discharge-guided subpetawatt laser pulses in the self-trapping regime," Phys. Rev. Lett. **113**, 245002 (2014).

[15] Gerard A. Mourou, Toshiki Tajima, and Sergei V. Bulanov, "Optics in the relativistic regime," Rev. Mod. Phys. **78**, 309–371 (2006).

[16] Bruce A. Remington, R. Paul Drake, and Dmitri D. Ryutov, "Experimental astrophysics with high power lasers and z pinches," Rev. Mod. Phys. **78**, 755–807 (2006).

[17] Siegfried H. Glenzer and Ronald Redmer, "X-ray thomson scattering in high energy density plasmas," Rev. Mod. Phys. **81**, 1625–1663 (2009).

[18] John Lindl, "Development of the indirect-drive approach to inertial confinement fusion and the target physics basis for ignition and gain," Physics of Plasmas **2**, 3933–4024 (1995), https://pubs.aip.org/aip/pop/article-pdf/2/11/3933/12577579/3933_1_online.pdf .

[19] O. A. Hurricane, D. A. Callahan, D. T. Casey, P. M. Celliers, C. Cerjan, E. L. Dewald, T. R. Dittrich, T. Döppner, D. E. Hinkel, L. F. Berzak Hopkins, J. L. Kline, S. Le Pape, T. Ma, A. G. MacPhee, J. L. Milovich, A. Pak, H.-S. Park,

P. K. Patel, B. A. Remington, J. D. Salmonson, P. T. Springer, and R. Tommasini, "Fuel gain exceeding unity in an inertially confined fusion implosion," Nature **506**, 343–348 (2014).

[20] T. Tajima and J. M. Dawson, "Laser electron accelerator," Phys. Rev. Lett. **43**, 267–270 (1979).

[21] Eric Esarey, Phillip Sprangle, and Jonathan Krall, "Laser acceleration of electrons in vacuum," Phys. Rev. E **52**, 5443–5453 (1995).

[22] Andrea Macchi, Marco Borghesi, and Matteo Passoni, "Ion acceleration by superintense laser-plasma interaction," Rev. Mod. Phys. **85**, 751–793 (2013).

[23] Avanish Kumar Dubey and Vinod Yadava, "Laser beam machining—a review," International Journal of Machine Tools and Manufacture **48**, 609–628 (2008).

[24] John Ion, *Laser processing of engineering materials: principles, procedure and industrial application* (Elsevier, 2005).

[25] Brian C Wilson and Michael S Patterson, "The physics, biophysics and technology of photodynamic therapy," Physics in Medicine & Biology **53**, R61 (2008).

[26] Sergey A. Ermilov, Tuenchit Khamapirad, André Conjusteau, Morton H. Leonard, Ron Lacewell, Ketan Mehta, Tom Miller, and Alexander A. Oraevsky, "Laser optoacoustic imaging system for detection of breast cancer," Journal of Biomedical Optics **14**, 024007 (2009).

[27] C. Bula, K. T. McDonald, E. J. Prebys, C. Bamber, S. Boege, T. Kotseroglou, A. C. Melissinos, D. D. Meyerhofer, W. Ragg, D. L. Burke, R. C. Field, G. Horton-Smith, A. C. Odian, J. E. Spencer, D. Walz, S. C. Berridge, W. M. Bugg, K. Shmakov, and A. W. Weidemann, "Observation of nonlinear effects in compton scattering," Phys. Rev. Lett. **76**, 3116–3119 (1996).

[28] D. L. Burke, R. C. Field, G. Horton-Smith, J. E. Spencer, D. Walz, S. C. Berridge, W. M. Bugg, K. Shmakov, A. W. Weidemann, C. Bula, K. T. McDonald, E. J. Prebys, C. Bamber, S. J. Boege, T. Koffas, T. Kotseroglou, A. C. Melissinos, D. D. Meyerhofer, D. A. Reis, and W. Ragg, "Positron production in multiphoton light-by-light scattering," Phys. Rev. Lett. **79**, 1626–1629 (1997).

[29] Lyndon Evans and Philip Bryant, "Lhc machine," Journal of Instrumentation **3**, S08001 (2008).

[30] G. Bollen, "FRIB—Facility for Rare Isotope Beams," AIP Conference Proceedings **1224**, 432–441 (2010), https://pubs.aip.org/aip/acp/article-pdf/1224/1/432/11977648/432_1_online.pdf .

[31] Richard H. Parker, Chenghui Yu, Weicheng Zhong, Brian Estey, and Holger Müller, "Measurement of the fine-structure constant as a test of the standard model," Science **360**, 191–195 (2018).

[32] Abhay Deshpande, Richard Milner, Raju Venugopalan, Vogelsang, and Werner, "Study of the fundamental structure of matter with an electron-ion collider," Annual Review of Nuclear and Particle Science **55**, 165–228 (2005).

[33] Bernhard Franzke, Hans Geissel, and Gottfried Münzenberg, "Mass and lifetime measurements of exotic nuclei in storage rings," Mass Spectrometry Reviews **27**, 428–469 (2008).

[34] Paul Adrien Maurice Dirac, "Classical theory of radiating electrons," Proceedings of the Royal Society of London. Series A. Mathematical and Physical Sciences **167**, 148–169 (1938).

[35] L. D. Landau and E. M. Lifshitz, *The Classical Theory of Fields* (Pergamon, Amsterdam, 1975).

[36] T. G. Blackburn, "Radiation reaction in electron–beam interactions with high-intensity lasers," Reviews of Modern Plasma Physics **4**, 5 (2020).

[37] T. G. Blackburn, A. Ilderton, M. Marklund, and C. P. Ridgers, "Reaching supercritical field strengths with intense lasers," New Journal of Physics **21**, 053040 (2019).

[38] V Yakimenko, S Meuren, F Del Gaudio, C Baumann, A Fedotov, F Fiuza, T Grismayer, M J Hogan, A Pukhov, L O Silva, *et al.*, "Prospect of studying nonperturbative qed with beam-beam collisions," Physical Review Letters **122**, 190404 (2019).

[39] C. Baumann, E. N. Nerush, A. Pukhov, and I. Yu Kostyukov, "Probing non-perturbative qed with electron-laser collisions," Scientific Reports **9**, 9407 (2019).

[40] C Baumann and A Pukhov, "Laser-solid interaction and its potential for probing radiative corrections in strong-field quantum electrodynamics," Plasma Physics and Controlled Fusion **61**, 074010 (2019).

[41] V.I. Ritus, "Radiative corrections in quantum electrodynamics with intense field and their analytical properties," Annals of Physics **69**, 555–582 (1972).

[42] N. B. Narozhny, "Expansion parameter of perturbation theory in intense-field quantum electrodynamics," Physical Review D **21**, 1176–1183 (1980).

[43] Alexander Fedotov, "Conjecture of perturbative qed breakdown at $\alpha\chi 2/3 \gtrsim 1$," Journal of Physics: Conference Series **826**, 012027 (2017).

[44] Charles K Birdsall and A Bruce Langdon, *Plasma Physics via Computer Simulation* (CRC press, 1991).

[45] Alexander Pukhov, "Three-dimensional electromagnetic relativistic particle-in-cell code vlpl (virtual laser plasma lab)," Journal of Plasma Physics **61**, 425–433 (1999).

[46] I. Kostyukov, A. Pukhov, and S. Kiselev, "Phenomenological theory of laser-plasma interaction in "bubble" regime," Physics of Plasmas **11**, 5256–5264 (2004).

[47] Antoine Rousse, Kim Ta Phuoc, Rahul Shah, Alexander Pukhov, Eric Lefebvre, Victor Malka, Sergey Kiselev, Fréderic Burgy, Jean-Philippe Rousseau, Donald Umstadter, and Daniéle Hulin, "Production of a kev x-ray beam from synchrotron radiation in relativistic laser-plasma interaction," Physical Review Letters **93**, 135005 (2004).

[48] A. Pukhov and J. Meyer-ter Vehn, "Relativistic laser-plasma interaction by multi-dimensional particle-in-cell simulations," Physics of Plasmas **5**, 1880–1886 (1998).

[49] Vural Kaymak, Alexander Pukhov, Vyacheslav N. Shlyaptsev, and Jorge J. Rocca, "Nanoscale ultradense z-pinch formation from laser-irradiated nanowire arrays," Phys. Rev. Lett. **117**, 035004 (2016).

[50] Jérôme Faure, Yannick Glinec, A Pukhov, S Kiselev, S Gordienko, E Lefebvre, J-P Rousseau, F Burgy, and Victor Malka, "A laser–plasma accelerator producing monoenergetic electron beams," Nature **431**, 541–544 (2004).

[51] Samuel F Martins, RA Fonseca, Wei Lu, Warren B Mori, and LO Silva, "Exploring laser-wakefield-accelerator regimes for near-term lasers using particle-in-cell simulation in lorentz-boosted frames," Nature Physics **6**, 311–316 (2010).

[52] Benoît Cerutti and Andrei M Beloborodov, "Electrodynamics of pulsar magnetospheres," Space Science Reviews **207**, 111–136 (2017).

[53] Alexander A Philippov and Anatoly Spitkovsky, "Ab initio pulsar magnetosphere: three-dimensional particle-in-cell simulations of axisymmetric pulsars," The Astrophysical Journal Letters **785**, L33 (2014).

[54] Kane Yee, "Numerical solution of initial boundary value problems involving maxwell's equations in isotropic media," IEEE Transactions on antennas and propagation **14**, 302–307 (1966).

[55] VI Ritus, "Quantum effects of the interaction of elementary particles with an intense electromagnetic field," Journal of Soviet Laser Research **6**, 497–617 (1985).

[56] G. Breit and John A. Wheeler, "Collision of two light quanta," Phys. Rev. **46**, 1087–1091 (1934).

[57] Alexander Pukhov, "Particle-in-cell codes for plasma-based particle acceleration," CERN Yellow Reports **1**, 181 (2016).

[58] Karl-Heinz Spatschek, *High temperature plasmas: theory and mathematical tools for laser and fusion plasmas* (John Wiley & Sons, 2013).

[59] Alexander Pukhov, "Lecture notes in introduction to plasma theory," (2017).

[60] Robert J Goldston, *Introduction to plasma physics* (CRC Press, 2020).

[61] Paul M Bellan, *Fundamentals of plasma physics* (Cambridge university press, 2008).

[62] Paul Gibbon, *Short Pulse Laser Interactions with Matter* (PUBLISHED BY IMPERIAL COLLEGE PRESS AND DISTRIBUTED BY WORLD SCIENTIFIC PUBLISHING CO., 2005) https://www.worldscientific.com/doi/pdf/10.1142/p116 .

[63] Brice Quesnel and Patrick Mora, "Theory and simulation of the interaction of ultraintense laser pulses with electrons in vacuum," Phys. Rev. E **58**, 3719–3732 (1998).

[64] William Kruer, *The physics of laser plasma interactions* (crc Press, 2019).

[65] D. Bruß, "Lecture notes of "Theoretische Elektrodynamik"," (2015).

[66] A. Di Piazza, C. Müller, K. Z. Hatsagortsyan, and Ch H. Keitel, "Extremely high-intensity laser interactions with fundamental quantum systems," Reviews of Modern Physics **84**, 1177 (2012).

[67] Orazio Svelto, David C Hanna, *et al.*, *Principles of lasers*, Vol. 1 (Springer, 2010).

[68] Julian Schwinger, "On the classical radiation of accelerated electrons," Phys. Rev. **75**, 1912–1925 (1949).

[69] Julian Schwinger, "On gauge invariance and vacuum polarization," Physical Review **82**, 664 (1951).

[70] Howard R. Reiss, "Absorption of Light by Light," Journal of Mathematical Physics **3**, 59–67 (2004), https://pubs.aip.org/aip/jmp/article-pdf/3/1/59/8158035/59_1_online.pdf .

[71] A. Gonoskov, S. Bastrakov, E. Efimenko, A. Ilderton, M. Marklund, I. Meyerov, A. Muraviev, A. Sergeev, I. Surmin, and Erik Wallin, "Extended particle-in-cell schemes for physics in ultrastrong laser fields: Review and developments," Physical review E **92**, 023305 (2015).

[72] N. V. Elkina, A. M. Fedotov, I. Yu. Kostyukov, M. V. Legkov, N. B. Narozhny, E. N. Nerush, and H. Ruhl, "QED cascades induced by circularly polarized laser fields," Physical Review Special Topics: Accelerator and Beams **14**, 054401 (2011).

[73] AI Nikishov and VI Ritus, "Quantum processes in the field of a plane electromagnetic wave and in a constant field. i," Sov. Phys. JETP **19**, 529–541 (1964).

[74] V. B. Berestetskii, E. M. Lifshitz, and L. P. Pitaevskii, *Quantum electrodynamics*, Vol. 4 (Butterworth-Heinemann, 1982).

[75] AI Nikishov and VI Ritus, "Pair production by a photon and photon emission by an electron in the field of an intense electromagnetic wave and in a constant field," Sov. Phys. JETP **25**, 1135–1142 (1967).

[76] A. I. Voroshilo, E. A. Padusenko, and S. P. Roshchupkin, "One-photon annihilation of an electron-positron pair in the field of pulsed circularly polarized light wave," Laser Physics **20**, 1679–1685 (2010).

[77] Alexander Pukhov, "X-dispersionless maxwell solver for plasma-based particle acceleration," Journal of Computational Physics **418**, 109622 (2020).

[78] Benjamin M. Cowan, David L. Bruhwiler, John R. Cary, Estelle Cormier-Michel, and Cameron G. R. Geddes, "Generalized algorithm for control of numerical dispersion in explicit time-domain electromagnetic simulations," Phys. Rev. ST Accel. Beams **16**, 041303 (2013).

[79] R. Lehe, A. Lifschitz, C. Thaury, V. Malka, and X. Davoine, "Numerical growth of emittance in simulations of laser-wakefield acceleration," Phys. Rev. ST Accel. Beams **16**, 021301 (2013).

[80] Alexander Blinne, David Schinkel, Stephan Kuschel, Nina Elkina, Sergey G. Rykovanov, and Matt Zepf, "A systematic approach to numerical dispersion in maxwell solvers," Computer Physics Communications **224**, 273–281 (2018).

[81] Jean-Luc Vay, Irving Haber, and Brendan B. Godfrey, "A domain decomposition method for pseudo-spectral electromagnetic simulations of plasmas," Journal of Computational Physics **243**, 260–268 (2013).

[82] R. Courant, K. Friedrichs, and H. Lewy, "Über die partiellen differenzengleichungen der mathematischen physik," Mathematische Annalen **100**, 32–74 (1928).

[83] Jay P Boris and Roswell Lee, "Nonphysical self forces in some electromagnetic plasma-simulation algorithms," Journal of Computational Physics **12**, 131–136 (1973).

[84] Fei Li, Viktor K. Decyk, Kyle G. Miller, Adam Tableman, Frank S. Tsung, Marija Vranic, Ricardo A. Fonseca, and Warren B. Mori, "Accurately simulating nine-dimensional phase space of relativistic particles in strong fields," Journal of Computational Physics **438**, 110367 (2021).

[85] D.F. Gordon and B. Hafizi, "Special unitary particle pusher for extreme fields," Computer Physics Communications **258**, 107628 (2021).

[86] T D Arber, K Bennett, C S Brady, A Lawrence-Douglas, M G Ramsay, N J Sircombe, P Gillies, R G Evans, H Schmitz, A R Bell, and C P Ridgers, "Contemporary particle-in-cell approach to laser-plasma modelling," Plasma Physics and Controlled Fusion **57**, 113001 (2015).

[87] J. Derouillat, A. Beck, F. Pérez, T. Vinci, M. Chiaramello, A. Grassi, M. Flé, G. Bouchard, I. Plotnikov, N. Aunai, J. Dargent, C. Riconda, and M. Grech, "Smilei : A collaborative, open-source, multi-purpose particle-in-cell code for plasma simulation," Computer Physics Communications **222**, 351–373 (2018).

[88] R. A. Fonseca, L. O. Silva, F. S. Tsung, V. K. Decyk, W. Lu, C. Ren, W. B. Mori, S. Deng, S. Lee, T. Katsouleas, and J. C. Adam, "Osiris: A three-dimensional, fully relativistic particle in cell code for modeling plasma based accelerators," in *Computational Science — ICCS 2002*, edited by Peter M. A. Sloot, Alfons G.

Hoekstra, C. J. Kenneth Tan, and Jack J. Dongarra (Springer Berlin Heidelberg, Berlin, Heidelberg, 2002) pp. 342–351.

[89] J.-L. Vay, A. Almgren, J. Bell, L. Ge, D.P. Grote, M. Hogan, O. Kononenko, R. Lehe, A. Myers, C. Ng, J. Park, R. Ryne, O. Shapoval, M. Thévenet, and W. Zhang, "Warp-x: A new exascale computing platform for beam–plasma simulations," Nuclear Instruments and Methods in Physics Research Section A: Accelerators, Spectrometers, Detectors and Associated Equipment **909**, 476–479 (2018), 3rd European Advanced Accelerator Concepts workshop (EAAC2017).

[90] V N Baier, V M Katkov, and V M Strakhovenko, *Electromagnetic Processes at High Energies in Oriented Single Crystals* (World Scientific, 1998).

[91] T. G. Blackburn, C. P. Ridgers, J. G. Kirk, and A. R. Bell, "Quantum radiation reaction in laser–electron-beam collisions," Physical Review Letters **112**, 015001 (2014).

[92] Matteo Tamburini, Antonino Di Piazza, and Christoph H Keitel, "Laser-pulse-shape control of seeded qed cascades," Scientific reports **7**, 1–8 (2017).

[93] T. Grismayer, M. Vranic, J. L. Martins, R. A. Fonseca, and L. O. Silva, "Seeded qed cascades in counterpropagating laser pulses," Phys. Rev. E **95**, 023210 (2017).

[94] SS Bulanov, CB Schroeder, E Esarey, and WP Leemans, "Electromagnetic cascade in high-energy electron, positron, and photon interactions with intense laser pulses," Physical Review A **87**, 062110 (2013).

[95] M. Afshari, S. Morris, L. D. Geulig, Z. M. Chitgar, P. Gibbon, P. G. Thirolf, and J. Schreiber, "The role of collisional ionization in heavy ion acceleration by high intensity laser pulses," Scientific Reports **12**, 18260 (2022).

[96] R. Hollinger, S. Wang, Y. Wang, A. Moreau, M. G. Capeluto, H. Song, A. Rockwood, E. Bayarsaikhan, V. Kaymak, A. Pukhov, V. N. Shlyaptsev, and J. J. Rocca, "Extreme ionization of heavy atoms in solid-density plasmas by relativistic second-harmonic laser pulses," Nature Photonics **14**, 607–611 (2020).

[97] Robert Scott Martin and Jean-Luc Cambier, "Octree particle management for dsmc and pic simulations," Journal of Computational Physics **327**, 943–966 (2016).

[98] Giovanni Lapenta and Jeremiah U. Brackbill, "Dynamic and selective control of the number of particles in kinetic plasma simulations," Journal of Computational Physics **115**, 213–227 (1994).

[99] Marija Vranic, Thomas Grismayer, Joana Luis Martins, Ricardo A Fonseca, and Luis O Silva, "Particle merging algorithm for pic codes," Computer Physics Communications **191**, 65–73 (2015).

[100] Phuc T Luu and T Tückmantel, "Voronoi particle merging algorithm for pic codes," Computer Physics Communications **202**, 165–174 (2016).

[101] Qian Dong, Binglin Wang, Xiaojun Duan, Liang Yan, Ke Liu, Wen Luo, Fuqiu Shao, and Tongpu Yu, "A dynamical particle merging and splitting algorithm for particle-in-cell simulations," Computer Physics Communications **294**, 108913 (2024).

[102] D.R. Welch, T.C. Genoni, R.E. Clark, and D.V. Rose, "Adaptive particle management in a particle-in-cell code," Journal of Computational Physics **227**, 143–155 (2007).

[103] F. Assous, T. Pougeard Dulimbert, and J. Segré, "A new method for coalescing particles in pic codes," Journal of Computational Physics **187**, 550–571 (2003).

[104] Georgy Voronoi, "Nouvelles applications des paramèrtes continus à la théorie des formes quadratiques. deuxième memorie: Recherche sur les parallélloèdres primitifs," Journal fur reine und angewandte Mathematik **3**, 198–287 (1907).

[105] M. Filipovic, C. Baumann, and A. Pukhov, "Suppression of errors in simulated ultrarelativistic bunch propagation using the x-dispersionless maxwell solver," Phys. Rev. Accel. Beams **25**, 054405 (2022).

[106] Brendan B Godfrey, "Canonical momenta and numerical instabilities in particle codes," Journal of Computational Physics **19**, 58–76 (1975).

[107] Brendan B Godfrey, "Numerical cherenkov instabilities in electromagnetic particle codes," Journal of Computational Physics **15**, 504–521 (1974).

[108] D-Y Na, Julio L Nicolini, Robert Lee, B-HV Borges, Yuri A Omelchenko, and Fernando L Teixeira, "Diagnosing numerical cherenkov instabilities in relativistic plasma simulations based on general meshes," Journal of Computational Physics **402**, 108880 (2020).

[109] Brendan B. Godfrey, "Review and recent advances in PIC modeling of relativistic beams and plasmas," AIP Conference Proceedings **1777**, 020004 (2016).

[110] Xinlu Xu, Peicheng Yu, Samual F Martins, Frank S Tsung, Viktor K Decyk, Jorge Vieira, Ricardo A Fonseca, Wei Lu, Luis O Silva, and Warren B Mori, "Numerical instability due to relativistic plasma drift in em-pic simulations," Computer Physics Communications **184**, 2503–2514 (2013).

[111] Xinlu Xu, Fei Li, Frank S. Tsung, Thamine N. Dalichaouch, Weiming An, Han Wen, Viktor K. Decyk, Ricardo A. Fonseca, Mark J. Hogan, and Warren B. Mori, "On numerical errors to the fields surrounding a relativistically moving particle in pic codes," Journal of Computational Physics **413**, 109451 (2020).

[112] S. Jalas, I. Dornmair, R. Lehe, H. Vincenti, J.-L. Vay, M. Kirchen, and A. R. Maier, "Accurate modeling of plasma acceleration with arbitrary order pseudo-spectral particle-in-cell methods," Physics of Plasmas **24**, 033115 (2017), https://doi.org/10.1063/1.4978569 .

[113] Rachel Nuter and Vladimir Tikhonchuk, "Suppressing the numerical cherenkov radiation in the yee numerical scheme," Journal of Computational Physics **305**, 664–676 (2016).

[114] Remi Lehe, Manuel Kirchen, Brendan B Godfrey, Andreas R Maier, and Jean-Luc Vay, "Elimination of numerical cherenkov instability in flowing-plasma particle-in-cell simulations by using galilean coordinates," Physical Review E **94**, 053305 (2016).

[115] Fei Li, Peicheng Yu, Xinlu Xu, Frederico Fiuza, Viktor K Decyk, Thamine Dalichaouch, Asher Davidson, Adam Tableman, Weiming An, Frank S Tsung, *et al.*, "Controlling the numerical cerenkov instability in pic simulations using a customized finite difference maxwell solver and a local fft based current correction," Computer Physics Communications **214**, 6–17 (2017).

[116] Brendan B. Godfrey and Jean-Luc Vay, "Suppressing the numerical cherenkov instability in FDTD PIC codes," Journal of Computational Physics **267**, 1–6 (2014).

[117] J.-L. Vay, C.G.R. Geddes, E. Cormier-Michel, and D.P. Grote, "Numerical methods for instability mitigation in the modeling of laser wakefield accelerators in a lorentz-boosted frame," Journal of Computational Physics **230**, 5908–5929 (2011).

[118] Peicheng Yu, Xinlu Xu, Viktor K. Decyk, Frederico Fiuza, Jorge Vieira, Frank S. Tsung, Ricardo A. Fonseca, Wei Lu, Luis O. Silva, and Warren B. Mori, "Elimination of the numerical cerenkov instability for spectral EM-PIC codes," Computer Physics Communications **192**, 32–47 (2015).

[119] Peicheng Yu, Xinlu Xu, Adam Tableman, Viktor K. Decyk, Frank S. Tsung, Frederico Fiuza, Asher Davidson, Jorge Vieira, Ricardo A. Fonseca, Wei Lu, Luis O. Silva, and Warren B. Mori, "Mitigation of numerical cerenkov radiation and instability using a hybrid finite difference-FFT maxwell solver and a local charge conserving current deposit," Computer Physics Communications **197**, 144–152 (2015).

[120] F Del Gaudio, T Grismayer, R A Fonseca, W B Mori, and L O Silva, "Bright γ rays source and nonlinear breit-wheeler pairs in the collision of high density particle beams," Physical Review Accelerators and Beams **22**, 023402 (2019).

[121] R. Lehe, C. Thaury, E. Guillaume, A. Lifschitz, and V. Malka, "Laser-plasma lens for laser-wakefield accelerators," Physical Review Special Topics: Accelerator and Beams **17**, 121301 (2014).

[122] Allen Taflove, Susan C Hagness, and Melinda Piket-May, "Computational electromagnetics: the finite-difference time-domain method," The Electrical Engineering Handbook **3** (2005).

[123] Kaoru Yokoya and Pisin Chen, "Beam-beam phenomena in linear colliders," in *Frontiers of Particle Beams: Intensity Limitations* (Springer, 1992) pp. 415–445.

[124] Pisin Chen and Valery I Telnov, "Coherent pair creation in linear colliders," Physical review letters **63**, 1796 (1989).

[125] M Filipovic, Christoph Baumann, Alexander M Pukhov, Aleksandr Sergeevich Samsonov, and I Yu Kostyukov, "Effect of transverse displacement of charged particle beams on quantum electrodynamic processes during their collision," Quantum Electronics **51**, 807 (2021).

[126] Matteo Tamburini and Sebastian Meuren, "Efficient high-energy photon production in the supercritical qed regime," Phys. Rev. D **104**, L091903 (2021).

[127] K. Poder, M. Tamburini, G. Sarri, A. Di Piazza, S. Kuschel, C. D. Baird, K. Behm, S. Bohlen, J. M. Cole, D. J. Corvan, M. Duff, E. Gerstmayr, C. H. Keitel, K. Krushelnick, S. P. D. Mangles, P. McKenna, C. D. Murphy, Z. Najmudin, C. P. Ridgers, G. M. Samarin, D. R. Symes, A. G. R. Thomas, J. Warwick, and M. Zepf, "Experimental signatures of the quantum nature of radiation reaction in the field of an ultraintense laser," Phys. Rev. X **8**, 031004 (2018).

[128] J. M. Cole, K. T. Behm, E. Gerstmayr, T. G. Blackburn, J. C. Wood, C. D. Baird, M. J. Duff, C. Harvey, A. Ilderton, A. S. Joglekar, K. Krushelnick, S. Kuschel,

M. Marklund, P. McKenna, C. D. Murphy, K. Poder, C. P. Ridgers, G. M. Samarin, G. Sarri, D. R. Symes, A. G. R. Thomas, J. Warwick, M. Zepf, Z. Najmudin, and S. P. D. Mangles, "Experimental evidence of radiation reaction in the collision of a high-intensity laser pulse with a laser-wakefield accelerated electron beam," Phys. Rev. X **8**, 011020 (2018).

[129] T. N. Wistisen, A. Di Piazza, C. F. Nielsen, A. H. Sørensen, and U. I. Uggerhøj (CERN NA63), "Quantum radiation reaction in aligned crystals beyond the local constant field approximation," Phys. Rev. Res. **1**, 033014 (2019).

[130] AA Mironov, S Meuren, and AM Fedotov, "Resummation of qed radiative corrections in a strong constant crossed field," Physical Review D **102**, 053005 (2020).

[131] Robin Ekman, Tom Heinzl, and Anton Ilderton, "High-intensity scaling in uv-modified qed," Physical Review D **102**, 116005 (2020).

[132] Aimé Matheron, Pablo San Miguel Claveria, Robert Ariniello, Henrik Ekerfelt, Frederico Fiuza, Spencer Gessner, Max F. Gilljohann, Mark J. Hogan, Christoph H. Keitel, Alexander Knetsch, Mike Litos, Yuliia Mankovska, Samuele Montefiori, Zan Nie, Brendan O'Shea, J. Ryan Peterson, Doug Storey, Yipeng Wu, Xinlu Xu, Viktoriia Zakharova, Xavier Davoine, Laurent Gremillet, Matteo Tamburini, and Sébastien Corde, "Probing strong-field qed in beam-plasma collisions," Communications Physics **6**, 141 (2023).

[133] C Baumann and A Pukhov, "Influence of e- e+ creation on the radiative trapping in ultraintense fields of colliding laser pulses," Physical Review E **94**, 063204 (2016).

[134] A S Samsonov, E N Nerush, I Yu Kostyukov, M Filipovic, C Baumann, and A Pukhov, "Beamstrahlung-enhanced disruption in beam–beam interaction," New Journal of Physics **23**, 103040 (2021).

[135] Filipovic, Marko and Pukhov, Alexander, "QED effects at grazing incidence on solid-state targets," Eur. Phys. J. D **76**, 187 (2022).

[136] Jie Zhao, Yan-Ting Hu, Yu Lu, Hao Zhang, Li-Xiang Hu, Xing-Long Zhu, Zheng-Ming Sheng, Ion Cristian Edmond Turcu, Alexander Pukhov, Fu-Qiu Shao, and Tong-Pu Yu, "All-optical quasi-monoenergetic gev positron bunch generation by twisted laser fields," Communications Physics **5**, 15 (2022).

[137] Xing-Long Zhu, Tong-Pu Yu, Zheng-Ming Sheng, Yan Yin, Ion Cristian Edmond Turcu, and Alexander Pukhov, "Dense gev electron–positron pairs generated by lasers in near-critical-density plasmas," Nature Communications **7**, 13686 (2016).

[138] Xing-Long Zhu, Tong-Pu Yu, Min Chen, Su-Ming Weng, and Zheng-Ming Sheng, "Generation of gev positron and γ-photon beams with controllable angular momentum by intense lasers," New Journal of Physics **20**, 083013 (2018).

[139] I. C. E. Turcu, B. Shen, D. Neely, G. Sarri, K. A. Tanaka, P. McKenna, S. P. D. Mangles, T.-P. Yu, W. Luo, X.-L. Zhu, and et al., "Quantum electrodynamics experiments with colliding petawatt laser pulses," High Power Laser Science and Engineering **7**, e10 (2019).

[140] Peng Zhang, C P Ridgers, and A G R Thomas, "The effect of nonlinear quantum electrodynamics on relativistic transparency and laser absorption in ultra-relativistic plasmas," New Journal of Physics **17**, 043051 (2015).

[141] D. A. Serebryakov, E. N. Nerush, and I. Yu. Kostyukov, "Near-surface electron acceleration during intense laser-solid interaction in the grazing incidence regime," Physics of Plasmas **24**, 123115 (2017), https://doi.org/10.1063/1.5002671 .

[142] A. M. Fedotov, N. B. Narozhny, G. Mourou, and G. Korn, "Limitations on the attainable intensity of high power lasers," Phys. Rev. Lett. **105**, 080402 (2010).

[143] A. R. Bell and J. G. Kirk, "Possibility of prolific pair production with high-power lasers," Physical Review Letters **101**, 200403 (2008).

[144] John G Kirk, AR Bell, and Ioanna Arka, "Pair production in counter-propagating laser beams," Plasma Physics and Controlled Fusion **51**, 085008 (2009).

[145] T. Grismayer, M. Vranic, J. L. Martins, R. A. Fonseca, and L. O. Silva, "Laser absorption via quantum electrodynamics cascades in counter propagating laser pulses," Physics of Plasmas **23**, 056706 (2016), https://doi.org/10.1063/1.4950841 .

[146] Marija Vranic, Thomas Grismayer, Ricardo A Fonseca, and Luis O Silva, "Electron–positron cascades in multiple-laser optical traps," Plasma Physics and Controlled Fusion **59**, 014040 (2016).

[147] C. P. Ridgers, C. S. Brady, R. Duclous, J. G. Kirk, K. Bennett, T. D. Arber, A. P. L. Robinson, and A. R. Bell, "Dense electron-positron plasmas and ultraintense γ rays from laser-irradiated solids," Physical Review Letters **108**, 165006 (2012).

[148] Archana Sampath and Matteo Tamburini, "Towards realistic simulations of qed cascades: Non-ideal laser and electron seeding effects," Physics of Plasmas **25**, 083104 (2018), https://doi.org/10.1063/1.5022640 .